

Friction in silicon dioxide micro-contacts

Présentée le 16 décembre 2020

à la Faculté des sciences et techniques de l'ingénieur
Groupe SCI STI SM
Programme doctoral en science et génie des matériaux

pour l'obtention du grade de Docteur ès Sciences

par

Vance NGUYEN

Acceptée sur proposition du jury

Prof. D. Damjanovic, président du jury
Dr S. Mischler, directeur de thèse
Dr J. Perret, rapporteur
Prof. M. Scherge, rapporteur
Prof. H. Brune, rapporteur

Acknowledgements

This thesis could never have been completed without the support of many people, both collaborators and friends. Of course, first and foremost, there has been the utmost support from my thesis supervisor Dr. Stefano Mischler and the members of the TIC group throughout my time at EPFL. Every one of the group members and students that I've come to work with has given me invaluable advice at our meetings. I would like to personally thank the fellow PhD students working with me including: Shoufan, Maxime, Angela, Leili, Fabio, Valentine, and Yueyue. Thanks also to Dr. Anna Igual-Munoz for the critical scientific discussions at group meetings, and a special thanks to Dr. Alejandro Roda-Buch for our numerous discussions and for his indispensable help in developing the MATLAB code for contact simulations.

Thanks to Pierre Mettraux for constant technical support and for performing the XPS measurements. Thanks to Sylvie Vaucher for all of the invaluable administrative support. Thanks to Dr. Lucie Navratilova of CIME for performing the FIB cross-sections and for advice on SEM measurements. Thanks to Raphaël Foschia and Caroline Lehmann of the Laboratory of the Physics of Living Matter (LPMV) for providing the AFM for measurements. Thanks to my friend Jules Macé for helping with French proofreading. Thanks to members of the Soft Materials Laboratory (SMaL) for lending me the rheometer and contact angle microscope, and for providing me with TCDS. Thanks also to Dr. Reuben Yeo of the Laboratory of Macromolecular and Organic Materials (LMOM) for providing training and support for tribological experiments.

I would finally like to thank Dr. Julien Perret and Dr. Frédéric Maier for their support and frequent scientific discussions. Thanks to both for making the regular trips to Lausanne and suffering through the lengthy presentations. It has truly been an privilege for me to be able to work with them.

Lausanne, December 4 2020

Vance Nguyen

Abstract

Silicon dioxide is finding more and more applications in tribological systems thanks in part to the possibilities of micro-fabrication in large scales at high precision, and in part to its good mechanical properties. It has found a particular niche in the horological industry, being used in various wristwatch components. In industry applications, the primary challenge is to develop a tribosystem that allows constant and minimal friction for the micro-scale geometry and load conditions. A scientific approach is used to address the industry challenges. An overview of the state of the art reveals a gap in literature regarding tribological studies under watch-relevant micro-scale conditions. Thus, the devices and methods are developed that allow experimental studies under micro-scale conditions with precise geometric constraints. A detailed physical characterization of the tribocontact allows quantification of contact conditions using boundary element simulation. Tribological experiments demonstrate dependence of friction on contact area and on surface adsorption of contaminants. It also reveals a characteristic behavior of friction increase that consists of a time-dependent recoverable component, and a irrecoverable cumulative component. A simple mechanistic model is developed based on adsorption of contaminants and evolution of elastic deformation energy due to crack growth. The model is then assessed for its applicability to the experimental system. Ultimately, this study allows quantification of the trade-off between contact area and contact pressure in systems of thermally grown silicon dioxide given any surface topography, while also considering effects of contaminant adsorption.

Résumé

L'oxyde de silicium trouve de plus en plus d'applications dans les systèmes tribologiques grâce aux possibilités de microfabrication à haute précision et grâce à ses bonnes propriétés mécaniques. Il a trouvé une application particulière dans l'industrie horlogère, étant utilisé dans les montre à mouvement mécanique. Dans les applications industrielles, le principal défi consiste à développer un tribosystème qui permette une friction constante et minimale pour les conditions à micro-échelle de géométrie et de charge. Une approche scientifique est utilisée pour relever les défis de l'industrie. Un aperçu de l'état de l'art révèle une lacune de la littérature concernant les études tribologiques dans des conditions à micro-échelle pertinentes pour les montres. Ainsi, des dispositifs et des méthodes sont développés qui permettent des études expérimentales dans des conditions à micro-échelle avec des contraintes géométriques précises. Une caractérisation physique détaillée du tribocontact permet de quantifier les conditions de contact à l'aide de la méthodes à éléments de frontière. Les expériences tribologiques démontrent la dépendance du frottement sur la surface de contact et l'adsorption des contaminants. Elles révèlent également un comportement caractéristique d'augmentation de la friction qui consiste en un composant récupérable dépendant du temps, et un composant cumulatif irrécupérable. Un modèle mécaniste simple est développé, basé sur l'adsorption des contaminants et l'évolution de l'énergie de déformation élastique due à la croissance de fissures. Le modèle est ensuite évalué pour son applicabilité au système expérimental. En conclusion, cette étude permet de quantifier le compromis entre la surface de contact et la pression de contact dans les systèmes de dioxyde de silicium, pour une topographie de surface donné, tout en tenant compte des effets de l'adsorption des contaminants.

Contents

Acknowledgements	iii
Abstract (English/Français)	v
List of Figures	x
List of Tables	xiv
List of Symbols	xvii
List of Acronyms	xix
1 Introduction	1
1.1 Industry Motivation	1
1.2 Scientific Challenge	1
1.3 Thesis Structure	2
2 State of the Art	5
2.1 Friction and Wear	5
2.2 Friction of Silicon Dioxide	8
2.3 Wear of Silicon Dioxide	11
2.4 Modeling of Friction	12
2.5 Outlook	16
3 Methods	19
3.1 Tribological Experiments	19
3.1.1 Tribometer Specifications	19
3.1.2 Sensor Calibration	20
3.1.3 Sample Design	21
3.1.4 Sample Mounting	24
3.1.5 Experimental Conditions	27
3.1.6 Data Post-Processing	29
3.2 Atomic Force Microscopy	33
3.3 Scanning Electron Microscopy	33
3.4 Focused Ion Beam	33
3.5 X-Ray Photoelectron Spectroscopy	34
3.6 Summary	34
	ix

4	Topography and Contact Mechanics	35
4.1	Topography	35
4.2	Contact Simulation	38
4.3	Experimental Validation	42
4.4	Summary	45
5	Experimental Results	47
5.1	Effects of Contact Radius	47
5.2	Effects of Load	54
5.3	Interrupted Experiments	60
5.4	Surface Pretreatment	61
5.5	Effect of Topography	66
5.6	Discussion	70
6	Modeling Friction	73
6.1	Introduction	73
6.2	Energy of Adhesion E_{ad}	75
6.3	Vertical Elastic Deformation E_{Ez}	77
6.4	Tangential Elastic Deformation E_{Ey}	79
6.4.1	Shear Strain Model	79
6.4.2	Cantilever Beam Model	80
6.4.3	Crack Growth Rate	81
6.5	Summary	82
7	Application of Model	85
7.1	Friction Regimes	85
7.2	Determination of Parameters	86
7.2.1	Determination of k_a & k_r	90
7.2.2	Determination of Crack Growth	94
7.3	Time Extrapolation	100
7.4	Cylinder Misalignment	101
7.5	Varying Load	102
7.6	Varying Counterpiece Radius	106
7.7	Chemical Treatments	107
7.8	Topography Effects	108
7.9	Summary	111
8	Conclusions	113
	References	117
	Curriculum Vitae	119

List of Figures

2.1	Apparent contact and asperity junctions that make up the real contact area . . .	5
2.2	Stress-strain behavior of a brittle material and a ductile material	7
2.3	Static friction, μ_S , and kinetic friction, μ_K , in self-mated silicon dioxide contacts	9
2.4	Friction of 3 mm radius ball on flat silicon nitride in air	10
2.5	The structure of an adsorbed water layer on silicon dioxide and physisorbed 1-propanol	11
2.6	Mechanism of flake formation as cracks propagate below the surface in the direction of sliding	12
2.7	Illustration of the Prandtl-Tomlinson model	15
2.8	Generic hysteresis loop of tangential force as given by the Dahl model	16
3.1	Photo of tribometer experimental area	20
3.2	Calibration curve of cantilever used to derive spring constant	21
3.3	Illustration of the geometry of the contact of a misaligned cylinder on flat surface	21
3.4	SEM image of a cross-section of a fractured sample	22
3.5	SEM images of a sample from the side perpendicular to sliding	22
3.6	SEM images of cylinder body of samples R5A, R5B, R5C and R5D prior to tribo- logical experiment	23
3.7	Designed sample etched from thermally oxidized silicon wafer	24
3.8	Displacement gauges are used to align the edges and surfaces	25
3.9	The four steps of mounting the sample viewed from Camera A perspective . . .	25
3.10	Camera B view from the side and Camera A view from the front of a sample (black) glued to the sample holder	26
3.11	Camera A view for alignment of sample before experiment	26
3.12	Normal force of one cycle in fixed-displacement experiment	27
3.13	Temperature evolution over 60 hours and its effects on normal load	28
3.14	Tangential force output adjusted for cantilever deflection	29
3.15	Calculated velocity (30 Hz low-pass filtered) and acceleration from the differen- tial of Y position	30
3.16	Mechanical resonance of the cantilever in air of approximately 28 Hz	30
3.17	Filtered signals of tangential load eliminating mechanical resonance effects . .	31
3.18	Tangential force signals are averaged within the intersection of the maximum velocity zone	31
3.19	Adjustment of tangential load for tilt angle	32
4.1	AFM images of Samples A, B, C and D	36
4.2	Contact AFM measurements on R5A samples	37

4.3	Cross-sectional profiles of Sample R5A, R5B, and R5C in direction perpendicular to sliding.	37
4.4	Cross-sectional profile of AFM images of R5D in direction perpendicular to sliding	38
4.5	Contact area of ideal cylinder on flat and contact area of misaligned cylinder on flat	38
4.6	Contact idealized as smooth cylinder upper body on rough flat surface	39
4.7	Distance mesh of the contact of cylinder-torus geometry with imposed angle of 0.1° and radii corresponding to R10 sample	39
4.8	An AFM profile of R5B perpendicular to sliding direction, repetitively stitched for application with numerical simulation	40
4.9	Distance mesh of topography A with AFM profile superimposed and assuming perfectly smooth upper counterpiece	40
4.10	The contact of cylinder-torus geometry representing R10A samples at 0.4° tilt .	41
4.11	Scratch test results of 0.2 mN load for R10 samples on 3 nm gold layer after 10 oscillations with 0.4° angl	42
4.12	Scratch test results of 0.5 mN load for R10 samples on 3 nm gold layer after 10 oscillations with 0.4° angle	43
4.13	Scratch test results of 1 mN load for R10 samples on 3 nm gold layer after 10 oscillations with 0.4° angle	43
4.14	Scratch test results of 2 mN load for R10 samples on 3 nm gold layer after 10 oscillations with 0.4° angle	44
4.15	Comparing simulated contact widths from the BES with experimental contact widths from gold scratches using R10A samples at 0.4° tilt	45
5.1	Coefficient of friction evolution over 5000 cycles at 1 Hz, 8 mm/s, 1 mN, 2 mm sliding length for R5A and R20A samples	48
5.2	Surface of R5A flat surface before tribological experiment	49
5.3	Surface of R5A flat surface after 10000 cycles at 1 Hz, 8 mm/s, 1 mN, 2 mm sliding length	49
5.4	Surface of R5A cylinder after tribological experiment	50
5.5	FIB cross-section of R5A sample after 10000 cycles at 1 Hz, 8 mm/s, 1 mN, 2 mm sliding length	51
5.6	High magnification extract of previous cross-section of R5A sample transverse the wear track	52
5.7	AFM profiles in the direction perpendicular to the sliding direction	52
5.8	Varying length-scale roughness of the AFM profiles	53
5.9	Coefficient of friction evolution of R5A samples over 1000 cycles at 1 Hz, 8 mm/s, 2 mm sliding length at varying loads	54
5.10	Friction shown as a function of contact width	55
5.11	SEM image of the low friction wear trace after 5000 cycles at 1 Hz, 8 mm/s, 2 mm sliding length and 4 mN load4mNflat1	56

5.12 SEM image of the cylinder counterpiece in the low friction experiment after 5000 cycles at 1 Hz, 8 mm/s, 2 mm sliding length and 4 mN load	56
5.13 SEM image of the high friction wear trace after 300 cycles at 1 Hz, 8 mm/s, 2 mm sliding length and 4 mN load	57
5.14 SEM image of the cylinder counterpiece in the high friction experiment after 300 cycles at 1 Hz, 8 mm/s, 2 mm sliding length and 4 mN load	57
5.15 SEM images of cylinder body of samples R5A after tribological experiments at varying loads	58
5.16 SEM images of flat surface of samples R5A after tribological experiments at varying loads	59
5.17 Coefficient of friction evolution of R5A samples over 50000 cycles at 1 Hz, 8 mm/s, 1 mN, 2 mm sliding length	60
5.18 Coefficient of friction evolution of R5A samples over 50000 cycles at 1 Hz, 8 mm/s, 1 mN, 2 mm sliding length with varying interruption time	61
5.19 Photoemission spectrum from XPS analyses	62
5.20 C1s emission intensity from XPS analyses	63
5.21 O1s emission intensity from XPS analyses	64
5.22 Si2p emission intensity from XPS analyses	64
5.23 Coefficient of friction evolution of 70000 cycles at 1 Hz, 8 mm/s, 1 mN, 2 mm sliding length, with 15 s interruptions every 5000 cycles, after various cleaning pretreatments	65
5.24 Coefficient of friction evolution of R5A samples over 5000 cycles at 1 Hz, 8 mm/s, 1 mN, 2 mm sliding length, with R5A, R5B and R5C	66
5.25 SEM image of flat surface of R5B before experiment	67
5.26 SEM image of flat surface of R5B after 5000 cycles under 1 mN	67
5.27 SEM images of cylinder body of samples R5A, R5B and R5C after tribological experiments at varying 1 mN load	68
5.28 Coefficient of friction evolution of R5A samples over 5000 cycles at 1 Hz, 8 mm/s, 0.1 mN, 2 mm sliding length, with four different surface topographies	69
5.29 SEM images of cylinder body of samples R5A, R5B and R5C after tribological experiments at varying 0.1 mN load	69
5.30 Presence of wear for various contact pressures and contact forces for various sample topographies	71
5.31 Threshold F_N and θ for a threshold P_{\max} of 1.7 GPa based on BES	71
6.1 Friction experiments with 1 mN load, 2 mm sliding distance and R5 samples over 70,000 cycles	73
6.2 Simplified illustration of modeled friction mechanisms	74
6.3 Simplified model of contaminant layer accumulation and removal	76
6.4 Cross-sectional profile of indentation of a ball on flat surface	78
6.5 Model of deformation on the surface along the sliding track as rectangular segments free to deform in shear mode	79

6.6 Model of cracks on the surface along the sliding track as ideal rectangular cantilevers	80
7.1 Two friction regimes can be observed in tribological experiment of R5A sample under 1 mN load	86
7.2 BES of contact at 1 mN and 0.1° tilt showing the contact width b	86
7.3 SEM cross-section image of R5A sample fractured by hand	88
7.4 Zones of critical crack propagation according to Bower & Fleck model	89
7.5 Effect of water on subcritical fracture in vitreous silica	89
7.6 Interrupted experiments under 1 mN load	90
7.7 Decrease in friction over interruption time using adsorption rate constants from experimental data of interruptions	92
7.8 A tribological experiment was performed under 1 mN load with 1 Hz cycle frequency with the linear increase subtracted	93
7.9 Model fit based on range of extracted k_r	94
7.10 Experimental results of R5A samples after 5000 cycles under 1 mN load with μ_{ad} and μ_{Ez} components subtracted.	95
7.11 Map of modeled values of a given a L and $\frac{da}{dt}$ for R5A samples after 5000 cycles under 1 mN load	96
7.12 Map of modeled values of μ given a L and $\frac{da}{dt}$ for R5A samples after 5000 cycles under 1 mN load	96
7.13 Map of modeled values of μ given a L and $\frac{da}{dt}$ for R5A samples after 5000 cycles under 1 mN load	97
7.14 Experimental μ_{Ey} compared to modeled μ_{Ey} for two sets of L and $\frac{da}{dt}$	98
7.15 Experimental μ_{Ey} compared to modeled μ_{Ey} with varying a_0	99
7.16 Experimental vs modeled friction for R5A samples under 1 mN load over 5000 cycles using the cantilever deformation model	99
7.17 Experimental friction evolution compared to modeled evolution	100
7.18 BES of various angles	101
7.19 Modeled friction evolution at various misalignment compared to experiments	102
7.20 BES of various loads	103
7.21 Modeled friction evolution at various loads compared to experiments	104
7.22 Friction evolution of 4 mN where high contact area and low contact area are observed	105
7.23 BES of various radii	106
7.24 Modeled friction evolution for various cylinder radii	107
7.25 Modeled friction evolution compared to experimental results for various surface treatments	108
7.26 BES of contact area for topographies A, B, C and D	109
7.27 Experimental results under 0.1 mN load compared to model predictions for R5A and R5B samples	110

List of Tables

3.1	Sample radii of curvature (r_1 & r_2) measured in SEM and S_a surface roughness measured on the flat surface by AFM	23
4.1	Constants for power law relationship of A and P_{\max} as functions of F_N and θ . .	41
5.1	Elemental composition from XPS analyses	63
7.1	Values extracted from numerical contact simulations of various angles	102
7.2	Values extracted from numerical contact simulations of various loads	104
7.3	Values extracted from numerical contact simulations of various radii	106
7.4	Values extracted from numerical contact simulations of various topographies .	110

List of Symbols

Symbols listed are in order of appearance.

μ	Coefficient of friction
F_T	Tangential force (N)
F_N	Normal force (N)
S_C	Hokkirigawa contact severity
P_{\max}	Maximum contact pressure (Pa)
R_t	Maximum roughness (m)
K_{IC}	Critical stress intensity factor I ($\text{Pa m}^{1/2}$)
E_{ad}	Energy of adhesion (J)
τ	Surface shear strength (N m^{-2})
H	Hardness (Pa)
r_{asp}	Asperity radius (m)
θ_{asp}	Asperity angle ($^\circ$)
γ	Surface free energy (J)
N_{asp}	Number of asperities
E	Young's modulus (Pa)
U_0	Prandtl-Tomlinson Energy Potential Amplitude (J)
k_b	Boltzmann Constant (J K^{-1})
λ	Prandtl-Tomlinson periodicity (m)
v	Sliding velocity (m/s)
v_0	Prandtl-Tomlinson velocity at zero temperature (m/s)
T	Temperature (K)
r_1, r_2	Primary and secondary radius of contact (m)
S_a	Mean height roughness of the surface of flat sample (m)
A	Contact area (m^2)
θ	Misalignment angle ($^\circ$)
$\beta_1, \beta_2, \beta_3$	Power law constants describing contact area determined from BES
η_1, η_2, η_3	Power law constants describing contact pressure determined from BES
R_a	Mean height roughness (m)
R_q	Root-mean-square roughness (m)
$R_s k$	Skewness
$R_k u$	Kurtosis
d	Sliding distance (m)
E_{Ez}	Energy of elastic deformation of indentation (J)
E_{Ey}	Energy of tangential elastic deformation (J)

τ	Surface shear strength of a bare surface (Pa)
μ_1	Coefficient of friction of a contaminated surface
μ_2	Coefficient of friction of a bare surface
$F_a d$	Adhesion force (N)
ϕ	Surface coverage of contaminant
ϕ_0	Initial surface coverage of contaminant
p	Partial pressure of contaminant (Pa)
k_a	Langmuir equilibrium constant of contaminant adsorption ($\text{Pa}^{-1} \text{s}^{-1}$)
k_r	Langmuir equilibrium constant of contaminant removal (s^{-1})
ν	Poisson's ratio
E^*	Hertzian reduced elastic modulus (Pa)
δ	Maximum Hertzian vertical deflection (m)
α	Loss constant of energy of indentation
b	Hertzian contact diameter (m)
L	Length of deformed segment (crack spacing) (m)
a	Depth of deformed segment (crack length) (m)
a_0	Initial depth of deformed segment (crack length) (m)
G	Shear modulus (Pa)
Δy	Tangential length of deformation (m)
k	Cantilever spring constant (N/m)
I	Cantilever moment of inertia (kg m^{-2})
t_g	Time of crack growth per cycle (s)
N	Total number of cycles
f	Frequency of sliding (Hz)
σ_T	Maximum tensile stress (Pa)
K_I	Stress intensity factor I ($\text{Pa m}^{1/2}$)
m_1	Paris-Erdogan proportionality constant
m_2	Paris-Erdogan exponent
t_{int}	Time of interruption (s)

List of Acronyms

Acronyms are listed alphabetically.

AFM	Atomic Force Microscopy
BES	Boundary Element Simulation
FFT	Fast Fourier Transform
FIB	Focused Ion Beam
IPA	Isopropyl Alcohol
MEMS	Microelectromechanical Systems
SD	Standard Deviation
SEM	Scanning Electron Microscopy
TCDS	Trichlorododecylsilane
XPS	X-ray Photoelectron Spectroscopy

1 Introduction

Silicon oxide is finding more and more applications in tribological systems thanks in part to the possibilities of micro-fabrication in large scales at high precision, and in part to its good mechanical properties. It is particularly of great interest in the tribological contacts of microelectromechanical systems (MEMS), which make extensive use of thermal silicon oxide layers for both electrical and mechanical properties. It has also found a niche in the horological industry, being used in various wristwatch components. At the moment, silicon oxide tribosystems show low coefficients of friction and high durability. However, there are long-term friction evolution of these contacts without lubrication is difficult to predict due to complex environmental and material phenomena.

1.1 Industry Motivation

The silicon dioxide tribosystem of study is one used in the gears of watch mechanisms. These systems are on the micro-scale in terms of size, with dimensions on the order of hundreds of micrometers. They experience forces in the hundreds of micronewtons to low millinewton range. As the edge of a gear tooth contacts the face of an adjacent gear, the geometry can be described as cylinder-on-flat. Periodic linear sliding of the contact occurs, at velocities roughly on the order of millimeters per second.

Under the conditions experienced, wear damage is not observed. High friction however, causes reduced energy efficiency. Additionally, variance in friction may cause unstable operation of the device. Therefore, the primary challenge is to develop a system that allows constant and minimal friction. In order to achieve conditions for low friction however, no lubricant may be used. Contamination of lubricants to other parts of the device may lead to unexpected behavior during operation. There are two degrees of freedom in component design, which are contact geometry and surface topography. Silicon dioxide components are fabricated within these degrees of freedom in order to meet the friction requirements.

1.2 Scientific Challenge

A scientific approach is used to address the industry challenges posed by the tribosystem of interest. Firstly, a review of the literature will be performed to determine the state of the research on tribosystems relevant to industry, considering the specific material, load and geometry conditions. In general, a tribosystem consists of the bodies in contact, the physicochemical environment, and any lubricant. This system is driven by some initial

conditions (geometry, kinetics, environment etc.), and the various mechanisms that may drive changes from the initial state. The friction and its evolution over time is based on those conditions within the contact as the number of sliding cycles increases. In order to have a tribosystem of predictable friction, it is necessary to have precise control of initial conditions and knowledge of other changes to the surface over time. For example, wear is a result of a complex sequence of phenomena that may alter the surface conditions, thereby altering friction. The interdependence and complexity of factors present a scientific challenge.

Because of the variety of factors influencing friction, experiments will be performed as close to real watch conditions as possible. Experimental sample fabrication processes will be the same as those used in watch components, with the same geometries. The effects of cleaning methods used in industry, such as alcohol rinsing, will also be investigated. The applied forces and velocity will be the same as those that are observed in watches. An experimental device will be designed with these geometries and range of forces in mind.

The initial conditions may be determined firstly by characterization of the samples prior to contact. This includes a detailed characterization of topographies and geometries. Their evolution may be observed *ex situ* after a given number of sliding cycles. By varying the experimental parameters, the primary mechanisms affecting friction in watch-relevant conditions may be determined. Following the determination of the primary mechanisms of friction, it will be possible to derive the friction force and its evolution over time. The results of the study may then be used to direct the design of the components in industry.

1.3 Thesis Structure

The approach used in this thesis is comprised of six parts: (1) a review of the literature, (2) the development of experimental systems and methods, (3) the physical characterization of the tribocontact, (4) the results of the tribological experiments, (5) the development of a predictive model and (6) an assessment of the model.

A literature review will show the state of research on the various factors affecting friction in thermally grown silicon dioxide systems under conditions that are relevant to industry applications. A range of models will be assessed, including asperity-scale models, atomistic-scale models, and empirical models. The aim of the literature review is to identify the areas that require further experimental study and further model development.

Experimental devices and protocols must be developed that allow for experimentation under watch-relevant conditions. Tribological experiments must be performed with precise contact geometries, loads and velocities. Additionally, suitable methods must be chosen to characterize sample initial conditions and their evolution over multiple sliding cycles.

Detailed characterization of the surface topography is to be performed, in order to determine sample roughness as well as contact properties. The characterization will establish

the initial state of the surface. Later on, deviations from the initial state after the experimental studies may be observed.

The experimental study is undertaken using parameters and that are relevant to watch conditions. Changes in the surfaces will be characterized according to protocols established in previous chapters. The primary phenomena affecting friction will be determined.

An applicable theoretical model will be developed, allowing for a way to quantitatively predict friction and its evolution over time. The model will consider the physical phenomena relevant to friction evolution that have been identified by the experimental study.

The predictive capability of the model will then be assessed by comparisons to experimental results. Estimated model parameters will be extracted by using a subset of experimental results. Using the extracted parameters, the model may be extrapolated to other tribological conditions, such as increased sliding cycles or increased load.

2 State of the Art

This chapter presents an overview of scientific literature, which acts to direct the experimental studies in this thesis. First, is a general overview of friction and wear, including their definitions as well as the physical mechanisms that govern their behavior. Next, the mechanisms of friction in silicon dioxide in particular are examined. Silicon dioxide friction has been investigated in number of studies under various experimental conditions. Their applicability to watch relevant conditions will be evaluated. A general overview of wear in brittle materials is also presented, including its relationship with friction. Finally, existing friction models are presented, including asperity-scale models, atomistic-scale models and empirical models.

2.1 Friction and Wear

When two bodies come into contact and experience relative motion, the force opposing the sliding motion is the force of friction. As the two bodies approach one another, contact occurs at asperities on the surface as depicted in Figure 2.1. Asperities form junctions that may adhere or deform. The friction force arises as a result of the energy required for adhesion and deformation of the asperity junctions.

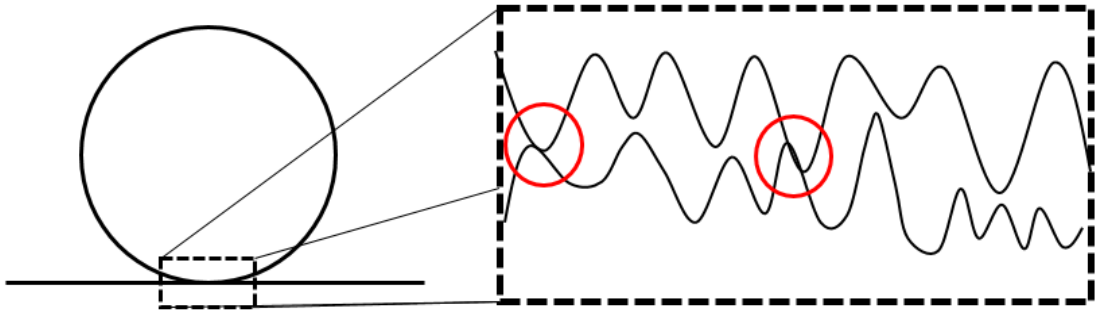


Figure 2.1 – Apparent contact (left) and asperity junctions (circled) that make up the real contact area (right)

A multitude of interrelated factors affect friction due to their influence on the adhesion or deformation of the junctions. There are broadly three ways by which friction is influenced: the total junction area, the adhesive strength of the materials, the propensity for materials to deform.

The total area of asperity junctions makes up what is called the real contact area, A_C . This is in contrast to the apparent contact area, which is the area of visibly in contact on a

macroscopic scale. The greater the real contact area the more energy is required to overcome adhesion and deformation. Contact geometry and surface topography may also affect the total area of asperity junctions. Increase in normal load may increase the area and number of asperity junctions. Due to this dependence on normal load, it is useful to characterize tangential force as a so-called coefficient of friction, μ , that is defined as the ratio of tangential force and normal force, F_T/F_N .

Adhesion occurs as a result of attractive forces between the contacting bodies. These forces can manifest due to a variety of phenomena, which influence chemical bonding between the two surfaces. The properties of the bonds, whether covalent, ionic or metallic, depend on the material properties. Additionally, intermolecular forces such as hydrogen bonding, dipole interaction or London dispersion forces may contribute to adhesion of junctions. The stress required to shear the bonds at the surface govern the effect of adhesion on total friction. The chemical state of the surface may be altered by any adsorbing species, or by material removal due to wear. Surface chemistry is sensitive to a variety of environmental factors including relative humidity, air composition, and ambient temperature. Surface contaminants may also come from sample handling, sample storage and experiment preparation.

Deformation of material can be elastic or plastic. Elastic deformation occurs when material is deformed by a stress below a yield stress criterion such that it returns to its original shape when the stress is released. The propensity for elastic deformation is characterized by elastic moduli, including Young's modulus, Shear modulus and Bulk modulus depending on whether the mode of stress is in tension, shear or compression respectively. An elastic modulus is defined as the ratio of stress to strain. The greater the modulus, the greater the amount of energy required to elastically deform a material. Applying stresses that exceed a yield stress criterion, irreversible deformation occurs, called plastic deformation. Some materials exhibit ductile behavior where they undergo large amounts of strain before fracture while some materials exhibit brittle behavior where fracture occurs soon after the strain exceeds the elastic limit, as shown in Figure 2.2. The plastic deformation behavior of the material may affect how the surface topography evolves over time as asperities are deformed.

The plastic deformation that is caused by friction may result in fracture and removal of material. This process is called wear. There are four mechanisms by which wear occurs, which are adhesion, abrasion, fatigue and tribocorrosion [1][2]. Adhesive wear occurs when junctions are strongly bonded. Fracture of the junctions occur and material is transferred between the sliding surfaces. Ultimately, particles may detach from the surface. Abrasive wear occurs when a material of greater hardness deforms one of lesser hardness. One material may cut and scratch the other generating wear particles. Fatigue wear occurs during cyclical loading. With each pass, cracks are generated and propagate until complete fracture occurs. Tribocorrosive wear occurs for metals in corrosive environments. Sliding may damage the passive film causing accelerated corrosion. Wear particles generated by any of these processes may be then be trapped in contacts to interact in the tribosystem as third bodies [3]. Third bodies may carry load, have varying geometries, travel at varying speeds, and themselves generate

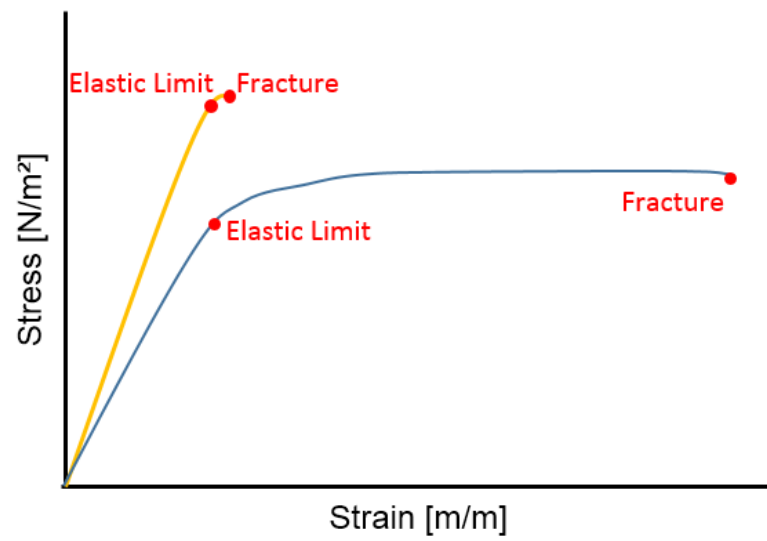


Figure 2.2 – Stress-strain behavior of a brittle material (yellow) and a ductile material (blue)

wear particles. The potential third body interactions as well as altered surface topography will further influence the friction.

2.2 Friction of Silicon Dioxide

The system of study is self-mated silicon dioxide in atmosphere conditions with no lubricant. Friction of self-mated silicon dioxide has been studied in the past, with a wide range of observations, highly dependent on experimental conditions. Reported kinetic friction has ranged widely from 0.1 to 0.77 [4][5][6][7]. Static friction of silicon dioxide has been shown to have great variance from between 0.09 and 6.7 [5][6][8][9] [10]. A list of previous friction experiments involving self-mated silicon dioxide is shown in Figure 2.3. Such large variation alludes to the sensitivity of silicon oxide surfaces to environmental conditions, and indicates the difficulty of creating a predictive model. In particular, Beerschwinger et al.[5], in particular, observed large variation in the static friction of thermal silicon dioxide samples with deviations of up to ± 0.2 . This variation was attributed to the presence of surface contaminants or adsorbed layers.

The surface of silicon dioxide consists of silanol groups and siloxane bridges, which act as sites for dipole-dipole interactions and hydrogen bonding. Adsorption of various molecules from the environment may occur on the surface of silicon dioxide, which has been shown to significantly influence friction and wear. In particular, gas and vapor adsorption on silicon dioxide, has been studied in various tribological systems. Deng et al.[10] observed static friction in silicon dioxide contacts in various gas environments. Argon, oxygen and nitrogen environments have been shown to result in greatly varying friction coefficients. Oxygen gas in particular was shown to significantly increase friction up to a coefficient of 0.75 for a thermal silicon dioxide counterpiece. On the contrary, nitrogen gas was shown to reduce friction. The mechanisms by which the adsorbed gases influence friction require further study.

Organic compounds typically adsorb onto silicon dioxide substrates at siloxane and silanol sites [11]. The adsorption of various types of organics have been observed on silicon dioxide, including small molecules, aromatics, surfactants, polymers, DNA and enzymes [11]. The presence of organics in particular has been linked to drastically reduced friction, including in silicon dioxide contacts [4][6][7]. The presence on alcohol vapor such as 1-pentanol and 1-propanol has resulted in stable friction coefficients of less than 0.2. It has also been shown that increasing 1-pentanol concentration results in more stable friction evolution over time and lower friction coefficients [7]. It has also been shown that wear is significantly decreased with upon carbon adsorption [4]. The structure of the adsorbed layer shown in Figure 2.5 (right) has been verified by simulations using a density-functional theory (DFT) model. The carbon film acts as a boundary lubricant, reducing adhesion between the sliding bodies. Alcohol adsorption has been shown to be a significant factor in the evolution of friction. In environmental conditions contamination of other organics may have significant effects. During an experiment of silicon nitride in a ball-on-flat configuration with a 3 mm ball under loads of 2 N, 10 N and 20 N, Kato has observed an increase in friction [12]. The results of the experiments are shown in Figure 2.4. It was suggested that this initial increase in friction coefficient was due to the removal of surface contaminants. This short term removal of carbon contamination shown in the experiments, requires further study.

AUTHOR	OXIDE TYPE	ENVIRONMENT	F_N	RADIUS	P_{MAX}	μ_S	μ_K
BEERSCHWINGER (1997)	Thermal vs poly-Si native	air	5-80 μN	-	1-23 kPa	0.7-0.8	0.56-0.77
	Native vs poly-Si native	air	5-113 μN	-	1-23 kPa	0.28-0.48	0.2-0.32
	Native	0-100% 1-propanol	3-120 nN	10 nm	2-7 GPa	0.2-0.4	0.02-0.12
STRAWHECKER (2005)		Ar	3-120 nN	10 nm	2-7 GPa	0.7-1.0	0.2-0.32
	Native	Air	10-100 nN	10 nm	3-6 GPa	-	0.16-0.28
CHUNG (2005) ASAY ET AL. (2008)	Native vs quartz	0% 1-pentanol	0.1 N	1.56 mm	115 MPa	-	0.2-0.6
		4% 1-pentanol	0.1 N	1.56 mm	115 MPa	-	0.1-0.3
		8% 1-pentanol	0.1 N	1.56 mm	115 MPa	-	0.25
		18% 1-pentanol	0.1 N	1.56 mm	115 MPa	-	0.2
		50% 1-pentanol	0.1 N	1.56 mm	115 MPa	-	0.17
		95% 1-pentanol	0.1 N	1.56 mm	115 MPa	-	0.15
		0% 1-pentanol	500 nN	56 μm	20 MPa	0.15	0.1-0.6
		15% 1-pentanol	500 nN	56 μm	20 MPa	-	0.1-0.3
BARNETTE ET AL. (2009)		95% 1-pentanol	500 nN	56 μm	20 MPa	0.2	0.1-0.2
	Fused silica vs native	Ar	0.1-0.7 N	1.5 mm	0.2-0.4 GPa	-	0.1-0.2
		50% n-pentanol	0.1-0.7 N	1.5 mm	0.2-0.4 GPa	-	0.15
		50% RH	0.1-0.7 N	1.5 mm	0.2-0.4 GPa	-	0.3-0.5
LIM (1990)	Poly-Si native	air	16-99 nN	-	-	3.6-6.7	-
	Native	air	1 μN	-	85 Pa	0.38	-
NOGUCHI (1991)	CVD vs native	air	1 μN	-	85 Pa	0.38	-
	Sol-gel vs native	air	1 μN	-	85 Pa	0.33	-
	PVD vs native	air	1 μN	-	85 Pa	0.09	-
	Thermal	air	50-450 μN	3 mm	11-23 MPa	0.54	-
DENG (1991)		air, after baking	50-450 μN	3 mm	11-23 MPa	0.21	-
		UHV	50-450 μN	3 mm	11-23 MPa	0.36	-
	Native vs thermal	air	50-450 μN	3 mm	11-23 MPa	0.48	-
		air, after baking	50-450 μN	3 mm	11-23 MPa	0.31	-
		UHV	50-450 μN	3 mm	11-23 MPa	0.33	-
	Sputtered vs thermal	Air	0.01-0.6 N	3 mm	65-256 MPa	0.43	-
		Ar	0.01-0.6 N	3 mm	65-256 MPa	0.2	-
		UHV	0.01-0.6 N	3 mm	65-256 MPa	0.2	-
		N ₂	0.01-0.6 N	3 mm	65-256 MPa	0.15	-
		O ₂	0.01-0.6 N	3 mm	65-256 MPa	0.75	-
	Sputtered vs native	Air	0.01-0.6 N	3 mm	65-256 MPa	0.55	-
		UHV	0.01-0.6 N	3 mm	65-256 MPa	0.39	-
		N ₂	0.01-0.6 N	3 mm	65-256 MPa	0.2	-
		O ₂	0.01-0.6 N	3 mm	65-256 MPa	0.55	-

Figure 2.3 – Static friction, μ_S , and kinetic friction, μ_K , in self-mated silicon dioxide contacts with given radius of contact, contact pressure P_{max} , and normal load F_N in various environments. A dash "-" represents no available data.

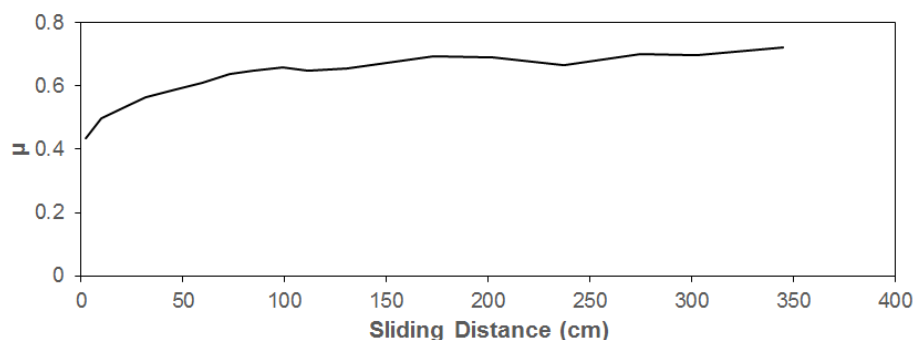


Figure 2.4 – Friction of 3 mm radius ball on flat silicon nitride in air for loads of 2 N, 10 N and 20 N. Experimental results extracted from [12]

Water vapor adsorption has shown to increase both friction and wear in tribological experiments [4]. The presence of water has also been found to induce tribochemical wear if the oxide layer is hydrated [7][13][14]. In silicon dioxide, crack propagation occurs by stress corrosion cracking [15], such that subcritical crack growth occurs at low velocities governed by the rate of chemical reactions in the crack. The chemical reaction that governs fracture in silicon dioxide is hydrolysis of siloxane bridges by as modeled in molecular dynamics simulations [16]. Further simulations have also shown that under tensile stress, the rate of water diffusion and hydrolysis may be enhanced [17]. The strong effect of water on crack propagation rate has been observed experimentally in water-immersed silicon oxide [18].

The adsorption of water has been depicted in Figure 2.5 (left), which shows the structure of hydrogen bonds based on ATR-IR spectra. It shows the transition in structure of the water film as relative humidity increases from a highly ordered structure to a liquid-like structure. The characteristics of the film depend on substrate-water interactions and on humidity [19]. Thickness may range from less than 1.5 nm at below 80% relative humidity to several nanometers at higher humidities. At very high humidities, the adsorbed liquid-like water film may result in meniscus formation due to capillary action at the contacting asperities [20]. Meniscus formation may significantly impact friction at low velocities of less than 10 $\mu\text{m/s}$, where friction forces are in the low micro-newton range as experimentally measured in 1 μm radius silica spheres [21]. At velocities greater than 10 $\mu\text{m/s}$, the meniscus effect becomes insignificant. It is suggested that at high velocities, the non-dependence of meniscus effect on velocity is due to the limited rate of hydrogen bond formation. At low humidities, highly ordered water films are formed and nano-newton scale friction forces are observed in silicon dioxide [22]. Non-hydroxylated surfaces experience low friction forces independent of humidity. For hydroxylated surfaces, the dominating mechanisms by which friction is influenced varies. At less than 1 μPa partial pressure, water adsorption acts as a lubricant reducing friction, while at greater partial pressures, hydrolysis may significantly increase surface hydroxylation and friction. The potential effects of water on friction prove to be complex and may also be affected by other competing adsorbent species. The prediction of the evolution of friction under such conditions would require further study.

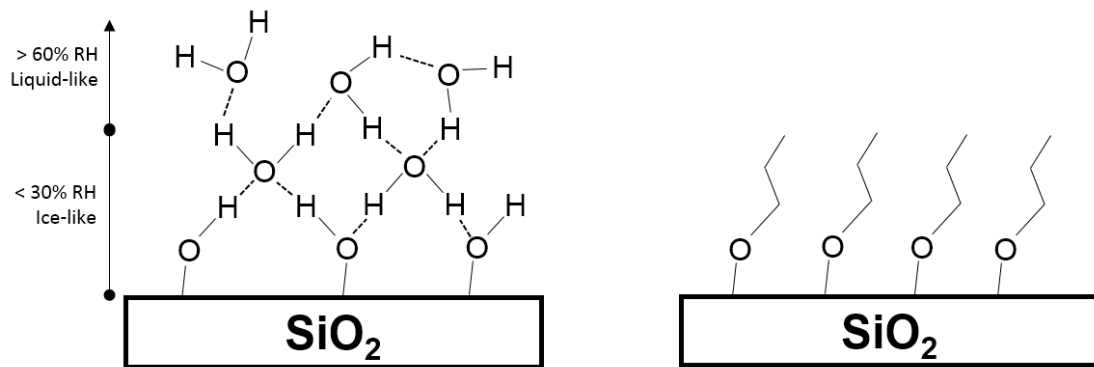


Figure 2.5 – Left is the structure of an adsorbed water layer on silicon dioxide. Right is a depiction of chemisorption of 1-propanol on silicon dioxide.

2.3 Wear of Silicon Dioxide

The wear of silicon oxide generates particles, which may modify the friction by a number of mechanisms. For example, these particles can remain between the two bodies in contact and can accommodate movement and reduce friction by rolling[4]. Contrarily, at the same time, the energy of fracture and generation of wear particles may greatly increase friction[4]. In particular, it has been shown that silicon dioxide, at temperatures close to room temperature, generally exhibits brittle fracture [24]. There have been numerous studies that explain wear behavior in brittle materials.

Initially, cracks propagate perpendicular to the surface, as has been shown both experimentally and theoretically from analysis of stress fields in a contact [25]. It has been verified experimentally where surface cracks have been observed a scratch to a diamond surface [25]. The cracks propagate initially perpendicular to the surface on the trailing edge of the contact. Crack width in this case is approximately $1\ \mu\text{m}$ and cracks are spaced $0.3\text{-}0.4\ \mu\text{m}$ apart. As cracks propagate, their intersection leads to material removal and wear [26].

Kato identifies three primary wear modes that typify tribological contacts of brittle materials: (1) powder formation, (2) flake formation, and (3) steady ploughing [27]. Powder formation occurs at low number of cycles where cracks are very short. Fracture on the asperity scale causes formation of very small wear particles. As the number of sliding cycles increases, larger cracks form and flake formation occurs. It occurs on the scale of the apparent contact area, and is due to the cracking phenomena shown previously by Lawn. Illustrated by Figure 2.6, as cracks grow longer they propagate beneath the surface parallel to the direction of sliding. Upon resurfacing or intersection with another crack, a wear particle is detached from the surface. The third wear mode of ploughing occurs at low stresses or after a large number of cycles. In this mode, no additional particles are formed though existing particles may be ejected from the contact. Later on, Kitsunai & Hokkirigawa proposed an additional mode of

deformation, which is crack generation occurring at high loads. Wear particles are not form, but cracks propagate within the material as a precursor to flake formation [28].

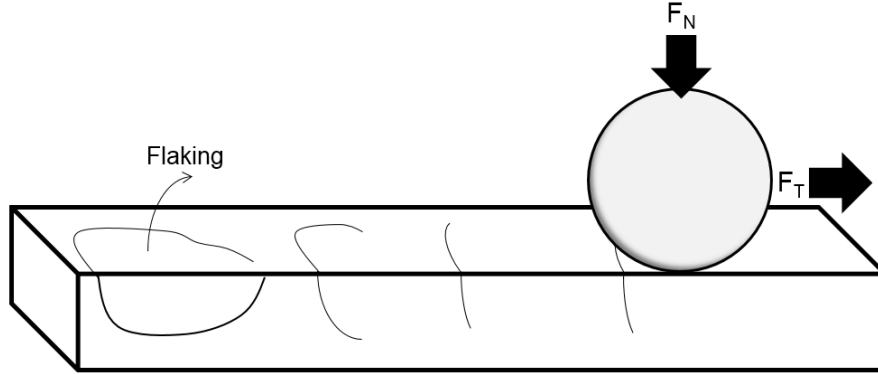


Figure 2.6 – Mechanism of flake formation as cracks propagate below the surface in the direction of sliding.

A parameter termed "contact severity", S_C , was used as a characteristic property of the contact, defined:

$$S_C = \frac{P_{\max} \sqrt{R_t}}{K_{IC}} \quad (2.1)$$

where P_{\max} represents the maximum pressure, R_t represents the total roughness height and K_{IC} represents the plane strain fracture toughness. The relationship between contact severity and friction force predicts the mode of wear that is observed. The empirically determined equations are shown as follows:

$$\text{Flake Formation:} \quad S_C \geq \frac{7}{1 + 10\mu} \quad (2.2)$$

$$\text{Powder Formation:} \quad \frac{7}{1 + 10\mu} > S_C \geq \frac{5}{1 + 10\mu} \quad (2.3)$$

$$\text{Ploughing Formation:} \quad \frac{5}{1 + 10\mu} > S_C \quad (2.4)$$

With high contact severity, or high frictional force, flaking is more likely to occur over powder formation and larger wear particles are observed.

2.4 Modeling of Friction

Classical friction behavior is typically described as Amonton-Coulomb behavior, which is described by three quantitative propositions [1]: (1) friction is proportional to the normal force, (2) friction is independent of apparent contact area, and (3) friction is independent of sliding velocity. Bowden & Tabor [29] have formulated an expression to explain Amonton-Coulomb

behaviour based on the plastic deformation of materials during sliding, as follows:

$$\mu = \frac{\tau}{H}$$

where μ represents a friction coefficient, τ the shear strength at the surface, and H the material hardness. For systems with low plastic deformation, this expression may not sufficiently describe the phenomena governing friction.

Rabinowicz [30] has expanded upon the Bowden & Tabor model accounting for asperity adhesion between the two counterpieces, which gives the following:

$$\mu = \frac{\tau}{H - 2W_{ab}(\cot\theta_{asp})/r_{asp}}$$

$$E_{ad} = \gamma_a + \gamma_b - \gamma_{ab}$$

where E_{ad} the work of adhesion between the two bodies, γ the surface free energies of the bodies a and b with respect to air or each other, θ_{asp} the asperity angle and r_{asp} the asperity junction radius of contact. This allows for incorporation of surface chemistry effects. Like the Bowden & Tabor model, it is based on plastic deformation of asperities. Furthermore, extension of the model would be necessary to describe time-dependent phenomena.

In cases of purely elastic deformation, it has been shown that the Amonton-Coulomb proposition of friction proportionality with normal force does not hold. Lincoln [31] observed in experimental results that friction coefficient variance with normal force in a ball-on-flat elastic contact follows the relationship:

$$\mu = \frac{F_T}{F_N^{2/3}}$$

This relationship is attributed to the increase in real contact area within a contact upon elastic deformation. Based on equations of Hertzian contacts, the real contact area is related to the load by the power of $2/3$ for a single spherical asperity on a plane surface as follows:

$$A_{real} = cN_{asp}^{1/3} \left(\frac{F_N r_{asp}}{E} \right)^{2/3}$$

where A_{real} represents the real contact area, c a constant, N_{asp} the number of asperities, and E the elastic modulus. It has later been shown that in some elastic contacts the relationship between μ and F_N may be greater than $2/3$ [32][33]. Lodge & Howell [33] have shown the following based on Hertzian equations:

$$\mu = \frac{F_T}{F_N^n}$$

where n is a constant greater than $2/3$ dependent on contact geometry. In cases two equal spheres or crossed cylinders n may be $8/9$. Certain simple geometries such as these are

solved analytically [34]. For other more complex geometries, such as those found in watch mechanisms, numerical simulations of the Hertzian contact are necessary. Further extension of the model would be necessary to describe effects of time-dependent phenomena.

A generic friction model at the asperity level has been developed by Al-Bender *et al.* [35]. The model takes into account creep, adhesion and deformation of asperities under load. Asperity junctions are modeled as ideal springs in the normal and tangential directions. The parameters of the Al-Bender *et al.* model are not mechanistically defined and would require expansion to incorporate physical mechanisms.

A range of friction models have been used in the study of earthquake faults. The Dieterich model [36] was initially developed to describe the connection between static and sliding friction with a parameter describing contact state based on junction lifetime. Ruina & Rice developed the rate-state model [37] describes friction based on the state of slip velocity. The Perrin-Rice-Zheng model [38] modified its predecessors to incorporate junction lifetime and slip velocity. These models seek to explain friction phenomena at very low sliding velocities relevant to geological length scales. Additional models designed to model earthquake faults, the Burridge-Knopoff model [39] and its derivative the Burridge-Knopoff-Carlson-Langer model [40] represent contacting bodies as a series of masses coupled with springs sliding on a smooth surface. These models do not describe friction in terms of measurable topographical characteristics.

Atomic-molecular scale models are often used to represent friction of smooth surfaces. The classical atomistic description of friction is the Prandtl-Tomlinson [41][42]. It was originally formulated to describe motion of atoms in a crystal lattice, but has since been applied also to tribological systems. Shown in Figure 2.7, the model describes a point mass dragged with a damped spring through a periodic potential. Physically, this may be representative of an atom sliding across the surface of a smooth perfect crystal lattice. For a series of point masses connected to a rigid body, the frictional force F_T is described as follows:

$$F_T = 2U_0/\lambda + (2k_B T/\lambda) \ln(v/v_0)$$

where U_0 represents the peak-to-peak amplitude of the an energy potential, k_B the Boltzmann constant, T the temperature, λ the spatial periodicity of the crystal lattice, v the velocity of sliding and v_0 the velocity at zero temperature. This equation is valid for forces satisfying the following condition.

$$kT \ll F_T \lambda/2 \ll U_0$$

The Prandtl-Tomlinson model has been extended by others such as in the Frenkel-Kontorova model [43] where atoms are elastically coupled in a harmonic chain. This elastic coupling allows representation of fluid-like long range interaction between atoms that occurs in adsorbed monolayers on an atomically flat surface [44]. A feature of the Frenkel-Kontorova model is zero static friction force. The two have been combined into a Frenkel-Kontorova-Tomlinson

model to more accurately represent systems with non-zero static friction [45][46]. These models require smooth surfaces with no adhesion, with sufficiently low temperatures or high energy potential wells. Additionally, the amplitudes of potential wells are not mechanistically described based on measurable material characteristics.

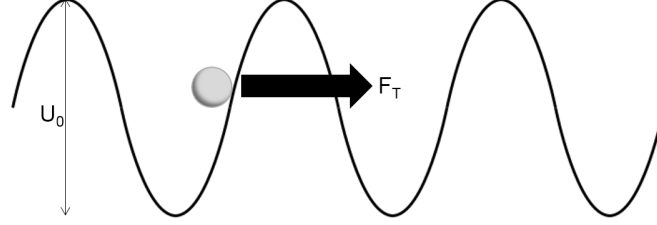


Figure 2.7 – Illustration of the Prandtl-Tomlinson model, with a mass in a potential field, being dragged with force F_T across a potential field of amplitude U_0 .

Aside from the previously described models based on descriptions of physical phenomena, there are also a range of friction models that are generalized empirical models often applied in control systems for friction compensation, such as in high precision motion control of micro-manufacturing. Static friction models have been developed that describe break-away friction behavior. The most simple is a formulation based on the empirical Amonton-Coulomb observations describing friction as a constant with respect to velocity. The so-called Coulomb model is expressed as follows:

$$F_T = F_c \operatorname{sgn}(v)$$

where v is the sliding velocity and F_c the coulomb friction force. The model fails to represent any transition from stiction around zero velocity, which the Karnopp model [47] and the reset integrator model [48] were designed to incorporate. Other expansions to the Coulomb model have been made to incorporate velocity-dependent effects, time-lag effects and hysteresis. Further developments have allowed incorporation of phenomena observed in different lubrication conditions, such as a combined model [49] incorporating stiction, velocity-dependent effects and viscous friction. Furthermore, a so-called seven parameter friction model [49] was developed to additionally model effects of rising static friction from dwell time frictional memory and presliding displacement. These models describe friction behavior at breakaway rather than kinetic friction during maintained sliding.

For kinetic friction, state-variable models better show the effects of hysteresis and dependence on sliding history. These models depend on differential equations representing the state of a contact given certain parameters such as velocity, position or time. They are used to describe friction evolution over a single cycle. The most simple dynamic model is the Dahl Model [50] which models hysteresis in oscillating sliding, shown as follows,

$$\frac{dF_T}{dt} = vk(F_T - F_0 \operatorname{sgn}(v))^2$$

where k represents an effective spring constant, and F_0 peak sliding friction level. The model results in a generic hysteresis loop with one parameter as shown in Figure 2.8.

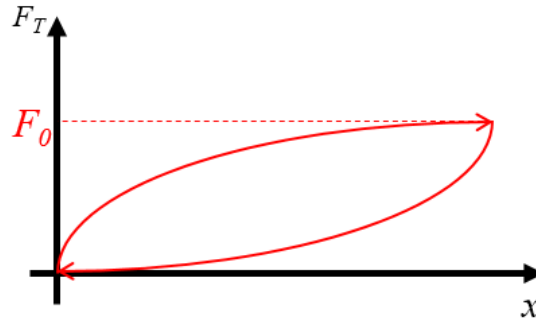


Figure 2.8 – Generic hysteresis loop of tangential force as given by the Dahl model

A number of models have been developed from the Dahl model. The LuGre model [51] introduces a parameter to allow change in friction at constant velocity. The elastoplastic model [52] was developed to increase accuracy of the LuGre model to account for drift in the position at low velocities. Further, the Leuven model [53] has been developed to account for frictional memory. The generalized Maxwell-Slip model [54] was developed from the Leuven model. It incorporated stick-slip phenomenon to describe presliding friction that governs the hysteresis behavior. These models are designed to be heuristically fit with experimental results, and are not based on physical mechanisms for friction behavior.

2.5 Outlook

Previous studies have shown various experimental results of silicon dioxide friction under different conditions. Different types of alcohol vapor, gas and humidity environments have shown a great impact on the friction. The change in the state of surface adsorption over time has been suggested to affect friction evolution. In the watch industry, a variety of substances are used in the production of components. Furthermore, while there is no lubricant, it is a system exposed to atmospheric conditions, which may lead to adsorption of gases in the air or contaminants from its surroundings. The specific impacts of the industrial methods used and the environmental exposure on friction will need further study. Furthermore, friction experiments have thus far been performed either at nano-scale forces and dimensions using MEMS devices, or at traditional millimeter scale dimensions. There has been a lack of studies under watch-relevant micro-scale conditions. An experimental device must be designed that will allow experiments in the required ranges of load and size.

A variety of friction models exist that can be broadly categorized into three categories: empirical, atomistic scale and asperity scale. Empirical models allow heuristic fitting observed friction behavior, but do not explain physical mechanism of friction that would be necessary to predict friction evolution from measurable characteristics. Atomistic scale friction models

cannot account for macro-scale phenomena without further adaptation. Asperity scale friction models may be applied, which take into material characteristics such as contact area and surface shear strength. Regardless, all models require expansion to incorporate time and cycle dependent effects to predict friction evolution. In order to expand the models for time dependence, the behavior of the relevant friction phenomena over time must be further studied.

The literature overview shows the need for experiments to be designed specifically for watch-relevant conditions. An experimental device that allows for well-defined micro-scale geometries at micro-scale loads must be developed. The tribological behavior of the material may be determined by an experimental study, such that the relevant phenomena influencing friction may be identified. A mechanistic model may then be developed based on these phenomena that allow for prediction of friction evolution over time.

3 Methods

This chapter provides an overview of the experimental system developed for the tribological study, as well as the characterization methods used for sample analysis. A device is developed that allows for samples of micro-scale dimensions, at micro-scale loads, with well defined sample geometry. The limits of the experimental system and sample properties are determined. Furthermore, a number of analytical tools are described, which allow for physical and chemical characterization of the surface, both qualitatively and quantitatively.

3.1 Tribological Experiments

3.1.1 Tribometer Specifications

A tribometer was delivered by an external supplier, the BASALT N-2 from Tetra GmbH (now AvateraMedical GmbH). The tribometer was prepared with a number of custom features allowing for the stringent precision requirements in alignment and measurement. It allows experiments to be performed in an reciprocating linear sliding configuration. The enclosed experimental area of the tribometer is shown in Figure 3.1. Also shown are the two components of the sample holders, one on top fixed to a cantilever, and one on the bottom fixed to a moving stage with rotational control on all three axes.

During operation, the base oscillates along the y-axis (inward and outward), and z-displacement is adjusted by vertical movement of the carrier module. Load is measured by deflection of the cantilever in the y and z-axes by capacitive sensors. The tribometer includes a temperature sensor and a relative humidity sensor. Sensor accuracy has been verified by external sensors, including a thermocouple for temperature and a hair tension hygrometer for relative humidity. The sample holder sits on a tilt stage, with the center of rotation being a fixed point, where the sample bodies are designed to come in contact. Along the x and y-axes are two fixed-focus black and white cameras. Focal points of the cameras can be adjusted by adjusting their positions via screws on the rear of each camera. Precise rotational alignment is performed from the camera images with a pixel size of 2 μm . The stage allows angle adjustment of approximately 0.1° precision, measured by camera imaging. The experimental area is enclosed by acrylic doors which prevent disturbances by external air flow. The enclosure is not airtight however, so experiments must be performed in room conditions.

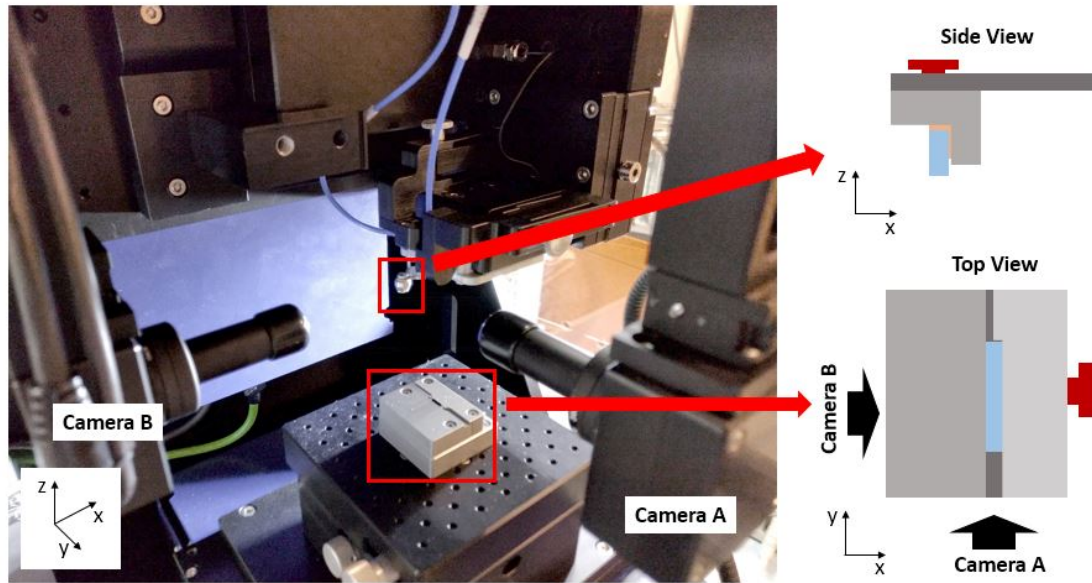


Figure 3.1 – Photo of tribometer experimental area, including sample in the sample holder on a rotating stage.

3.1.2 Sensor Calibration

The cantilever used is designed to work in the low milli-Newton range between 0.1 mN and 10 mN, though cantilevers of 100 mN and 1000 mN maximum loads have also been supplied. Cantilevers were delivered manufacturer provided calibration constants, and have been verified experimentally. Linear response of the 10 mN cantilever has been verified by controlled displacement tests. The cantilever is brought into contact with a fixed surface, upon which, force is gradually applied. The measured load is correlated to the displacement in order to determine the spring constant of the cantilever, the plot of which is shown in Figure 3.2. The vertical and lateral spring constants are found to be 33.745 mN/mm and 36.986 mN/mm respectively.

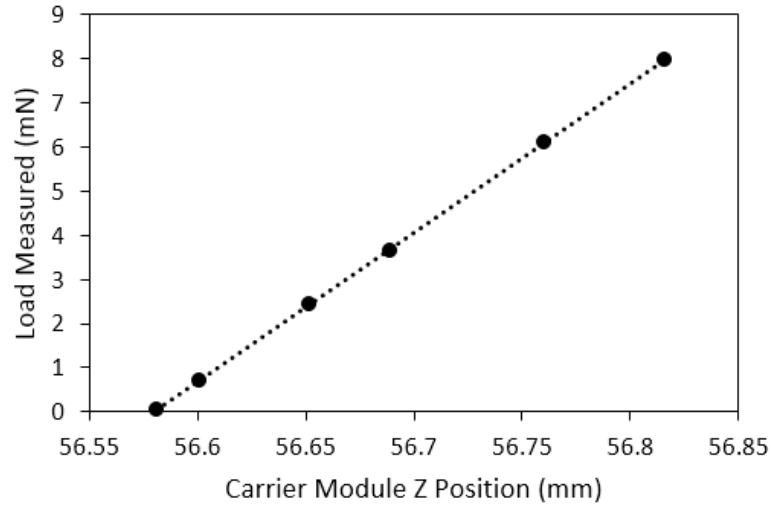


Figure 3.2 – Calibration curve of cantilever used to derive spring constant

3.1.3 Sample Design

Samples are specially designed as close to real watch component specifications as possible. Geometries and fabrication processes match those used industrially. The design must be made to allow for precise alignment of the upper and lower bodies. The idealized geometry is cylinder-on-flat. However, in reality, the contact geometry is as shown in Figure 3.3). The cylinder counterpiece may be misaligned such that contact occurs on one edge. As such, the contact can be characterized by two radii of curvature, r_1 and r_2 .

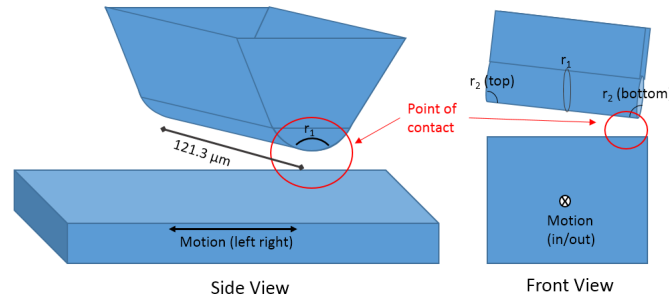


Figure 3.3 – Illustration of the geometry of the contact of a misaligned cylinder on flat surface.

The width of the cylinder is 121.3 μm . The lower body is designed to be a flat surface 4 mm in length and 300 μm in width. The manufacturer provided elastic modulus is 70 GPa, and the poisson ratio is 0.17. SEM imaging of a cross-section, shown in Figure 3.4, also verifies oxide thickness to be 3.02 μm . The primary radius r_1 and secondary radius r_2 are listed in Table 3.1. The cylinder radius is not uniform throughout its length. Thus, the radii of curvature on the top and bottom faces of the cylinder have been measured and listed separated. Experiments are to be performed with the contact point on the bottom edge of the cylinder. SEM imaging

was used to precisely measure sample dimensions. The radius of the profile from the direction perpendicular to sliding is verified in Figure 3.5 (left). The secondary radius may be observed under SEM as shown in 3.5 (right). The secondary radius can reach as low as $2\text{ }\mu\text{m}$ measured over an average three samples. Depending on the angle of the cylinder misalignment, the actual contact geometry may approach that of an ellipsoid on flat with characteristic radii r_1 and r_2 .

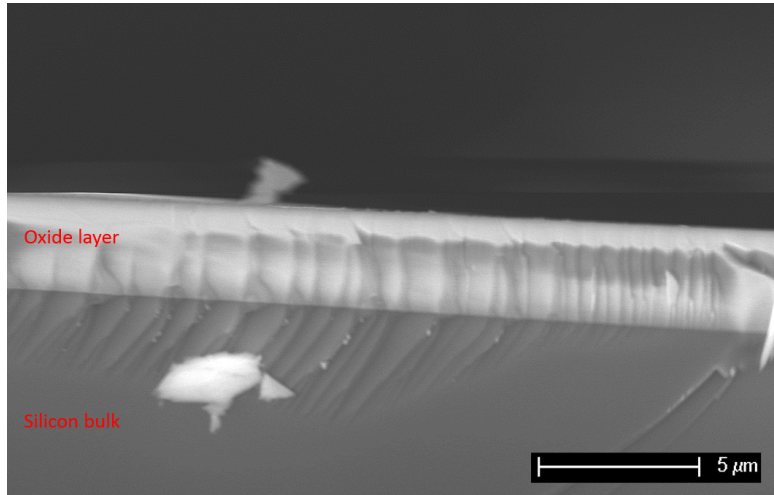


Figure 3.4 – SEM image of a cross-section of a sample fractured by hand. Bright particles are debris generated during fracture of the wafer.

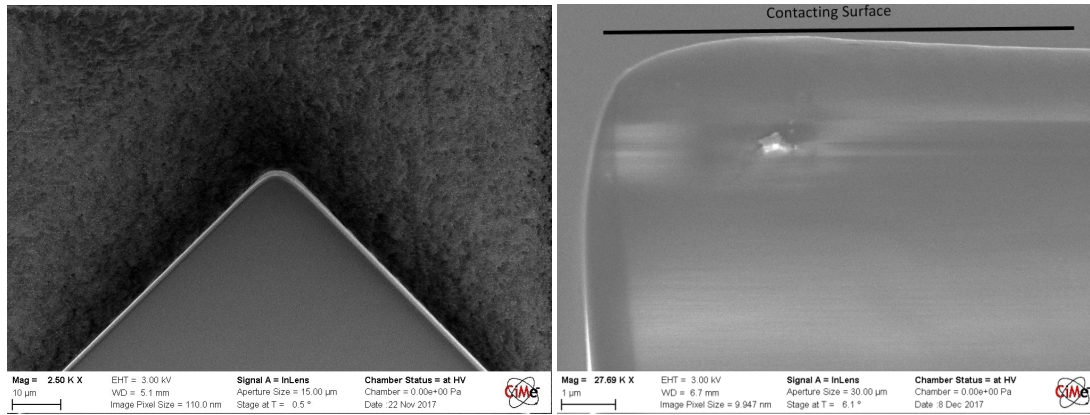


Figure 3.5 – SEM images of a sample from the side perpendicular to sliding (left) showing primary radius and from the side parallel to sliding (right) showing the secondary radius of the corner.

The upper cylindrical contact was fabricated with varying expected radii of curvature of $5\text{ }\mu\text{m}$, $10\text{ }\mu\text{m}$ and $20\text{ }\mu\text{m}$, so the samples are aptly named R5, R10 and R20. Samples of varying topography have also been fabricated. These samples are named A, B, C, and D. They are characterized by their roughness by arithmetic mean S_a measured over a 10 mm^2 on the

flat surface, also displayed in Table 3.1. More detailed surface topography analyses are to be performed using the methods outlined in the following sections.

Table 3.1 – Sample radii of curvature (r_1 & r_2) measured in SEM and S_a surface roughness measured on the flat surface by AFM. Bottom and top surfaces of the cylinder (refer to Figure 3.3) have different radii of curvature.

Name	Top r_1 (μm)	Bottom r_1 (μm)	Top r_2 (μm)	Bottom r_2 (μm)	S_a (nm)
R5A	5.85	5.33	2.06	1.87	6.29
R5B	5.85	5.33	2.06	1.87	12.72
R5C	5.85	5.33	2.06	1.87	15.13
R5D	5.85	5.33	2.06	1.87	461.7
R10A	8.94	8.69	2.26	2.37	6.29
R20A	19.94	18.74	2.92	2.65	6.29

The cylinder bodies of Samples R5A, R5B, R5C and R5D were imaged under SEM, revealing the various surface topographies, as shown in Figure 3.6. Contact occurs only on one edge of the cylinder when misaligned, and is indicated by the red arrow. SEM images of the cylinder may be compared after an experiment to observe tribological behavior.

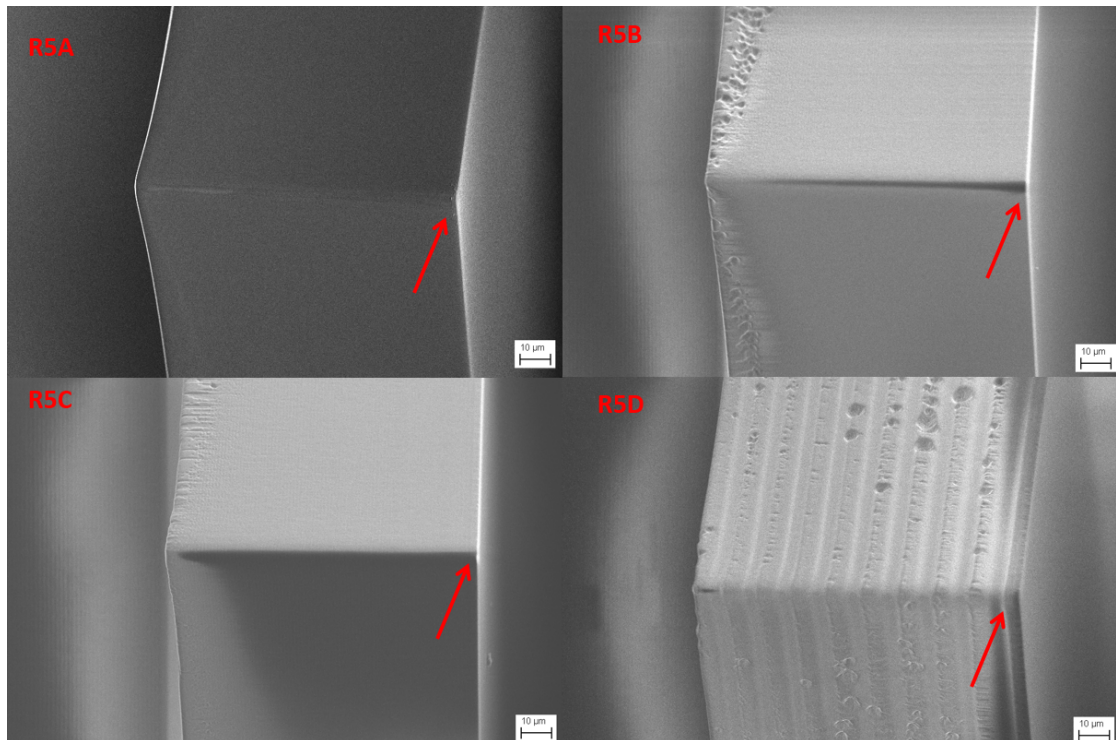


Figure 3.6 – SEM images of cylinder body of samples R5A, R5B, R5C and R5D prior to tribological experiment. Red arrows indicate point of contact

A special sample design was made in order to ensure reproducible alignment between upper and lower counterpieces. This design as depicted in Figure 3.7, consists of both upper and lower counterpieces joined by breakable limbs. The limbs fix the alignment of the upper and lower counterpieces, such that every sample will have the same alignment. Only after samples are mounted may the limbs be broken to allow independent motion of the bodies during experiments. Experimental samples are fabricated by dry etching of silicon wafers with a 3 μm layer of thermally grown oxide. They are stored at room temperature in desiccators to limit exposure to moisture.

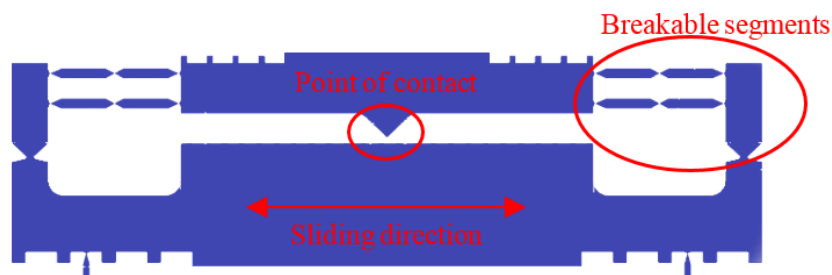


Figure 3.7 – Designed sample etched from thermally oxidized silicon wafer with sliding surface length of 4 mm

3.1.4 Sample Mounting

A detailed method for mounting the sample has been developed for precise and reproducible alignment between the two sample counterpieces. Prior to mounting the sample, the stage should be well aligned. Preliminary alignment of the stage is performed with displacement gauges attached by screws to fixed points on the carrier module. Alignment of rotation around the z-axis is performed with the lateral displacement gauge, shown in Figure 3.8 (left). The gauge probe must first be placed against a straight edge along the y-axis such that it measures the x-displacement. While sliding along the y-direction, rotation around the z-axis should be adjusted such that the gauge shows zero displacement in the x-direction. Alignments of rotation around the x and y-axes are performed with the vertical displacement gauge, shown in Figure 3.8 (right). It must first be placed on a flat surface such that it measures the z-displacement. The stage is then moved in the x-direction while rotation around the y-axis is adjusted such that the displacement of the gauge in z is constant. The same is performed for the x-axis rotation by moving the stage along the y-direction.

The sample holder consists of two parts. The sample is mounted to the two parts as shown in Figure 3.9. There are four steps: (1) mounting the sample to the bottom sample holder, (2) attaching the upper sample holder to sample with glue, (3) separating the upper and lower components of the sample by breaking the breakable limbs, and (4) allowing the glue to fully cure.

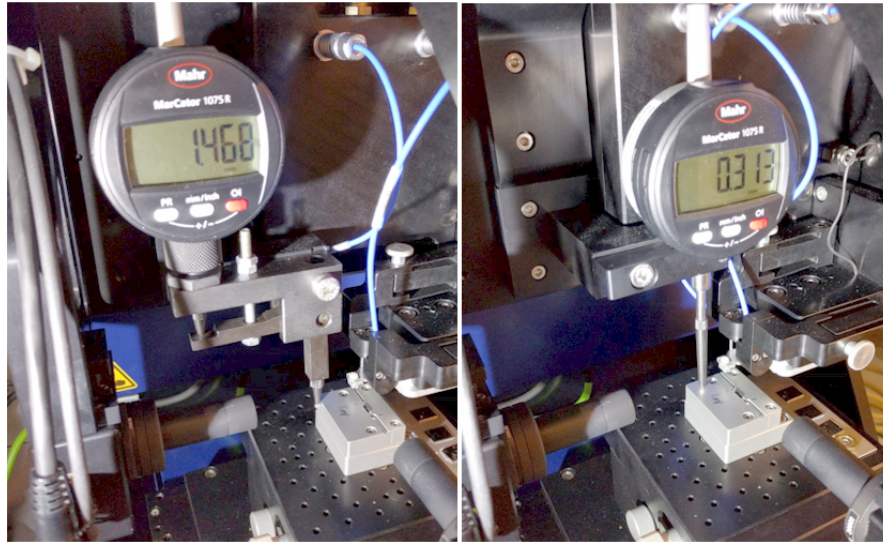


Figure 3.8 – Displacement gauges are used to align the edges and surfaces for rotation around the z-axis (left) and rotation around x and y-axes (right), shown in the proper positions for angle alignment.

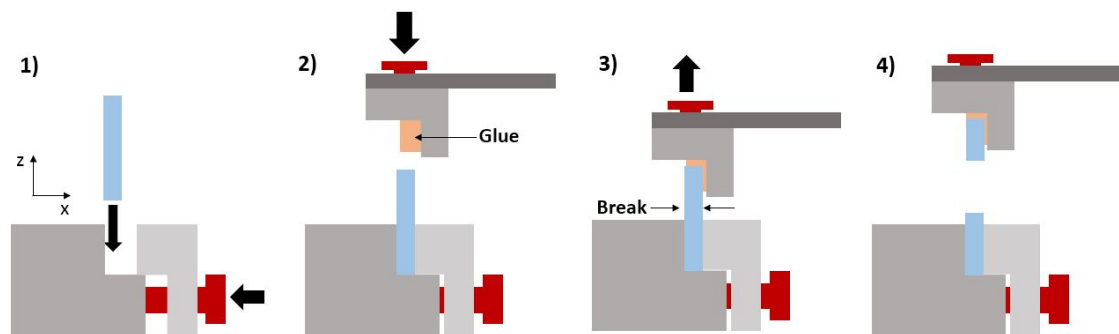


Figure 3.9 – The four steps of mounting the sample viewed from Camera A perspective. (1) Mounting the sample to bottom holder (2) attaching top holder to sample (3) separation of top and bottom counterpieces (4) allowing glue to cure

In step (1) of Figure 3.9, The sample is first fixed to the bottom sample holder. This is done in a laminar flow cabinet to minimize outside contamination. The sample is oriented such that the top of the wafer is facing away from the screw head. The sample is then pushed flush with the edges of the sample holder and gently screwed in place. The sample holder is screwed to the stage while applying gentle force with the hands towards the inner right in order to ensure reproducible positioning. The tightness of the screw holding the sample is verified to ensure a strong hold.

The upper sample holder is screwed onto the cantilever. Care must be taken to avoid damaging delicate cantilevers. Gel-type acrylate-based glue, UHU Extra All Purpose Adhesive, is applied with a needle to coat the upper sample holder. The cantilever is then be firmly screwed onto the cantilever module of the tribometer. Capacitive sensors should be adjusted such that the output is within the acceptable range, as specified by the tribometer software,

and the sensors should be zeroed. In step (2) of Figure 3.9, the sample holder is lowered onto the sample. Using the two camera views, shown in Figure 3.10, the upper sample holder may be guided to the sample. Final adjustments to rotational alignment should be performed before attachment of the sample to the upper sample holder. The sample can then be glued to the sample holder by moving them into contact to apply a load of approximately 6 mN.

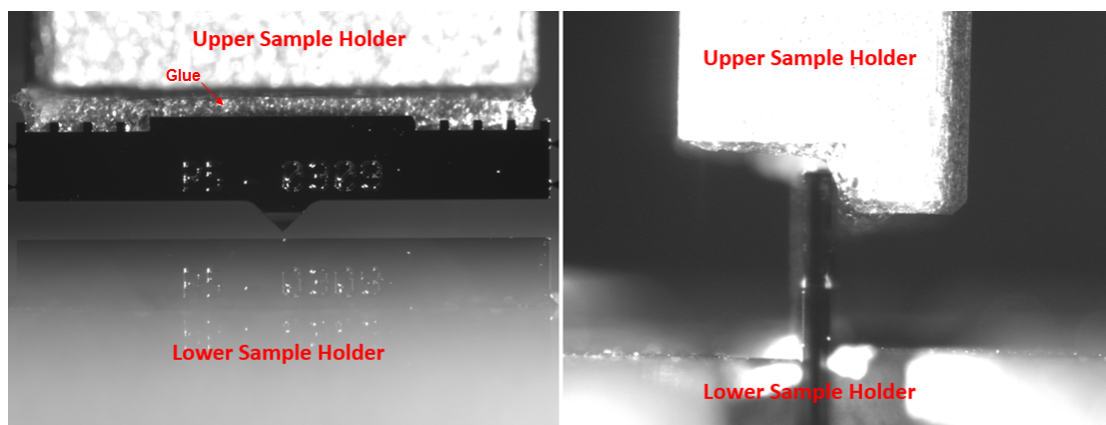


Figure 3.10 – Camera B view from the side (left) and Camera A view from the front (right) of a sample (black) glued to the sample holder (white). The layer of glue is visible between the sample and sample holder.

In step (3) of Figure 3.9, breakable limbs are removed. The carrier body is first slowly raised to reduce the load to -2 mN. With tweezers, all of the small breakable segments, shown previously in Figure 3.7, can be gently broken. The upper sample can then be raised freely.

In step (4), The sample is then left overnight to ensure that the glue is fully cured before the experiment begins. Before start of the experiment, angle alignments are verified and adjusted if necessary. The contact should also be positioned and aligned with the camera, as shown in Figure 3.11. Tribometer software limits x position precision to 0.1 millimeters.

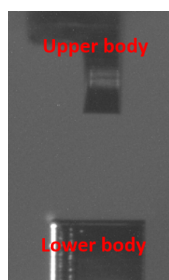


Figure 3.11 – Camera A view for alignment of sample before experiment. Contact angle can be estimated from the camera image. Sliding is controlled by movement of the lower body in the direction in and out of the page.

3.1.5 Experimental Conditions

The tribometer operates in fix-position mode where it maintains the cantilever module position throughout the duration of the experiment. Fixed-position mode is very sensitive to sliding inclination, shown in Figure 3.12. The precision alignment capabilities of the device, which includes the cameras and the tilt stage, allow control of the sliding inclination.

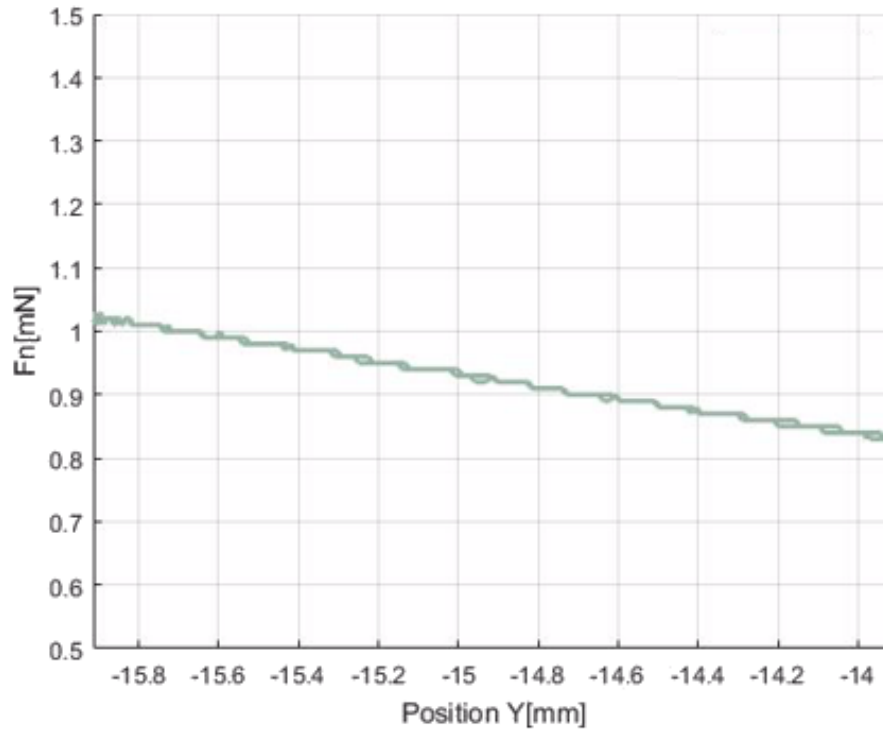


Figure 3.12 – Normal force of one cycle in fixed-displacement experiment with an inclined sample

At a room temperature of 23°C, the temperature within the apparatus enclosure during operation is between 32-33°C due to heat from the surrounding electronics. The variance in temperature and its impact on frictional force is shown in Figure 3.13. During this long-term tribological experiment, there was an initial load of 1.02 mN, which fluctuated over the course of the day. Fluctuation in load may related to thermal expansion and contraction, or temperature dependence of elastic modulus of various parts of the device. The maximum fluctuation of normal load was approximately 0.06 mN, which corresponds to approximately 1.8 μm of sensor displacement. Relative humidity is approximately 60% as measured by a hair hygrometer in the device encolsure.

Experiments are performed at 8 mm/s average velocity with 2 mm stroke length. Cycle frequency as low as 1 Hz can be achieved, corresponding to 2 strokes per second. Normal loads of between 0.1 and 2 mN are targeted in order to emulate the real conditions. The starting position of each cycle is at the end of the stroke closest to front of the device.

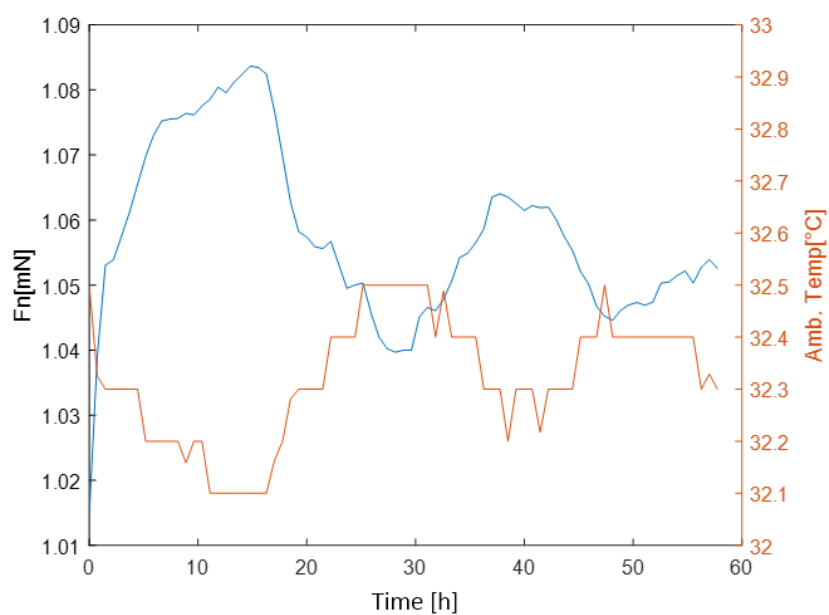


Figure 3.13 – Temperature evolution over 60 hours and its effects on normal load.

After the experiment, the glue is removed by soaking the upper sample holder and sample in acetone, in an ultrasonic bath for 3 min. The samples are finally stored for later analysis in ambient room conditions.

3.1.6 Data Post-Processing

Data is processed using MATLAB scripts. The number of cycles recorded by MATLAB for post-processing is an adjustable parameter. For time-efficient data analysis, the dataset should be less than 100 000 points. This section describes the post-processing steps taken, in the order they are applied to the dataset.

Positions along the y-axis is reported by the device based on stage position. This is adjusted to be the real sample position by subtracting spring displacement, resulting in the shift shown in Figure 3.14. Spring displacement is calculated from the spring constant, from Section 3.1.2, and the output tangential force.

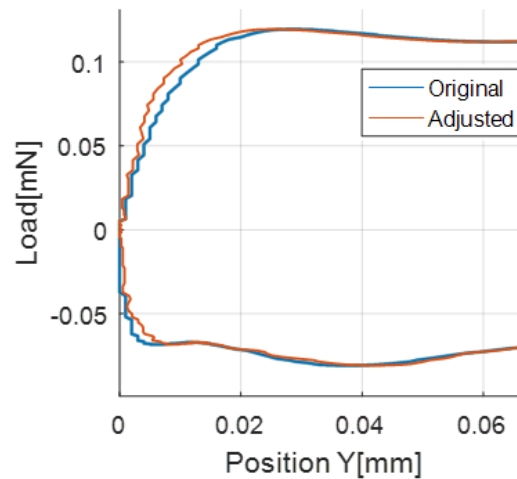


Figure 3.14 – Tangential force output adjusted for cantilever deflection

Velocity and acceleration are calculated as the first and second order differentials of the position, given the sampling rate of 1000 Hz. Velocity is filtered with a 4th-order Butterworth low-pass filter of 30 Hz, the result of which is shown in Figure 3.15. The velocity or acceleration of a given point is the average of the differences with its two directly adjacent points.

X and y-positions are output as co-ordinates of the stage position within the device. This can vary between experiments. Therefore, all positions are offset such that their minimum values are zero. Zero y-position thus corresponds to the starting position of the cycle.

The 10 mN cantilever is observed to have a mechanical resonant frequency of 25-35 Hz, depending on the mass of the attached sample shown in Figure 3.16. A 4th-order Butterworth low-pass filter is used on the tangential force, and normal force outputs. This filter introduces a signal delay of approximately 30 ms, shown in Figure 3.17, thus the signal is shifted in time accordingly to compensate. It is the same filter is applied earlier to velocity. The RMS deviation of the signal from the filter is also calculated as a moving average with a range of 30 points.

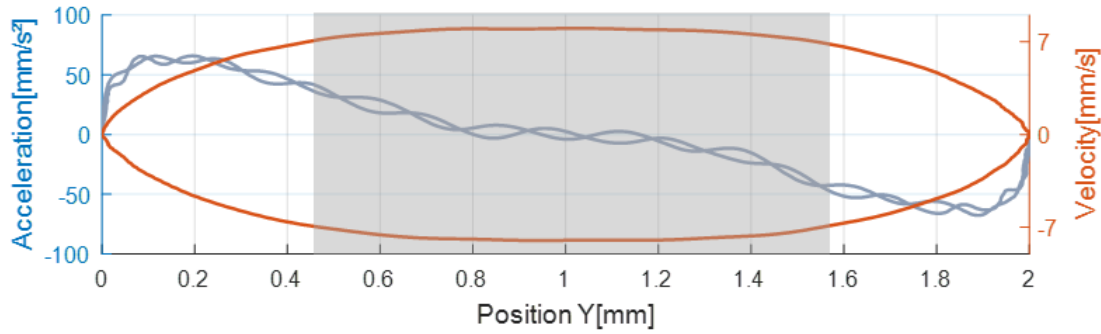


Figure 3.15 – Calculated velocity (30 Hz low-pass filtered) and acceleration from the differential of Y position. The gray region depicts the zone where friction data is recorded (threshold of 12.5% of maximum velocity).

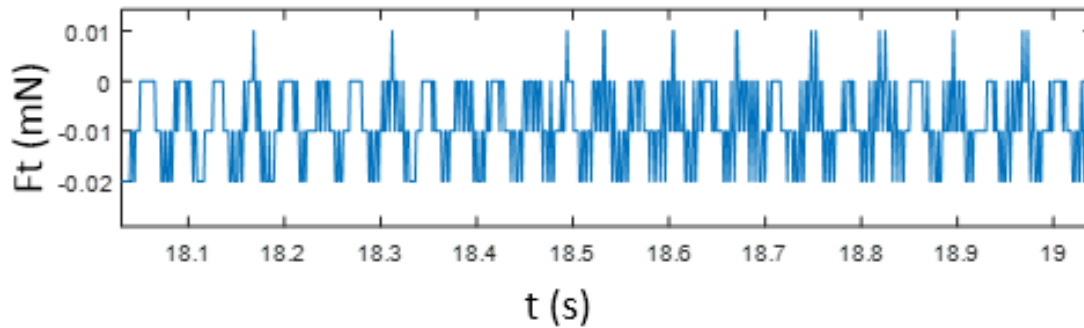


Figure 3.16 – Mechanical resonance of the cantilever in air of approximately 28 Hz

After the aforementioned processes, coefficient of friction is recalculated using the adjusted and filtered values. Coefficient of friction is calculated as the direct ratio of tangential force to normal force.

From each cycle, the averages of coefficient of friction, tangential force and normal force are extracted, shown for the tangential force in Figure 3.18. Tangential force values during the backward stroke are multiplied by -1 to account for the opposite direction of movement. The average values are taken as the mean of the values of the points where velocity is within 12.5% of the maximum velocity. Instantaneous temperature is recorded during the cycle, and mean temperature during each cycle can be calculated.

Tilt angle of the sample around the x-axis is calculated from the slope of the linear regression of the normal load. The spring constant, from Section 3.1.2, is used to calculate the vertical displacement throughout the stroke. Finally, tangential force, normal force and coefficients of friction are adjusted with this tilt angle. The effect of adjustment is shown in 3.19. The effects are insignificant at the tilt angles of typical experiments.

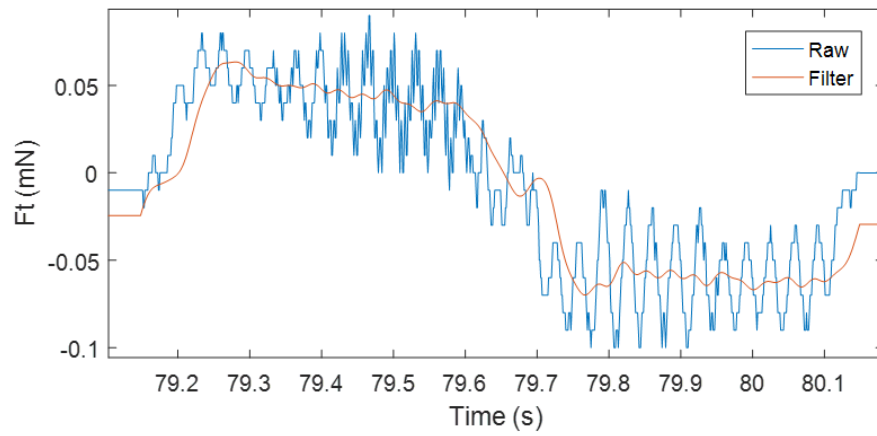


Figure 3.17 – Filtered signals of tangential load eliminating mechanical resonance effects. There is a 30 ms delay imposed in the filter method.

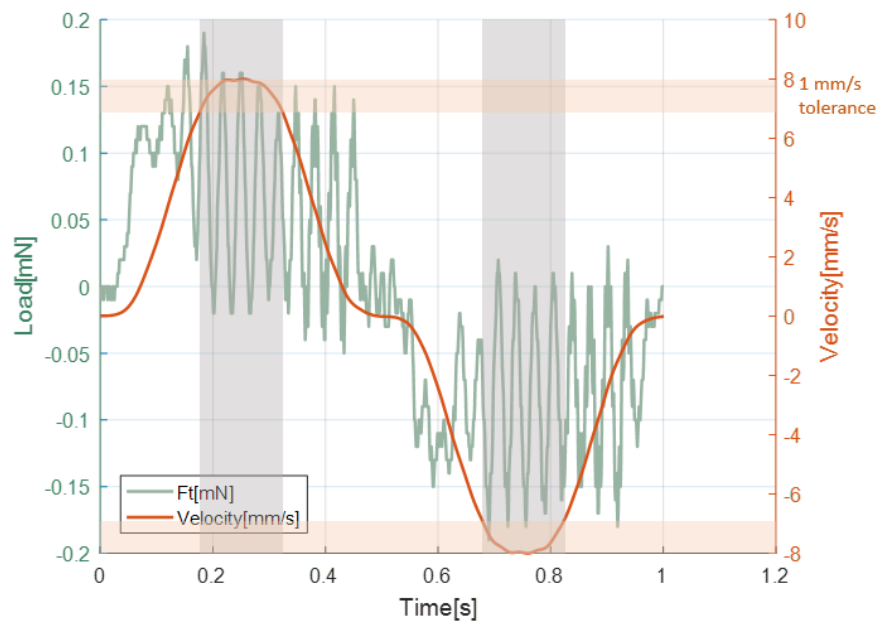


Figure 3.18 – Tangential force signals are averaged within the intersection of the maximum velocity zone (intersection of orange and gray regions).

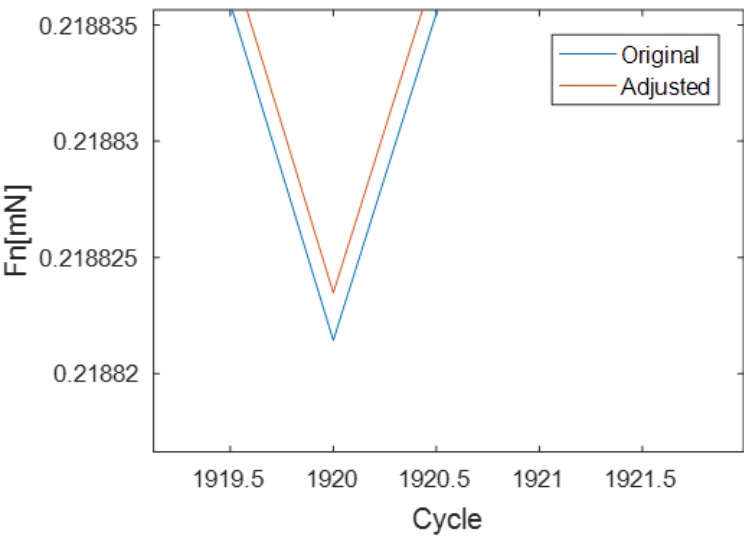


Figure 3.19 – Adjustment of tangential load for tilt angle. The effects are insignificant at the tilt angles of typical experiments.

3.2 Atomic Force Microscopy

Atomic force microscopy (AFM) is performed with a Park Systems NX10 atomic force microscope. Compared to CLSM, AFM allows greater precision of measurements with the drawback of greater measurement time. Profiles are made with NanoWorld PNP-TR Pyrex-nitride contact cantilevers with tip radius of less than 10 nm and tip height of 3.5 μm . A load of 6 nN is applied for contact mode scans at a scan frequency of 0.2 Hz.

Long profiles consist of stitched measurements, each of 30 μm in length. The profiles are stitched using a MATLAB script. Profiles to be stitched have a predefined overlap region of 10% of the profile length at the beginning and end of the scan. Measurement of profiles of up to 1 mm in length are possible. The profiles are stitched in the following steps:

1. The mean height value of the points in the overlap region are shifted so that it is equal to that of the adjacent scan.
2. The height of the points within the overlap region, are computed as the average of the two stitched scan.
3. The slope of the linear regression of the entire stitched profile is used to compute the angle of tilt.
4. The points are rotated around the origin to negate the tilt angle and then, are translated such that the minimum height value is zero.

3.3 Scanning Electron Microscopy

Scanning electron microscopy (SEM) is used for observation of sample surfaces and geometry. A Zeiss GeminiSEM 300 device is used, available at the Interdisciplinary Center for Electron Microscopy (CIME) of EPFL. The SEM is equipped with an in-lens secondary electron detector. Parameters used for imaging of the silicon dioxide samples are aperture size of 30 μm , acceleration voltage of 10 kV, and working distance of approximately 5 mm.

For high resolution imaging of topography, a sputtered gold coating of less than 10 nm in thickness is necessary to reduce distortion due to surface charging effects. With a conductive coating, a lower acceleration voltage of 3 kV may be used, allowing greater resolution. The gold coating has a 50 nm grain size which may be visible at high magnifications.

3.4 Focused Ion Beam

Focused Ion Beam (FIB) is used for milling cross-sections of the sample for observation. A Zeiss CrossBeam 540 device is used, available at CIME of EPFL. The device is equipped with a field emission SEM, a secondary electron secondary ion detector and gas injection systems for deposition of carbon. To perform the cross-section, a thin film of carbon of 500 nm was deposited on the surface. The carbon layer acts as a protective layer against unwanted etching

of the surface, allowing a smooth vertical cross-section at the area of interest. Milling of the sample is performed using gallium ion milling, with 100 nA beam current. The resulting cross-section is 10 μm in length perpendicular to the sliding direction. Imaging is done with a 2 kV electron beam at a working distance of 5 mm.

3.5 X-Ray Photoelectron Spectroscopy

X-Ray Photoelectron Spectroscopy (XPS) is used for characterization of surface chemical composition. Spatial resolution is approximately 100 μm^2 and depth sensitivity is approximately 10 nm. XPS provides atomic concentration with atomic percent resolution on the order of 0.1%. The X-ray monochromator uses Al K-alpha X-rays at 25.2 W. The primary elements of interest in this study are silicon, oxygen and carbon. The carbon 1s binding energy peak is calibrated to be 284.8 eV. For detection of silicon, the 2p peak is used, located between 103-104 eV binding energy. For detection of oxygen, the 1s peak is used located at approximately 533 eV binding energy.

3.6 Summary

A tribometer has been developed that allows for experiments with samples of well-defined geometries produced via microfabrication methods. The samples have been designed for a cylinder-on-flat geometry of contact with imposed alignment angle. Several features have been included that allow reproducible alignment, such as fixing the upper and lower bodies with breakable limbs, and cameras along two different axes. The tribometer functions at low load ranges of less than 10 mN matching watch conditions.

SEM allows observation of surfaces in the nanometer length scale under vacuum, combined with FIB cross-sections of the sample may also be observed. The topography may be characterized using AFM. Long stitched profiles are used to allow for characterization of roughness over a large range of length scales from nanometer to millimeter. XPS will be used for chemical characterization of surfaces. It will allow observation of any adsorbed substances with approximately 10 nm depth sensitivity.

4 Topography and Contact Mechanics

This chapter presents the physical characterization of the sample surface. Sample topography is characterized using AFM. With a well-defined topography, a method is developed for determining contact properties, such as contact area and contact pressure, as a function sample alignment, load and geometry. The simulation of the contact is verified with experiments on sputtered gold layers.

4.1 Topography

In order to investigate effects of varying surface topography, samples with four different surface topographies were designed. These topographies were fabricated with R5 geometry, and are named R5A, R5B, R5C and R5D. Each sample has respectively increasing roughness. Detailed AFM profiles of the samples were measured shown in Figure 4.1. The waviness forms regular ridges across the samples, and sliding occurs parallel to the ridges. The cylinder counterpiece is oriented with its length perpendicular to the ridges.

The characteristics of the ridges can be observed by performing 2D fast fourier transform (2D FFT) on the height map as shown for the R5A sample in Figure 4.2. The 2D FFT reveals a waviness with a periodicity of $0.67\text{ }\mu\text{m}$ with an amplitude of 1.3 nm . This pattern is a result of the etching process during fabrication. Adjusting the etching parameters allows control of the ridge height and sample roughness.

Cross-sectional profiles are shown in Figure 4.3. This characteristic waviness that is present in the different topographies have varying asperity radius, roughness heights and periodicities. Each of these parameters may impact the properties of the tribocontact such as contact area and contact pressure. Those properties in turn, will influence friction behavior. A method must be developed to quantitatively determine the effects each topography has on the tribocontact.

There is one sample with a significantly different surface topography. R5D was fabricated with large valleys of depth greater than $1\text{ }\mu\text{m}$. The cross-section is shown in Figure 4.4. Valleys have $10\text{ }\mu\text{m}$ periodicity and the peaks are flat, with a profile on the flat regions that is equivalent to that of R5C. R5D was designed in order to hypothetically further reduce surface area of the contact.

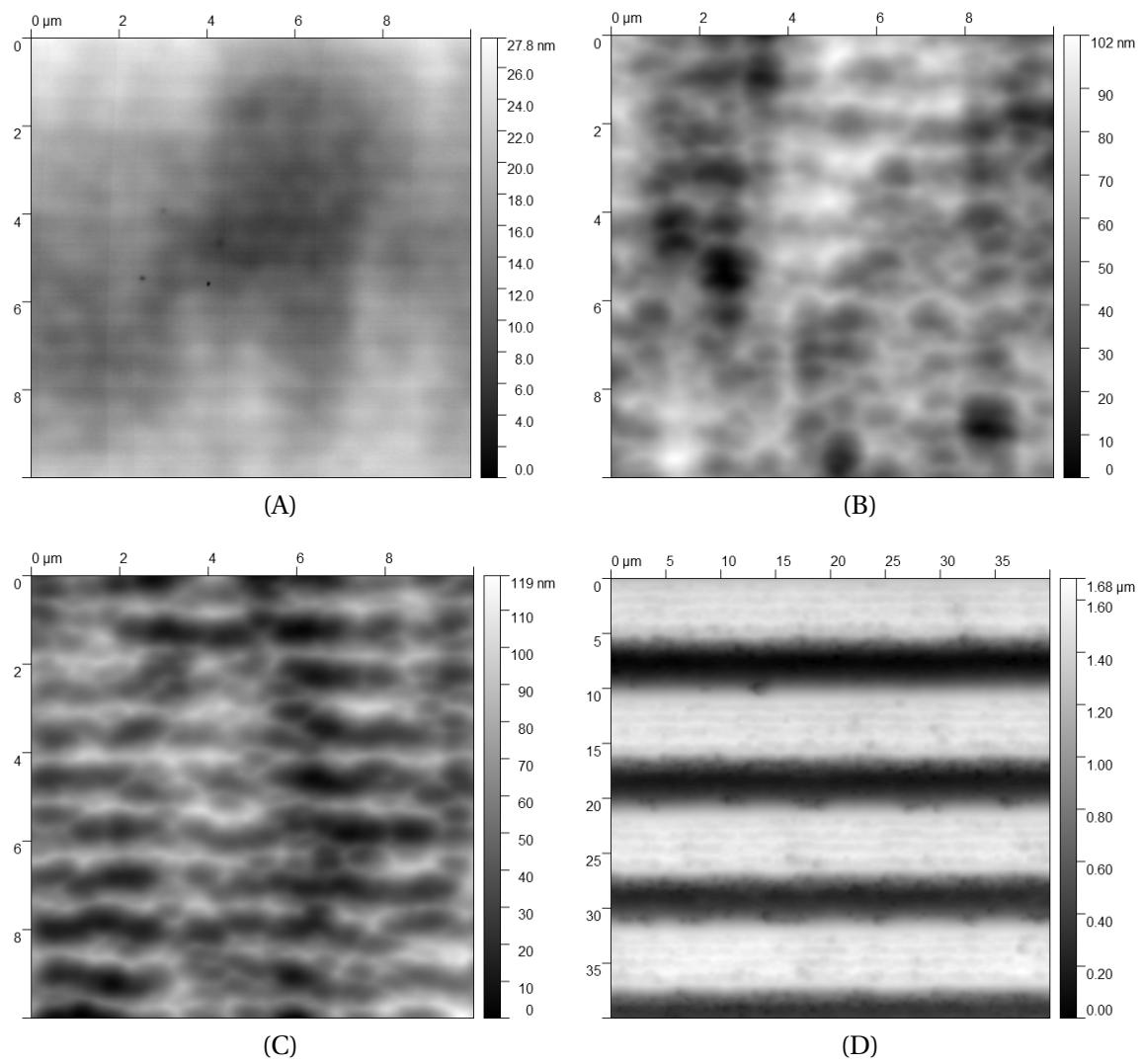


Figure 4.1 – AFM images of Samples A, B, C and D. Sliding occurs left to right with the length of the cylinder perpendicular to sliding direction.

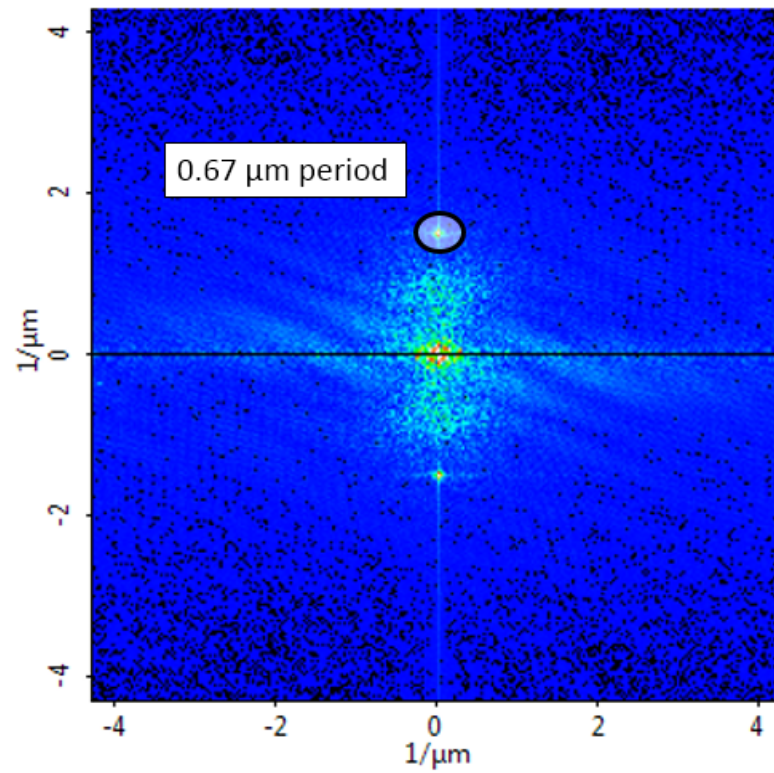


Figure 4.2 – Contact AFM measurements on R5A samples with scan area of $10 \times 10 \mu\text{m}$ with fast scan in the y direction. The 2D FFT (right) shows the periodicity to be $0.67 \mu\text{m}$.

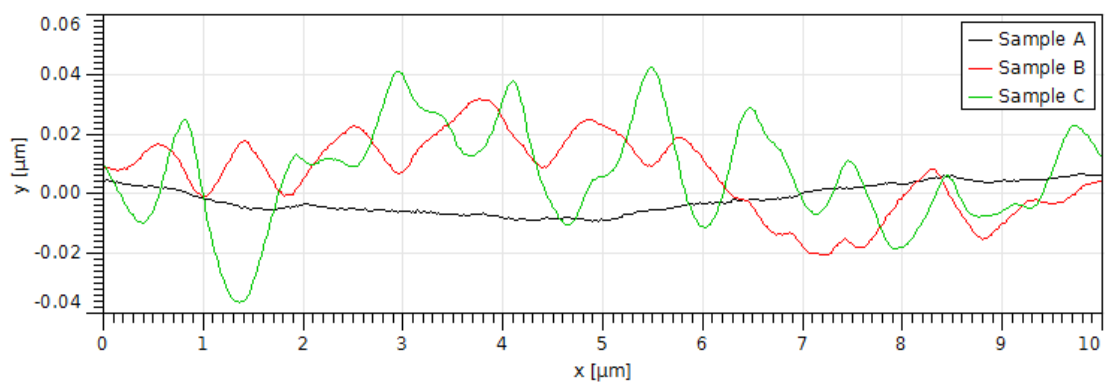


Figure 4.3 – Cross-sectional profiles of Sample R5A, R5B, and R5C in direction perpendicular to sliding.

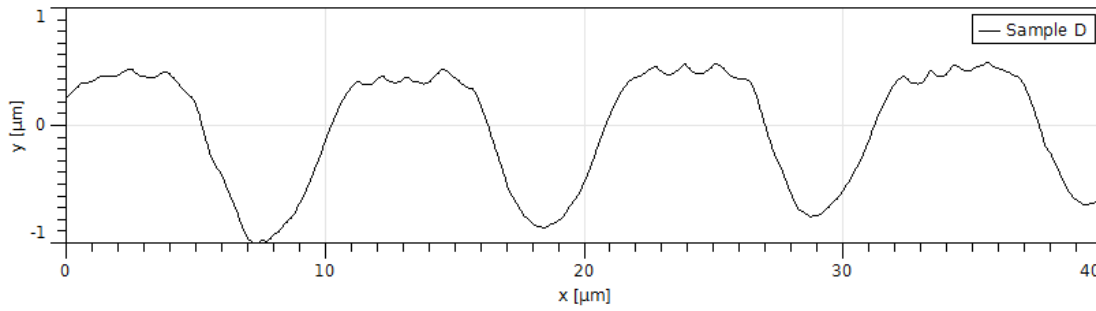


Figure 4.4 – Cross-sectional profile of AFM images of R5D in direction perpendicular to sliding.

4.2 Contact Simulation

In order to determine the effects of the various topographies on the tribocontact, a method is developed to simulate contact. The goal of the simulation is to determine contact areas and contact pressures experienced during sliding. The elastic deformation may be simulated using Hertzian models. The geometry of the contacting bodies corresponds to cylinder-on-flat. However, the solution to the Hertzian contact is complicated by two points: first is contact misalignment, shown in Figure 4.5, and second is surface roughness, shown in Figure 4.6. It is expected that the contact pressure is much larger than in an ideal cylinder-on-flat case and that the contact area is much smaller. Because the trivial solution for the ideal case cannot be applied, a boundary element simulation (BES) has been developed. For simplicity, the contact is taken as a smooth cylinder body on a rough flat surface, when in reality, both the cylinder and flat have surface roughness.

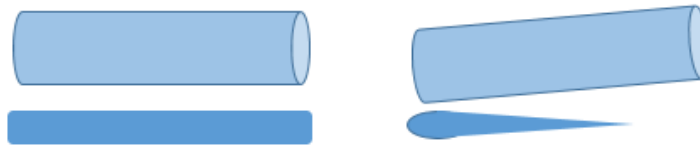


Figure 4.5 – Contact area of ideal cylinder on flat (left), and contact area of misaligned cylinder on flat (right), which requires numerical methods to solve

The BES is designed according to the Polonsky-Keer method [55], solved using the Bound-Constraint Conjugate Gradient method [56]. The material properties are that of silicon dioxide provided by the manufacturer, with elastic modulus of 70 GPa and Poisson's ratio of 0.17. A regular rectangular mesh is used with dimensions of 25 nm. The geometry of the contact is defined by a cylinder and torus, with radii designated as primary and secondary radii respectively, as shown in Figure 4.7. Primary radius and secondary radius is fixed based on SEM measurements shown previously in Table 3.1. Additionally, in order to simulate misalignment, an angle θ is imposed. The mesh that is generated is a distance mesh, where each point x and y have a value z corresponding to the distance between the two surfaces.

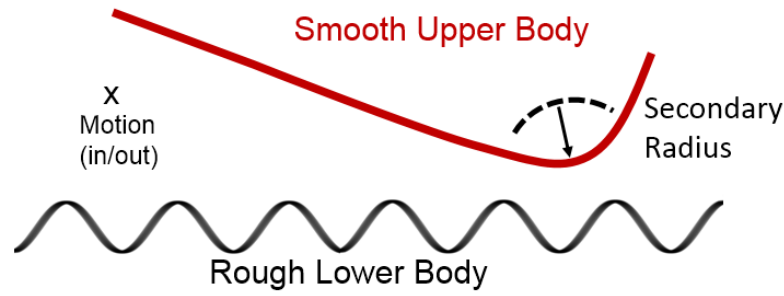


Figure 4.6 – Contact idealized as smooth cylinder upper body on rough flat surface

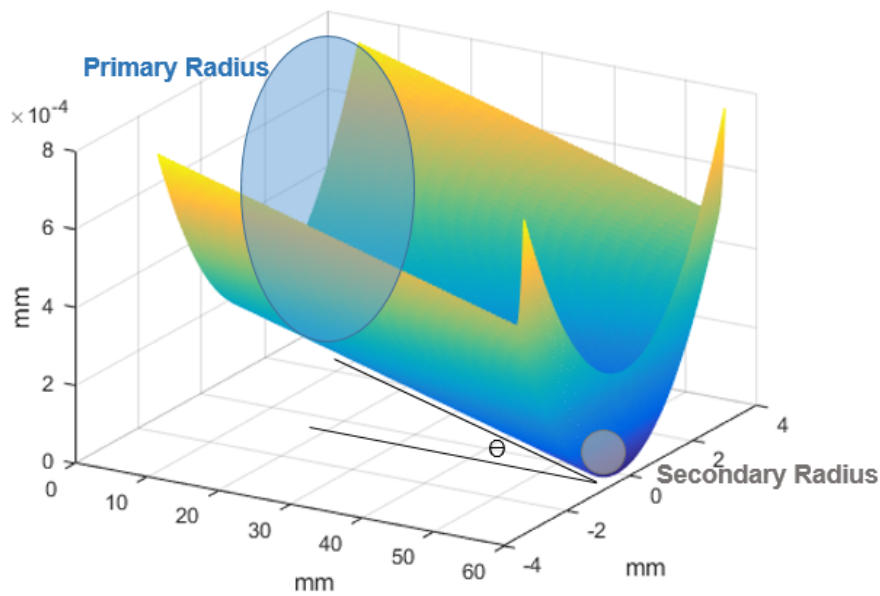


Figure 4.7 – Distance mesh of the contact of cylinder-torus geometry with imposed angle of 0.1° and radii corresponding to R10 sample.

In order to accurately determine characteristics of the contact under varying topography, real measured AFM profiles are also used. The AFM profiles are to be imposed on the distance mesh of the BES. The dimensions of the simulated area are up to $10\text{ }\mu\text{m}$ by $100\text{ }\mu\text{m}$. Because AFM data are available with scan dimensions of only $40\text{ }\mu\text{m}$ or less, the profiles must be extrapolated in order to extend the entire $100\text{ }\mu\text{m}$ distance of the simulation. AFM profiles are naively stitched together, as shown in Figure 4.8 for topography B. Stitched AFM profiles have been corrected for inclination and have had height values shifted such that the minimum is equal to zero. Profiles are also interpolated in order to match the sampling rate with the mesh dimensions.

The profile is subtracted from the distance mesh, yielding a mesh as shown in Figure 4.9. The ridges and valleys are in the direction parallel to the direction of sliding and perpendicular

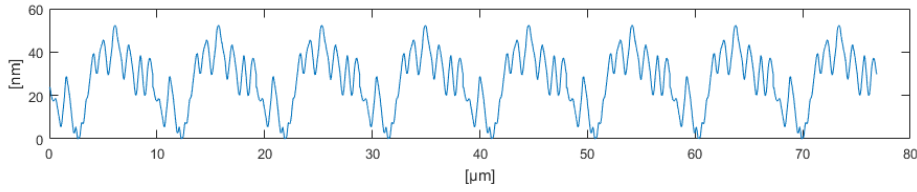


Figure 4.8 – An AFM profile of R5B perpendicular to sliding direction, repetitively stitched for application with numerical simulation.

to the length of the cylinder counterpiece. It is assumed that the cylindrical counterpiece is perfectly smooth.

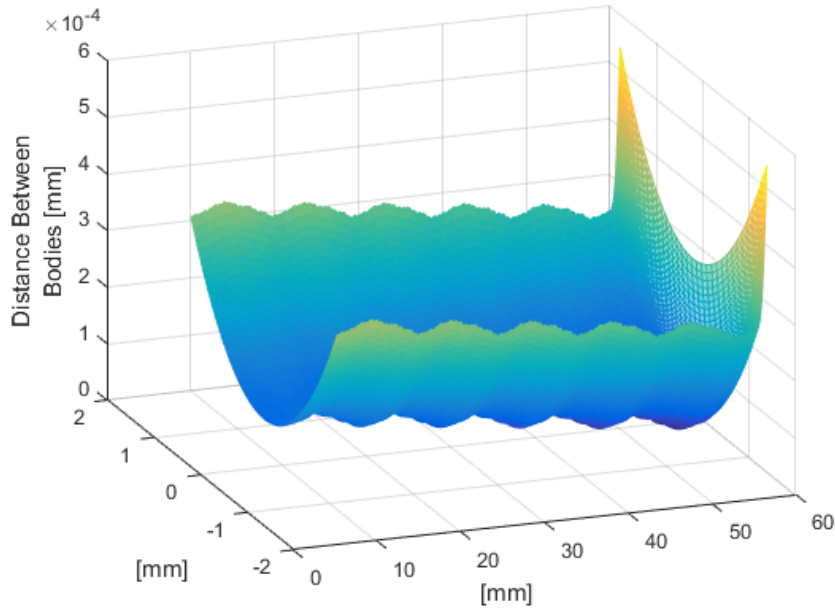


Figure 4.9 – Distance mesh of topography A with AFM profile superimposed and assuming perfectly smooth upper counterpiece. The cylindrical has a primary radius of 5 μm , a secondary edge radius of 2 μm , and a misalignment of 0.1°.

Solving the BES allows extraction of the contact area and distribution of contact pressures. For the R10A sample with 0.4° tilt angle under varying load, the results are shown in Figure 4.10. Under loads of up to 2 mN for example, it is expected that there are maximum contact pressures of between 1 and 2 GPa. Contact area, however, may vary greatly from 0.3 to 4 μm^2 being highly dependent on both angle and pressure. A series of simulations may be performed by varying load and misalignment angle. The results of contact area and maximum pressure may be fit with a least-squares power law fit in 3 dimensions order to estimate the contact conditions given the experimental parameters. This allows quick estimation of contact properties without performing the potentially time intensive simulation. The contact area, A in m^2 , and maximum pressures, P_{max} in Pa, are estimated by the equations as follows in

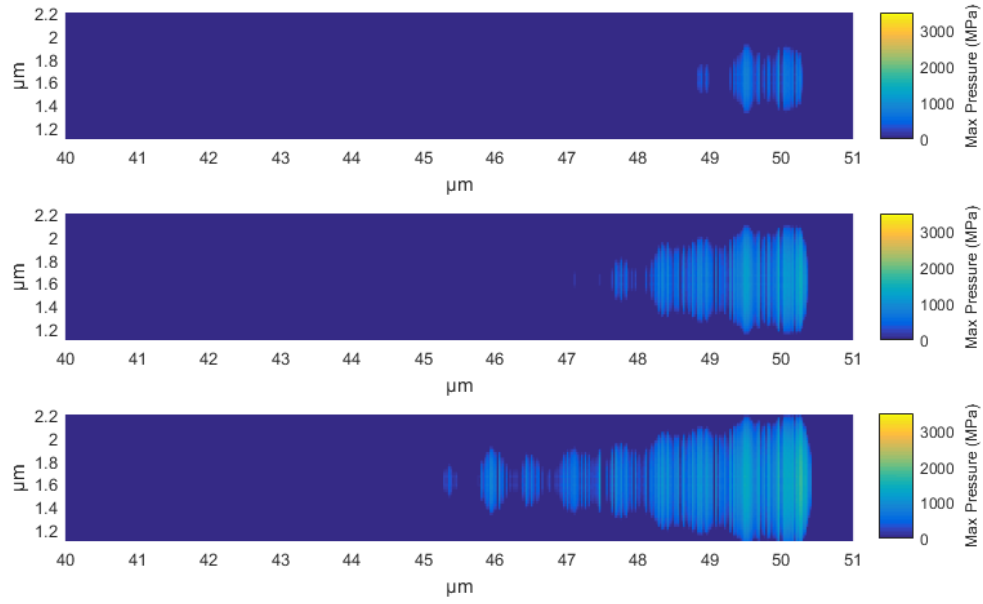


Figure 4.10 – The contact of cylinder-torus geometry representing R10A samples at 0.4° tilt. Contact area is the area where pressure is greater than zero.

terms of log base 10:

$$\log(A) = \beta_1 \log(F_N) + \beta_2 \log(\theta) + \beta_3 \quad (4.1)$$

$$\log(P_{\max}) = \eta_1 \log(F_N) + \eta_2 \log(\theta) + \eta_3 \quad (4.2)$$

where normal load, F_N , is in N and angle, θ , is in degrees. The values of the power law constants, for base 10 logarithm, for each of the samples and topographies are summarized in Table 4.1. These simulated values of contact area and maximum pressure may be used as parameters in a quantitative mechanistic model.

Table 4.1 – Constants for power law relationship of A [m^2] and P_{\max} [Pa] as functions of F_N [N] and θ [$^\circ$].

Sample	β_1	β_2	β_3	η_1	η_2	η_3
R5A	0.832	-0.228	-9.451	0.195	0.184	9.900
R5B	0.898	-0.164	-9.350	0.166	0.122	9.882
R5C	0.847	-0.162	-9.735	0.166	0.120	10.145
R5D	0.902	-0.148	-9.782	0.236	0.104	10.455
R10A	0.882	-0.079	-9.058	0.182	0.074	9.677
R20A	0.874	-0.056	-9.025	0.083	0.066	9.306

4.3 Experimental Validation

The simulation results are validated by comparing experimental wear trace dimensions with those extracted from the simulation. Under the low load conditions applied there is no significant wear. Due to lack of visible wear traces, an experimental method was devised to allow observation of the contact dimensions involving scratch tests on gold coated samples. The scratch test consists of 10 oscillations on samples with a 3 nm sputter-coated layer of gold. Angle is imposed from camera images, and load is fixed at the beginning of the test. Results for varying loads with R10 samples and a tilt angle of approximately 0.4° are shown in Figures 4.11, 4.12, 4.13 and 4.14. Contact width is measured based on contrast of SEM images. It is from the extremities of the region of deformed gold perpendicular to sliding direction as shown by the dashed red line in the figures. At low loads the effects of surface topography can be clearly observed. The periodicity of the marks correspond directly to the periodicity of the surface roughness measured by AFM.

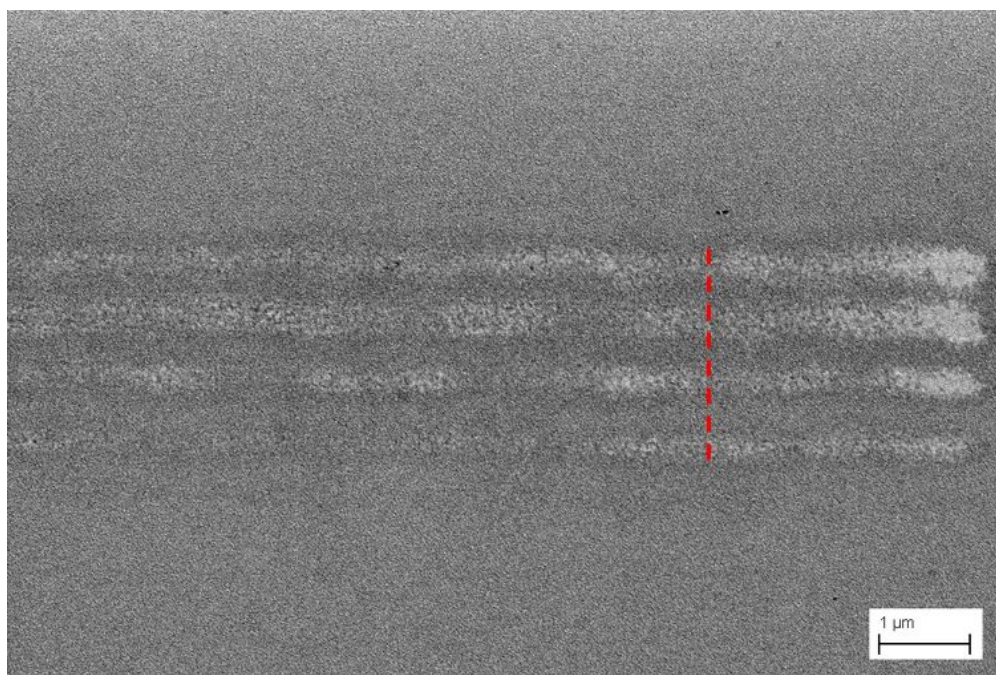


Figure 4.11 – Scratch test results of 0.2 mN load for R10 samples on 3 nm gold layer after 10 oscillations with 0.4° angle. The brighter regions indicate plastically deformed gold. Dark regions correspond to exposed silicon dioxide surface. The dashed line represents the measurement of contact width.

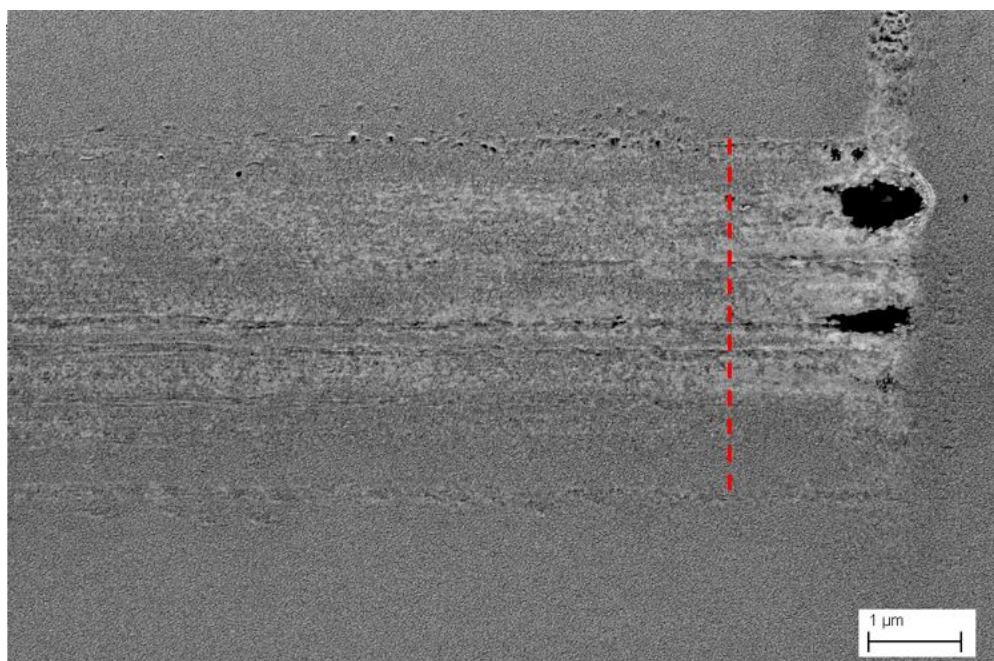


Figure 4.12 – Scratch test results of 0.5 mN load for R10 samples on 3 nm gold layer after 10 oscillations with 0.4° angle. The brighter regions indicate plastically deformed gold. Dark regions correspond to exposed silicon dioxide surface. The dashed line represents the measurement of contact width.

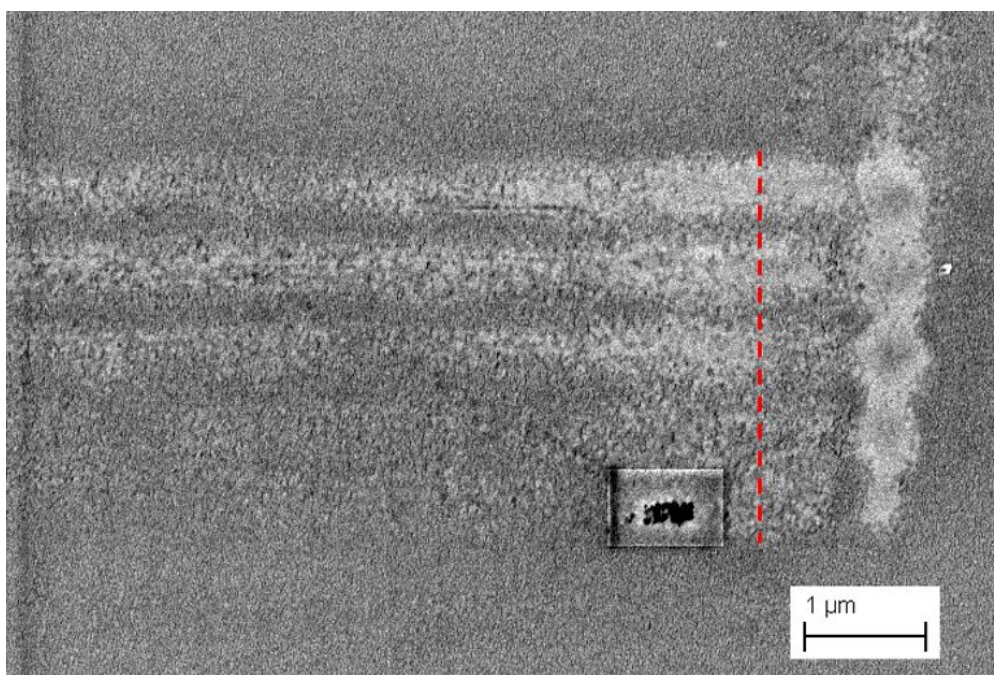


Figure 4.13 – Scratch test results of 1 mN load for R10 samples on 3 nm gold layer after 10 oscillations with 0.4° angle. The brighter regions indicate plastically deformed gold. Dark regions correspond to exposed silicon dioxide surface. The dashed line represents the measurement of contact width.

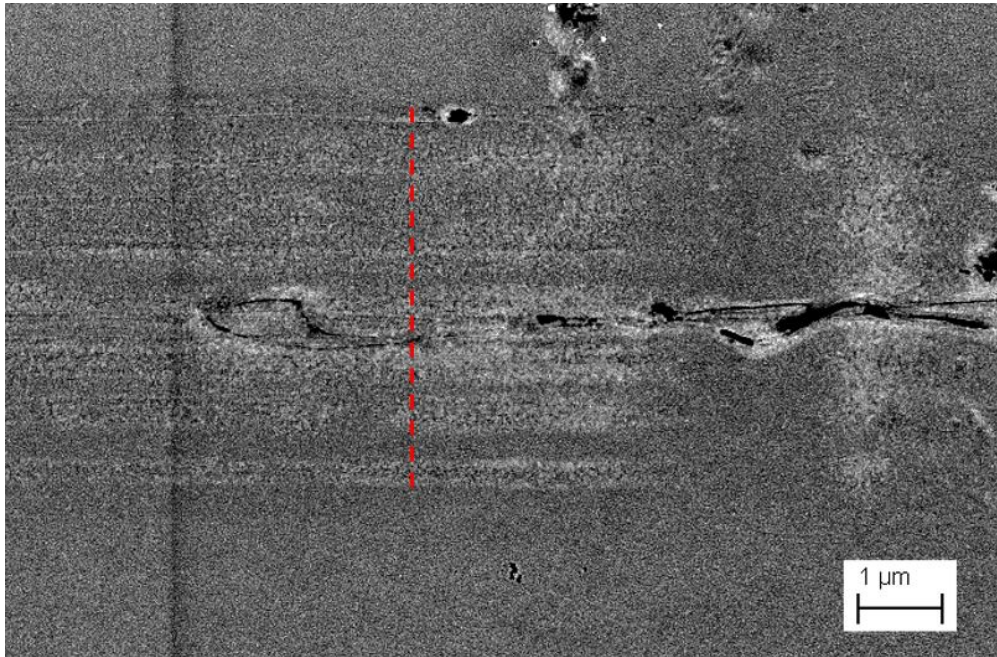


Figure 4.14 – Scratch test results of 2 mN load for R10 samples on 3 nm gold layer after 10 oscillations with 0.4° angle. The brighter regions indicate plastically deformed gold. Dark regions correspond to exposed silicon dioxide surface. The dashed line represents the measurement of contact width.

Simulated contact widths from the BES are compared with experimental contact widths, shown in Figure 4.15. Experimental width may be underestimated at high loads due to limited sensitivity of SEM imaging. Plastic deformation of gold at the extremities of the contact area may not be visible. This effect is greater at high loads where the low contact pressure region is larger. Nevertheless, the predicted contact widths are within 1 μm error.

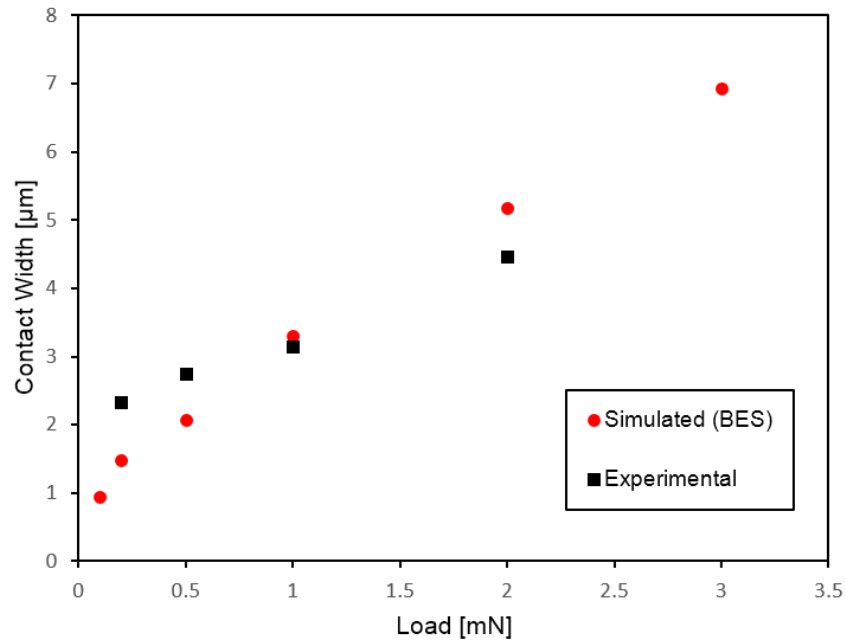


Figure 4.15 – Comparing simulated contact widths from the BES with experimental contact widths from gold scratches using R10A samples at 0.4° tilt.

4.4 Summary

A method has been developed for simulating elastic deformation of the contacts. This allows for extraction of contact pressures and contact dimensions, given a normal load and geometry. The contact of interest is of misaligned cylinder-on-flat configuration. The geometry is defined by the radii of the cylinder, the misalignment angle of the cylinder and the topography of the surfaces. Topography has been determined by AFM profiles for a variety of samples. Width of the simulated contact has been shown to correspond with widths of wear traces observed experimentally.

5 Experimental Results

Given the experimental system developed and the detailed characterization of the tribological contact of interest, a series of experiments has been designed. The aim is to identify the various factors affecting friction and friction evolution. The effects of cylinder geometry, load, chemical surface treatments, and topography are investigated. The experiments allow observation of the friction evolution over several thousand cycles is observed and of any changes to the surface. Changes to surface topography are to be characterized quantitatively by AFM, and qualitatively by FIB and SEM.

5.1 Effects of Contact Radius

The effects of primary contact radius are investigated using a series of identical experiments. An increase in contact radius is expected to correspond to an increased contact area and decreased contact pressure according to Equations 4.1 and 4.2. The R20A sample with the largest primary radius, and the R5A sample with the smallest primary radius were used for this series of experiments.

The normal load used is 1 mN. Maximum sliding velocity is 8 mm/s, with a sliding length of 2 mm. Cycle frequency is 1 Hz. The experiments are run for at least 5000 cycles. The friction evolution is observed by taking the average friction coefficient during each cycle. Plotted in Figure 5.1 are the average frictions with a data point at 80 cycle intervals for both R5A (blue) and R20A (green) samples. Seven identical experiments are performed with R5A samples and four identical experiments are performed with R20A samples.

The results show that in all experiments, a gradually increasing friction is observed. Friction results for R5A samples have a total dispersion of friction coefficient μ of approximately 0.3 throughout the duration of the experiment. R20A samples show a dispersion of 0.5-0.8 throughout the duration of the experiment. There is an inverse dependence of contact radius on friction. Over the 5000 cycles, R5A samples generally show an increase in friction from 0.21 to 0.25, while R20A samples generally show an increase from approximately 0.22 to 0.33. The initial friction shows less of a dependency on contact radius compared to the friction at the end of the experiment. The influence of the size of the contact is more apparent as R5A and R20A friction diverges from each other with increasing number of sliding cycles.

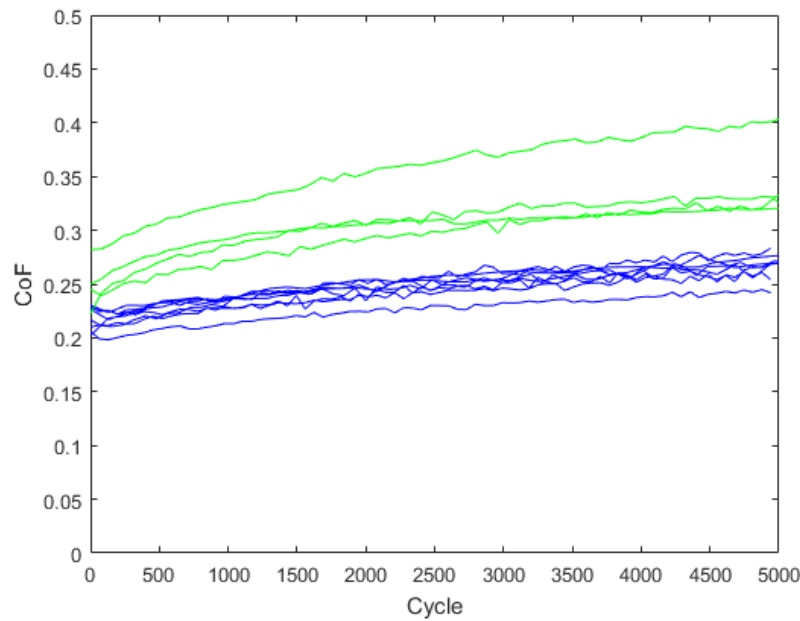


Figure 5.1 – Coefficient of friction evolution over 10000 cycles at 1 Hz, 8 mm/s, 1 mN, 2 mm sliding length for R5A (Blue) and R20A (Green) samples

To begin with, wear behavior and surface deformation is investigated as a possible cause of the gradual increase in friction. In these experiments, wear traces and wear particles are not observed under SEM imaging. Figure 5.2 shows the surface of a R5A sample before a tribological experiment, and Figure 5.3 shows the surface of a sample after the tribological experiment where the wear trace should be located. Sliding Images were taken at different positions on the sample surface. No features of material deformation or removal are present. No sign of a wear trace is observed. SEM imaging of the R5A cylinder body after the experiment is shown in Figure 5.4 and also shows no sign of wear. The red circle indicates the region of contact, no distortion in the cylinder geometry is observed.

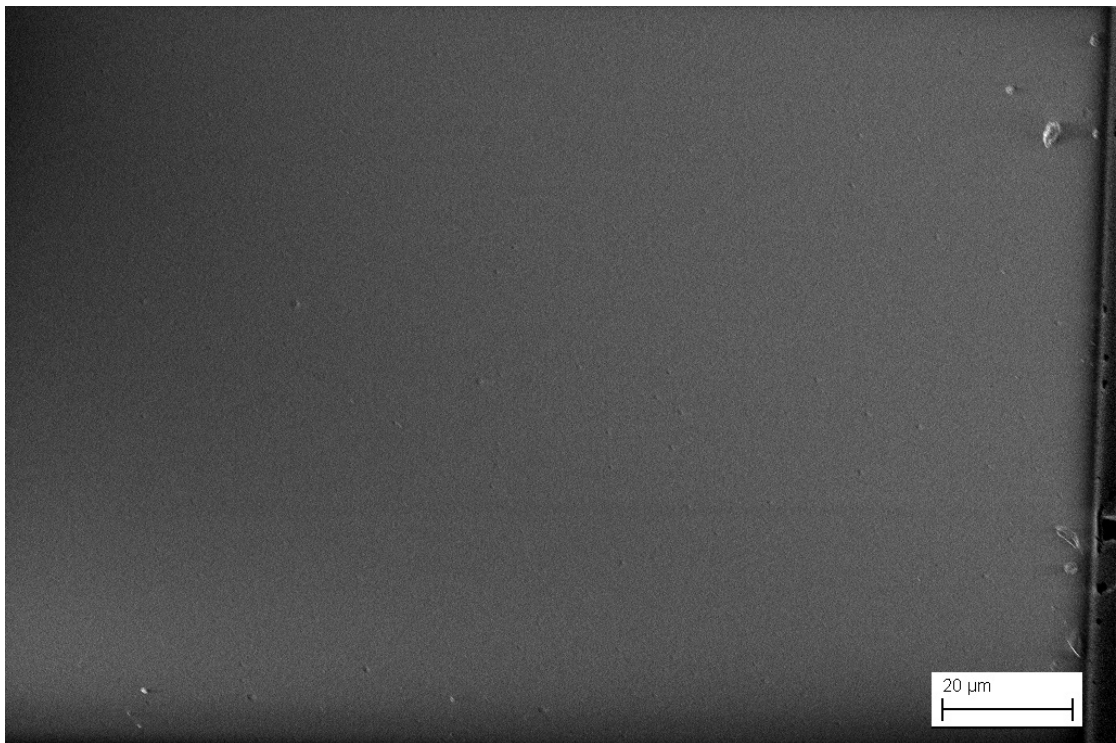


Figure 5.2 – Surface of R5A flat surface before tribological experiment

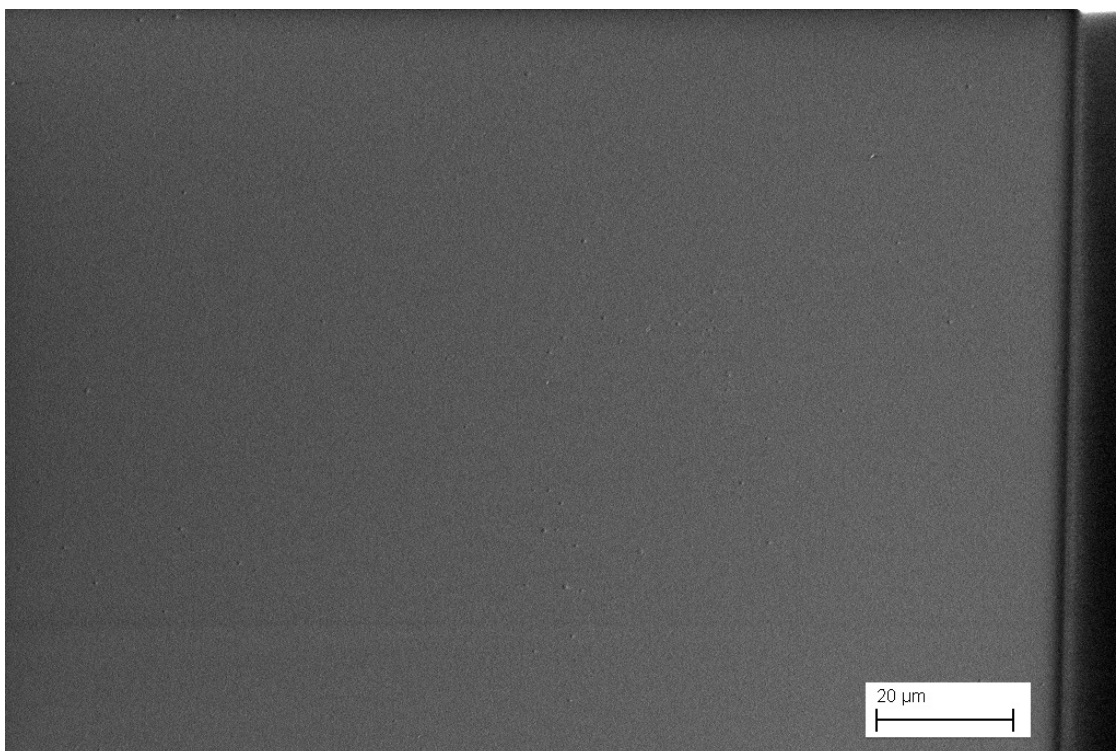


Figure 5.3 – Surface of R5A flat surface after 10000 cycles at 1 Hz, 8 mm/s, 1 mN, 2 mm sliding length.

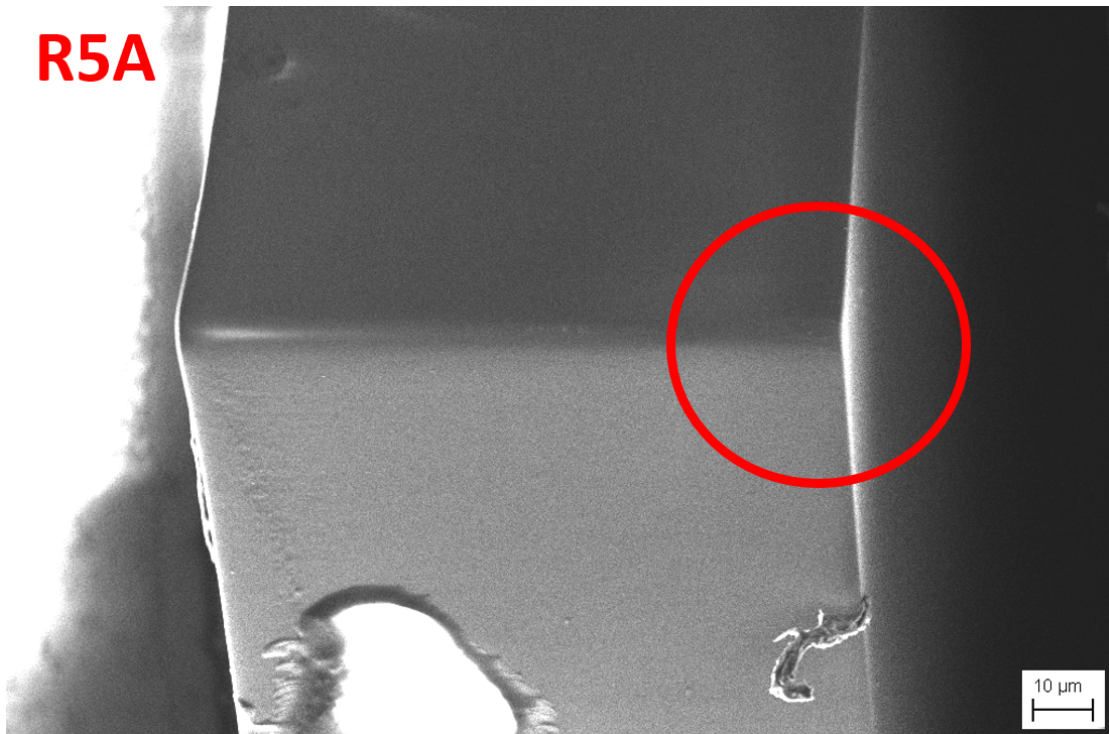


Figure 5.4 – Surface of R5A cylinder after 10000 cycles at 1 Hz, 8 mm/s, 1 mN, 2 mm sliding length. Circled is the region of contact.

In order to observe subsurface signs of deformation, such as cracks, FIB was used to mill cross-sections perpendicular to the sliding path. The cross-sections were then observed by SEM, as shown in Figure 5.5. A high magnification image shown in Figure 5.6 shows the surface topography of the sample. No evidence of deformation is observed beneath the surface by SEM imaging.

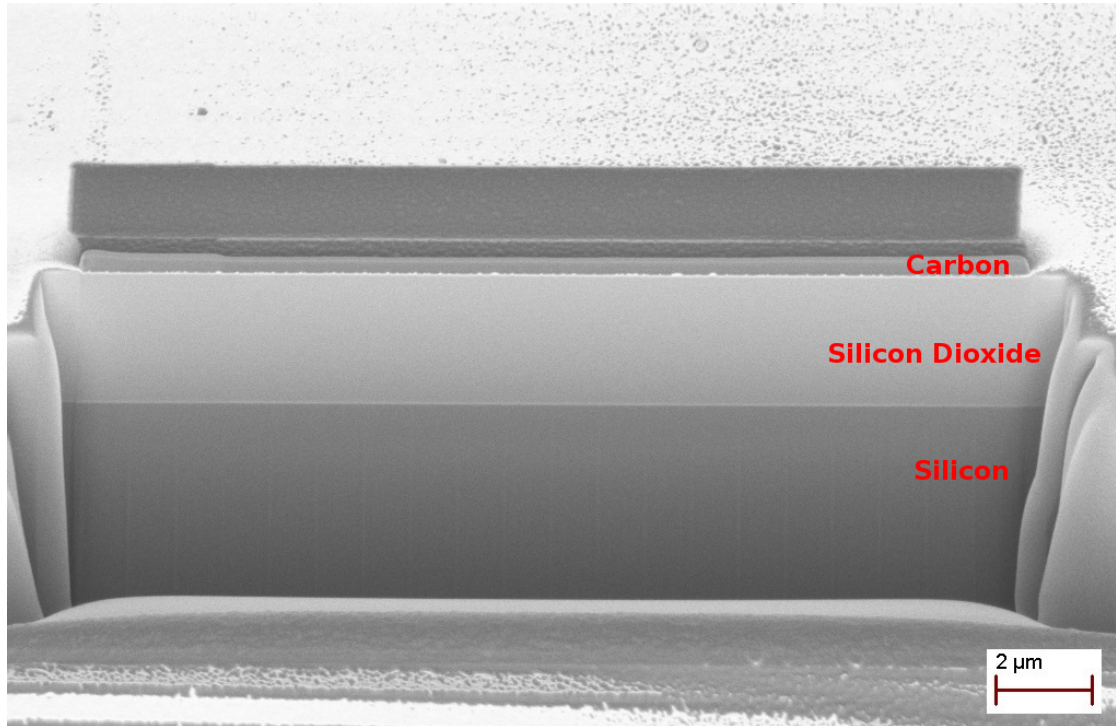


Figure 5.5 – FIB cross-section of R5A sample after 10000 cycles at 1 Hz, 8 mm/s, 1 mN, 2 mm sliding length.

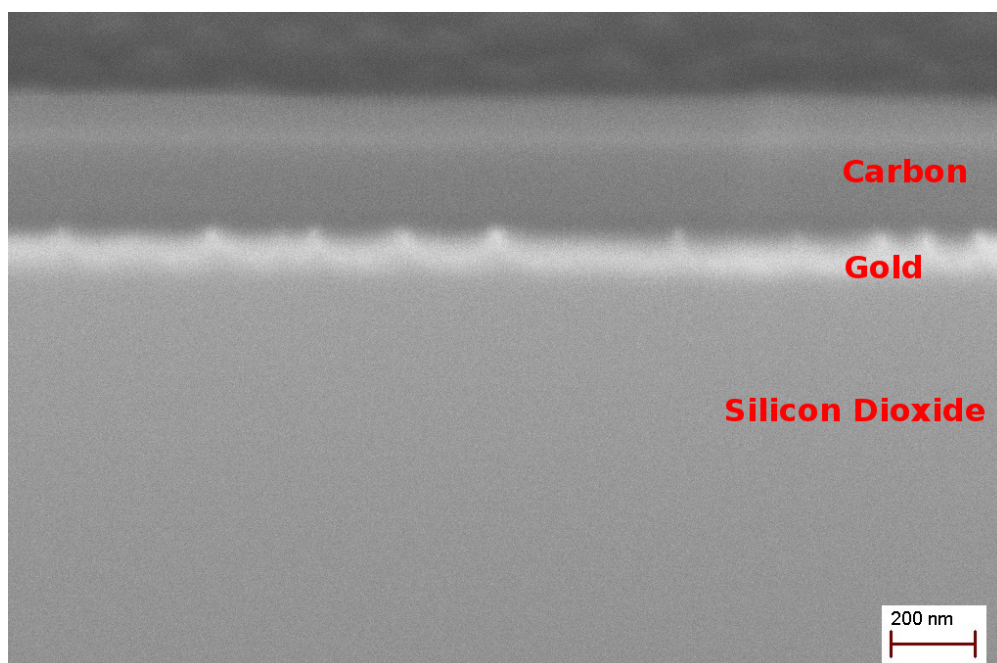


Figure 5.6 – High magnification extract of previous cross-section of R5A sample transverse the wear track

Topographic changes are expected if there is plastic deformation of the surface or material removal due to wear. After the experiments at 1 mN over 2 mm distance at 8 mm/s with R5A samples, the surface topography is characterized. No topographical change is observed under optical microscopy or laser confocal scanning microscopy. As a higher resolution technique, the topography of the surface is measured using AFM, as described by the protocols. Profiles transverse of the sliding track are measured. Three profiles crossing the sliding track are compared to two profiles outside the sliding area altogether, all shown in Figure 5.7. By comparing values of roughness at various length scales, it is possible to evaluate if the surface has deformed [57]. If there is significant differences in roughness at a certain length scale after a tribological experiment, surface deformation has occurred and the presence of wear can be confirmed.

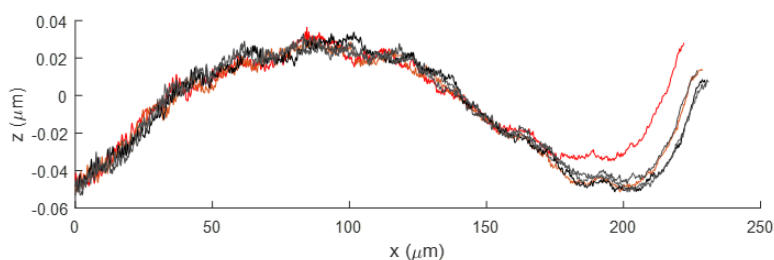


Figure 5.7 – AFM profiles in the direction perpendicular to the sliding direction, two profiles crossing the sliding track (red) and three profiles outside of the sliding track (black)

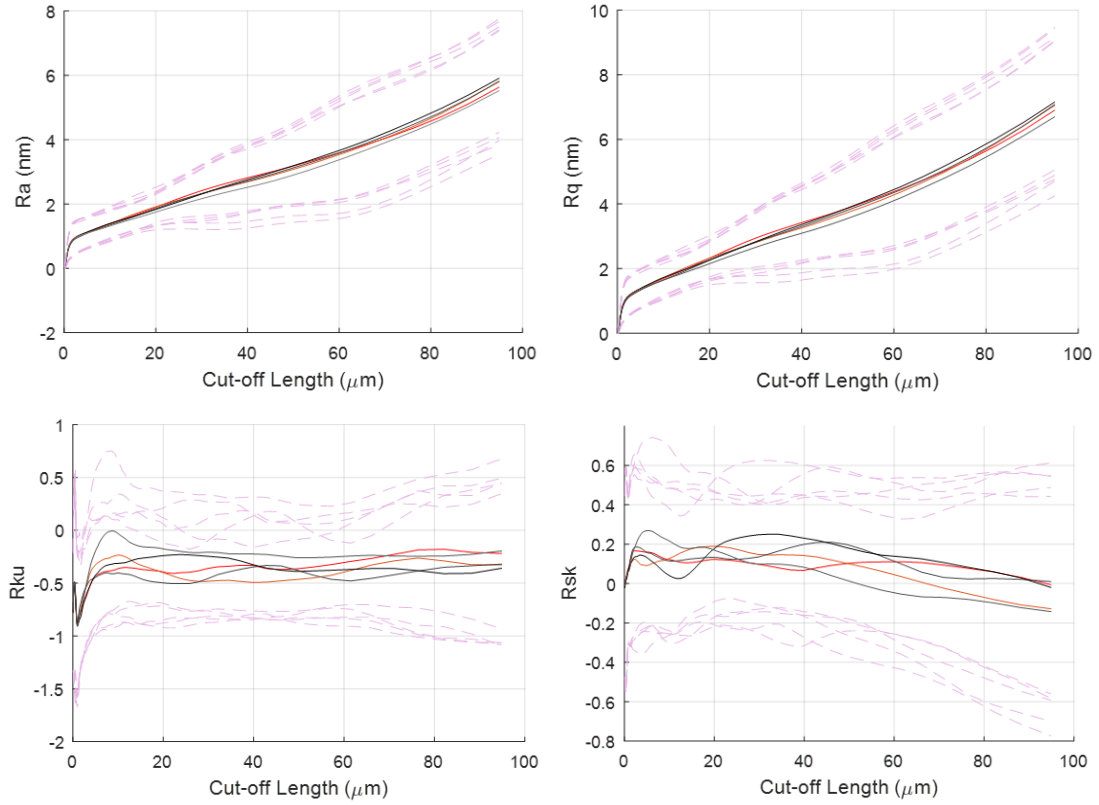


Figure 5.8 – Varying length-scale roughness of the AFM profiles. R_a , R_q , R_{sk} and R_{ku} . Two profiles crossing the sliding track (red) and three profiles outside of the sliding track (black). Limits of standard deviation of the roughness values over the profile length are in pink.

The results in Figure 5.8 show measurements of roughness parameters R_a , R_q , R_{sk} and R_{ku} , representing the arithmetic mean roughness, root-mean-square roughness, skewness and kurtosis respectively. It is unknown the length scales at which modifications of the surface due to friction will appear, therefore, values at varying length scales is determined by varying the cut-off length of roughness calculation. At each point in the AFM profile, the roughness values within a cut-off length of that point is calculated. The mean and standard deviations of the values at all AFM data point are calculated for each cut-off length. The mean and standard deviations are then plotted as a function of cut-off length. The results show that there are no significant changes in topography at any scale comparing before and after the tribological experiment, both in mean values and in standard deviations. From both SEM imaging and roughness analysis with AFM profiles, no plastic deformation or material removal due to wear of the surfaces are observed. The increasing friction observed experimentally therefore cannot be attributed to surface deformation.

5.2 Effects of Load

Load dependence was next observed. As with increasing contact radius, increasing load would lead to an expected increase in contact area. There is, however, significant increase in contact pressure. These experiments used the R5A samples with the same parameters as used previously except for normal load, for which 1.5 mN, 2 mN, 4 mN and 5 mN were also applied. Two repetitions at 4 mN load were performed to observe variance. The results are shown in Figure 5.9.

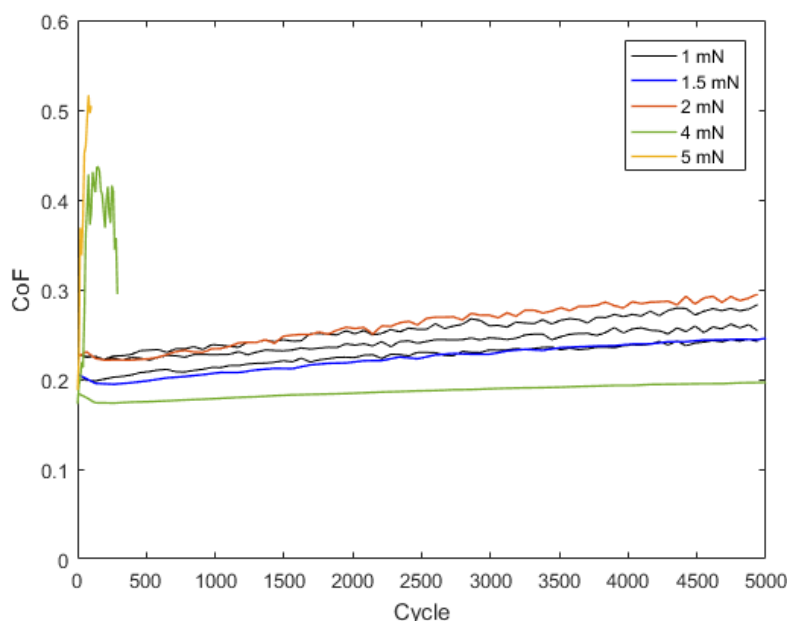


Figure 5.9 – Coefficient of friction evolution of R5A samples over 1000 cycles at 1 Hz, 8 mm/s, 2 mm sliding length at varying loads. Experiments at 4 mN and 5 mN are terminated prematurely due to sensor overload

Friction evolution at high loads was highly irreproducible. For some samples, at higher loads of 4 and 5 mN, a rapid rise in friction coefficient is observed in the first 100 cycles. In these samples, the experiments were terminated early due to sensor overload. At lower loads of 1.5 mN and 2 mN, a gradual rise in friction coefficient typical of the results at 1 mN is observed. There is no clear dependence of friction on normal load. There is a second experiment at 4 mN that had significantly lower friction.

The two samples at 4 mN showed particularly varying friction evolution. One sample showed rapidly increasing friction coefficient until experiment termination, and another sample showed consistently low friction coefficients. SEM images of the samples in the two 4 mN experiments were observed. Figures 5.11 and 5.12 show the flat surface and cylinder counterpiece, respectively, of the low friction experiment. Figures 5.13 and 5.14 show the flat surface and cylinder counterpiece, respectively, of the high friction experiment. There is a clear

difference in contact area, shown by the width of the wear traces on the flat surfaces. Wear on the cylinder counterpiece may explain this discrepancy. In the low friction experiment, particles had accumulated on the cylinder counterpiece, which reduced the contact area to the vicinity of the accumulation. In the high friction experiment, wear debris accumulated on the flat counterpiece, some of which may be seen ejected at the ends of the sliding path. The cylinder counterpiece has a flattened region, showing a polishing type of wear. This allowed for a large contact area. The results show how the random behavior of particles may cause extreme irreproducibility of friction evolution.

The relationship between contact width and friction coefficient is plotted in Figure 5.10. The friction coefficient taken is the maximum friction coefficient observed in the 5000 cycles of the experiment. In the 4 mN experiments, where wear was observed, the contact width was taken to be the width of the wear trace in SEM images of the flat surface. Experiments with lower load, between 1 and 2 mN, have no wear trace, so contact widths are approximated using BES. A misalignment angle of 0.1° tilt was used as determined by camera imaging. Horizontal error bars show the range of contact width for angles $\pm 0.05^\circ$ to account for imprecision of the angle measurement. For the 1 mN experiment, vertical error bars show the range of friction observed over the three repetitions. The simulated change in contact width due to increasing load from 1 to 2 mN is within the error limits caused by precision of the angle measurement. Nevertheless, the 4 mN results suggest a dependence of friction coefficient evolution on contact width, where greater contact width indicates greater contact area. The initial friction coefficients however, have no clear dependence on contact area.

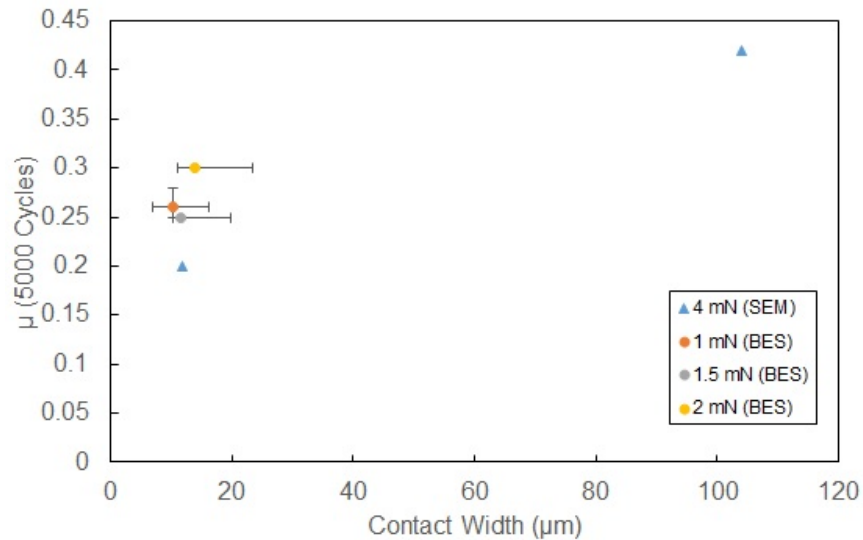


Figure 5.10 – Friction shown as a function of contact width. Triangle markers represent contact widths extracted from SEM images for 4 mN experiments. Circle markers represent contact widths extracted from BES for 1 mN to 2 mN experiments. Horizontal error bars represent the effect of $\pm 0.05^\circ$ tilt, and vertical error bars represent the range of friction observed over multiple experiments.

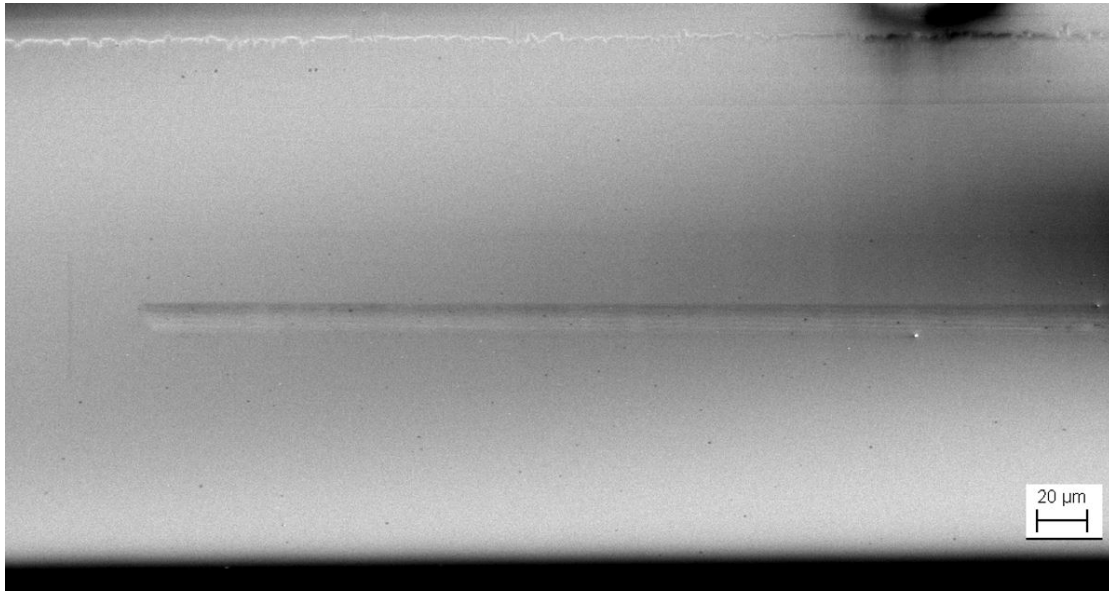


Figure 5.11 – SEM image of the low friction wear trace after 5000 cycles at 1 Hz, 8 mm/s, 2 mm sliding length and 4 mN load.

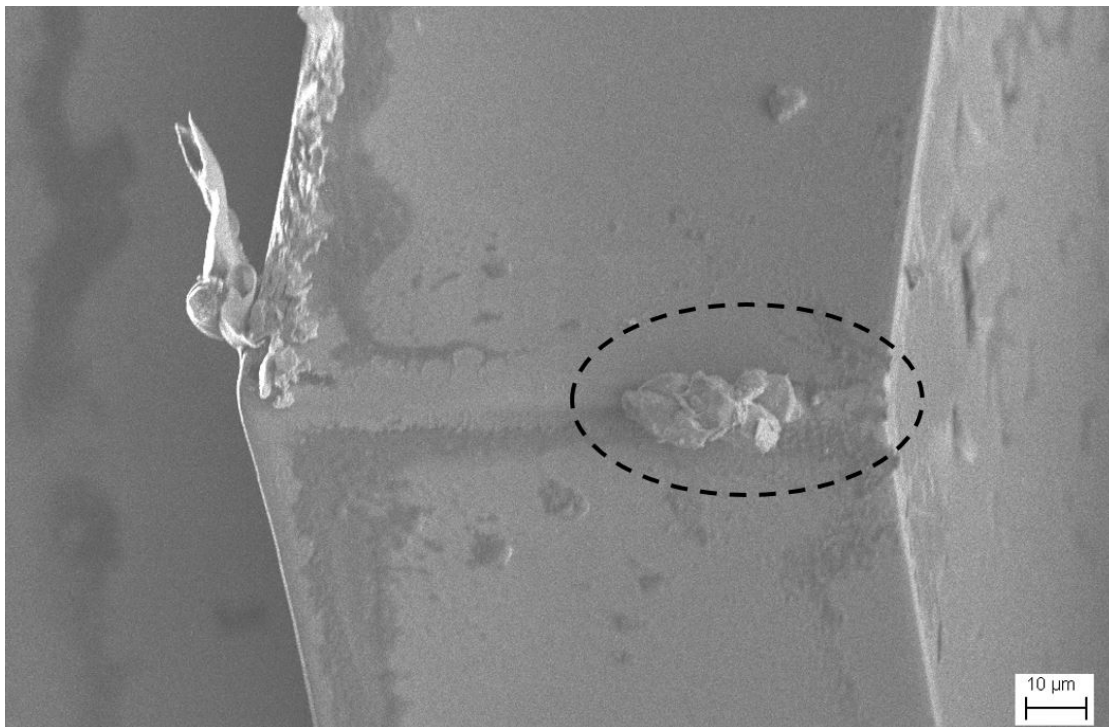


Figure 5.12 – SEM image of the cylinder counterpiece in the low friction experiment after 5000 cycles at 1 Hz, 8 mm/s, 2 mm sliding length and 4 mN load. Circled is the region where the cylinder is in contact with the flat.

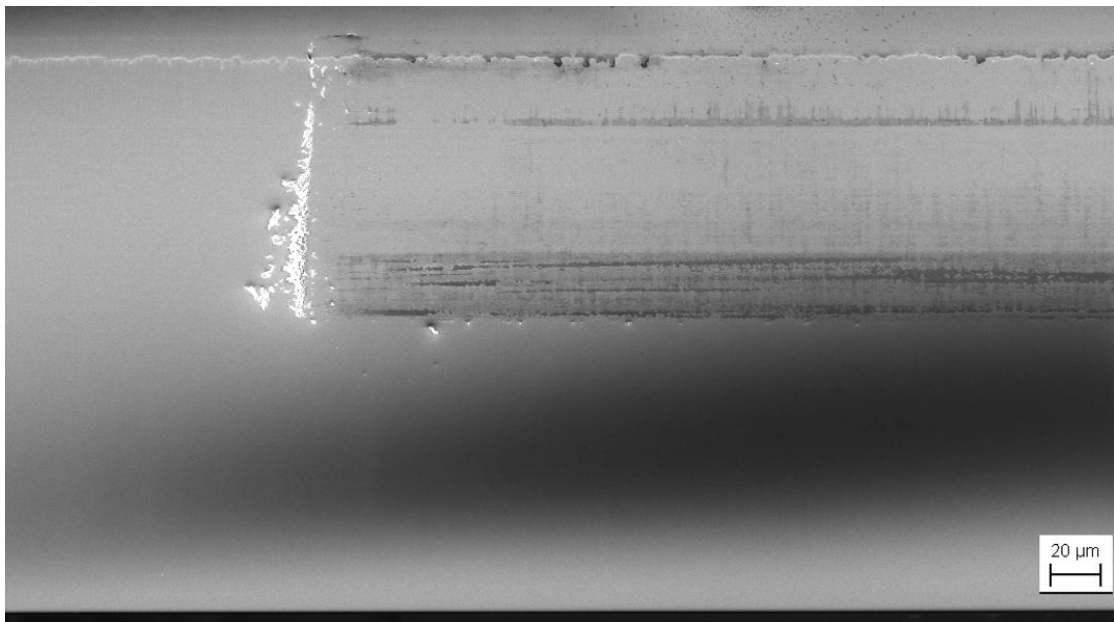


Figure 5.13 – SEM image of the high friction wear trace after 300 cycles at 1 Hz, 8 mm/s, 2 mm sliding length and 4 mN load.

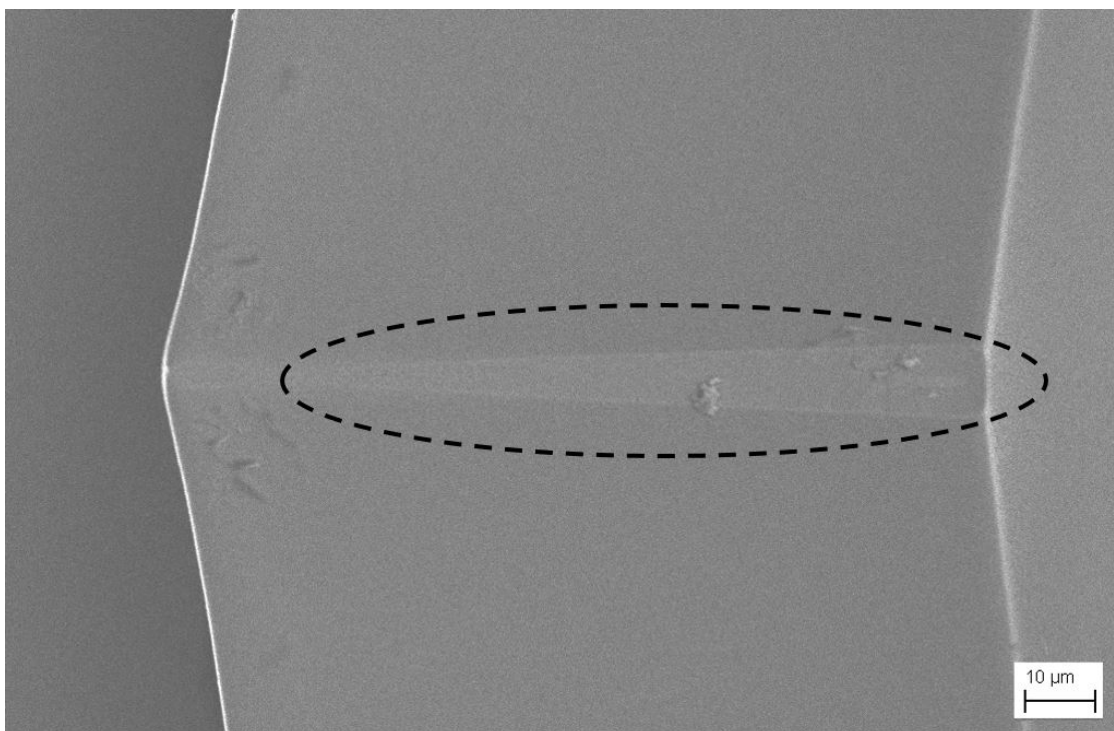


Figure 5.14 – SEM image of the cylinder counterpiece in the high friction experiment after 300 cycles at 1 Hz, 8 mm/s, 2 mm sliding length and 4 mN load. Circled is the region where the cylinder is in contact with the flat.

Wear behavior for all the samples are observed by imaging of the cylinder counterpieces. As seen previously, a polishing type wear may result in a flattening of the curvature of the cylinder body. This is seen in SEM images of the cylinder counterpieces after 5000 cycles of sliding shown in Figure 5.15. The region of contact is shown circled in red. The results at 4 mN, which have been shown previously, and at 5 mN show a visible flattened region. Wear debris is also observed at the ends of the sliding trace in flat surfaces shown in Figure 5.16. No wear is observed for experiments at 2 mN or below, suggesting there exists a load or contact pressure threshold above which significant wear occurs.

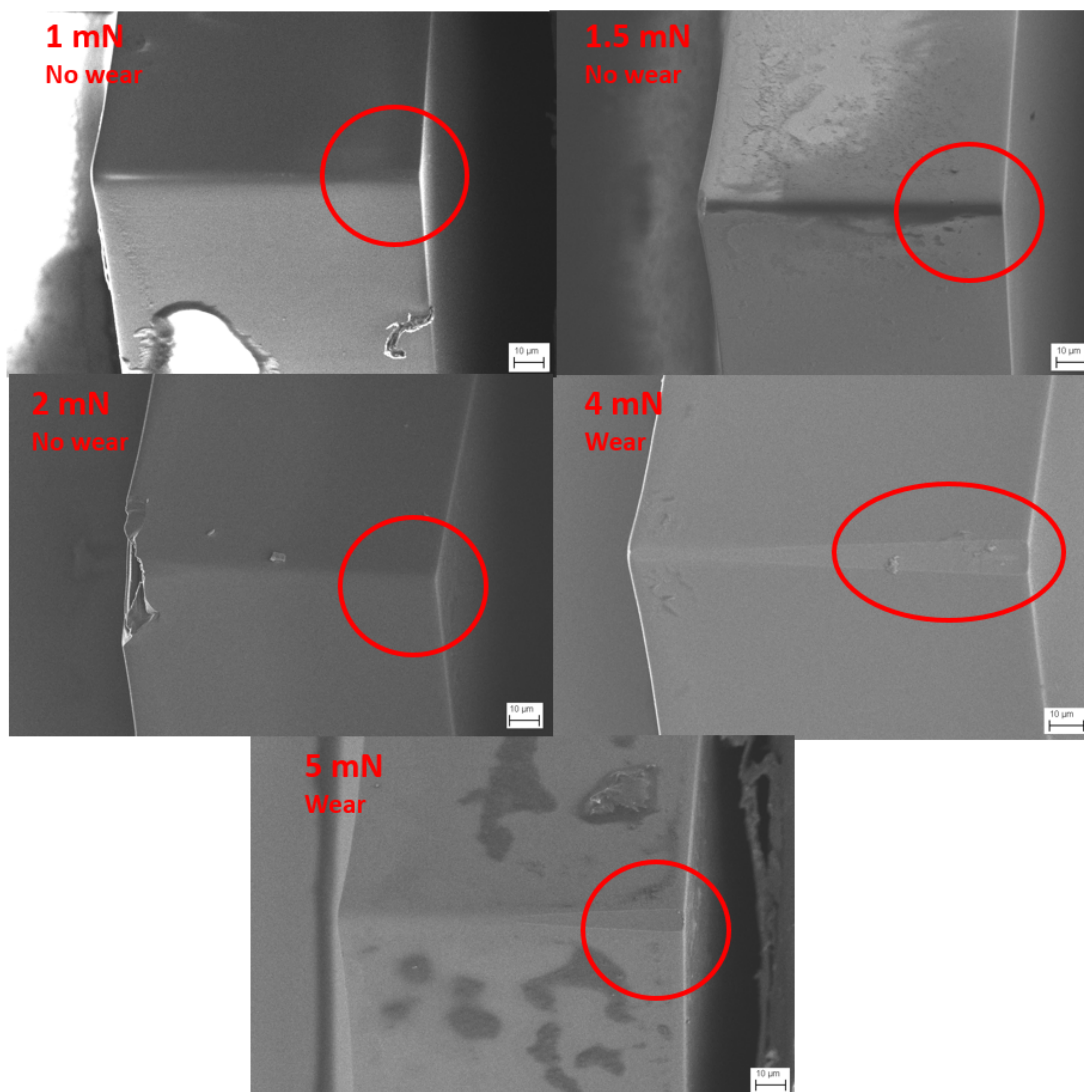


Figure 5.15 – SEM images of cylinder body of samples R5A after 5000 cycle tribological experiments at varying loads from 1 mN to 5 mN. Red circles indicate region of contact.

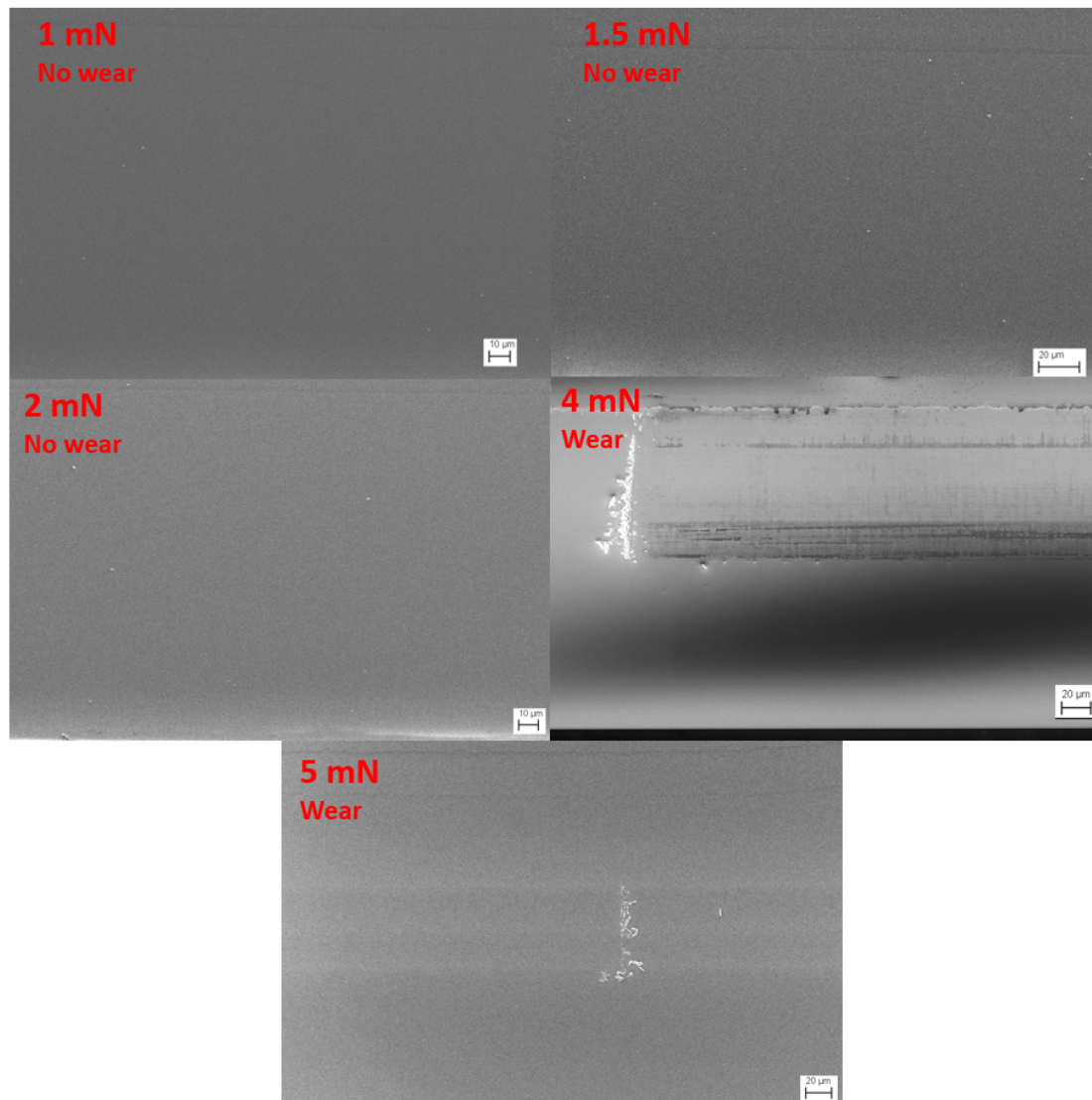


Figure 5.16 – SEM images of flat surface of samples R5A after 5000 cycle tribological experiments at varying loads from 1 mN to 5 mN.

5.3 Interrupted Experiments

To observe the characteristic gradual increase in friction over time, longer duration experiments of up to 50000 cycles were performed with R5A samples. Experimental parameters are the same as in the previous experiments. Two types of experiments were performed: continuous and interrupted. Continuous experiments operated nonstop over its entire duration. Interrupted experiments had pauses of fixed duration after 5000, 10000, 13000, 18000, 23000 and 28000 cycles. Results are shown in Figure 5.17, where the dashed lines indicate interruptions in sliding. The interruptions last for a duration of 15 s, during which time, the counterpieces remain stationary in contact under 1 mN load. Two general features of friction evolution are observed. First is that there is a continuous cumulative increase in the friction coefficient. Second is that there is a recovery in the friction coefficient after an interruption.

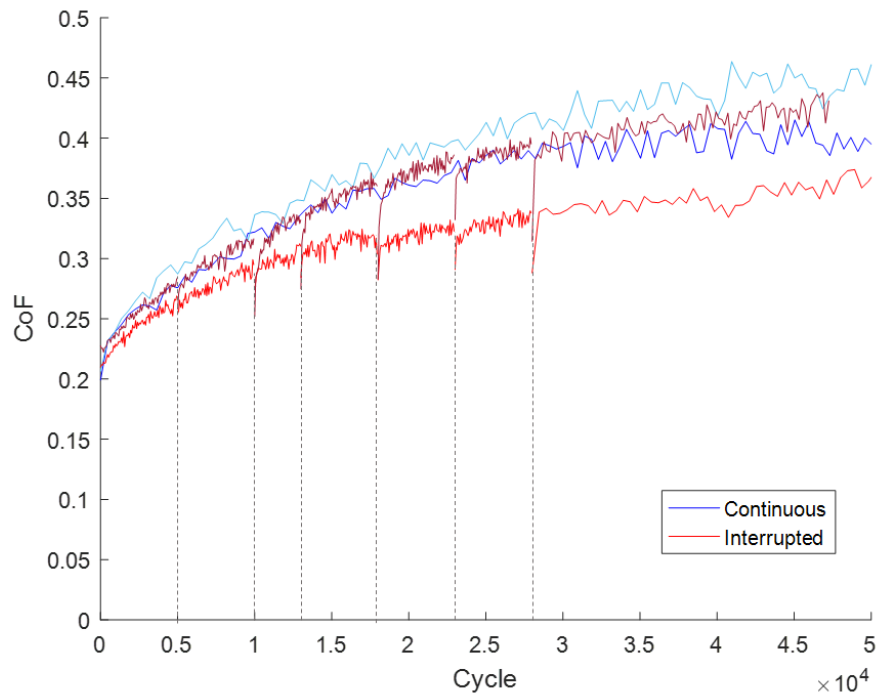


Figure 5.17 – Coefficient of friction evolution of R5A samples over 50000 cycles at 1 Hz, 8 mm/s, 1 mN, 2 mm sliding length for two experiments with no interruptions (blue) and two experiments with 15 s interruptions (red). Interruptions are indicated by the dashed lines.

The time dependence of the recovery of friction is also observed by performing an experiment with longer interruption time, as shown in Figure 5.18. These results suggest two main types mechanisms of friction: one that causes a permanent cumulative change in the material, and one that causes a recoverable change in the material during the interruption. The shape of the curve resembles those observed in literature [12]. Adsorption or desorption of surface species may cause the recoverable behavior observed. No evidence of wear is observed in any experiment by SEM imaging of the cylinder counterpiece.

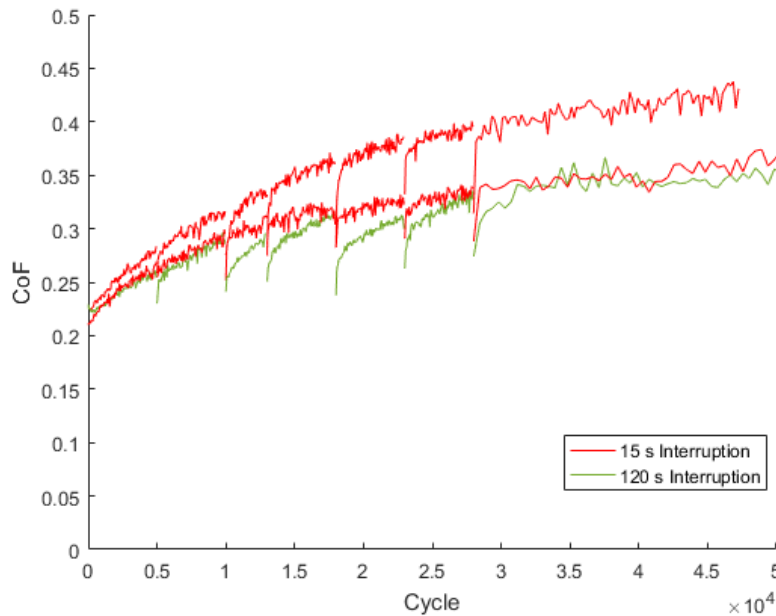


Figure 5.18 – Coefficient of friction evolution of R5A samples over 50000 cycles at 1 Hz, 8 mm/s, 1 mN, 2 mm sliding length for two experiments with 15 s interruptions (red) and one experiment with 2 min interruptions (green).

5.4 Surface Pretreatment

Given the possible effects of surface contamination, the effects of different surface treatments were studied. Different treatments typical used in industry for sample cleaning were selected for the investigation. Five cases were studied: samples as-delivered after fabrication, water rinse, isopropyl alcohol (IPA) rinse, benzene rinse, and trichlorododecylsilane (TCDS) coating. Petroleum-benzene 60-95 is used, which is a mixture of C6 and C7 hydrocarbons typically used in industry as a cleaning fluid. The procedure for water, IPA and benzene treatments consist of soaking the sample in a beaker of the respective solution for 30 minutes while in an ultrasonic bath. Samples were then fixed to the tribometer and left in the enclosure overnight for the glue to cure before commencing the experiments. TCDS samples had been cleaned in Piranha solution for 20 min and subsequently rinsed in a water bath. The TCDS coating was performed by soaking for 15 min in a dodecane solution of 2% TCDS.

XPS analyses were performed to determine surface composition of the samples prior to the experiment. The results are shown in Figure 5.19, where all spectra have been normalized such that their maximum intensities are equal to 1. Carbon 1s, oxygen 1s and silicon 2p peaks are used to quantify atomic composition. Samples vary in the intensities of the carbon peak, oxygen peak and silicon peak, as shown in Figures 5.20, 5.21 and 5.22 respectively. The relative atomic concentrations of carbon, oxygen and silicon are shown in Table 5.1. Increases in carbon are attributed to organic contaminant adsorption from the environment, or from the cleaning solution. Water rinsing may introduce small amounts of carbon contamination. IPA

and benzine rinsing leaves some residual molecules adsorbed to the surface. As, expected benzine and TCDS treatments yield the greatest carbon concentrations.

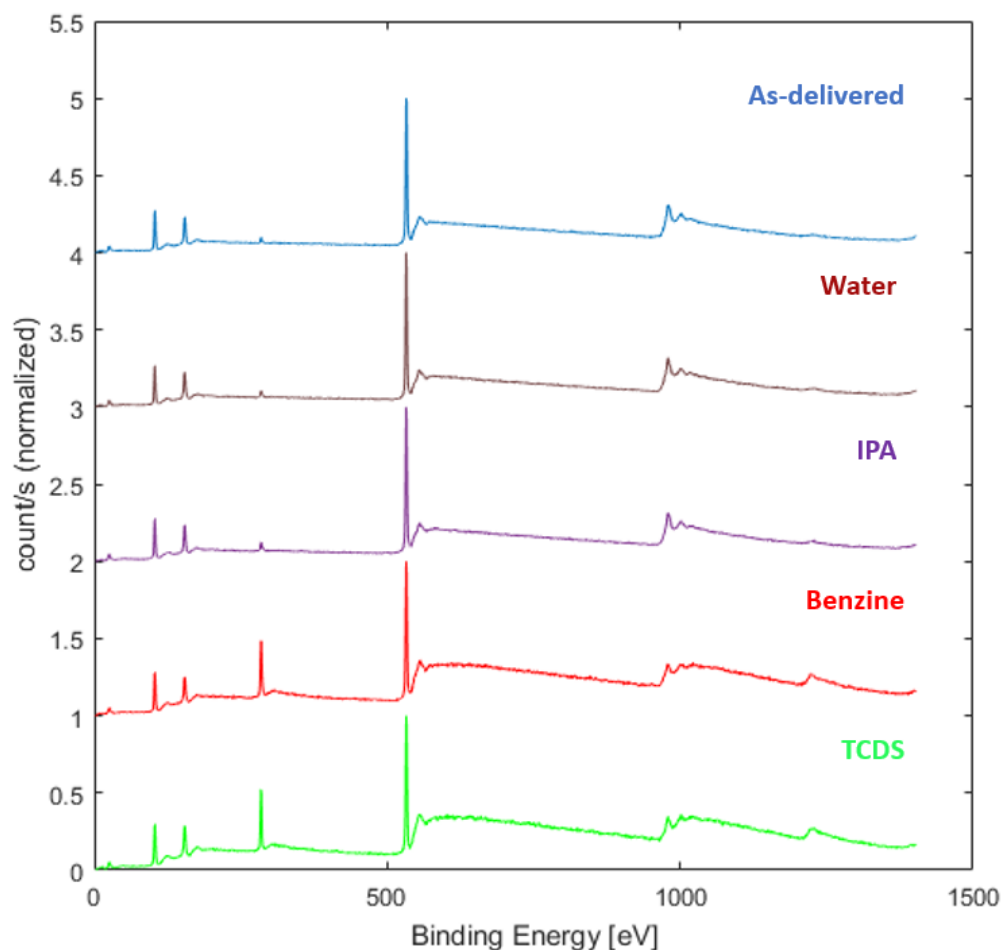
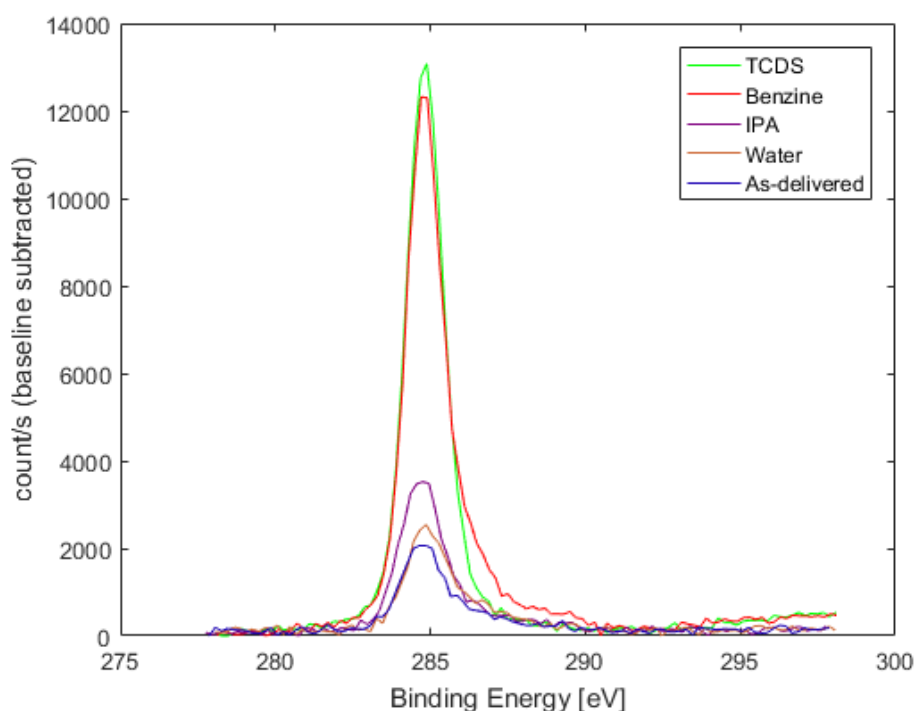


Figure 5.19 – Photoemission spectrum from XPS analyses

Using the R5A samples, the interrupted tribological experiments were performed after treatment. Interruption time was 15 s at 5000, 10000, 13000, 18000, 23000 and 28000 cycles. Friction evolutions are shown in Figure 5.23, with identical experimental parameters as previous tests. No wear is observed by SEM imaging of the cylinder counterpiece in all experiments. Over 70000 cycles, there is a low stable coefficient of friction in IPA, Benzine and TCDS treated samples. Water rinsed samples have reduced friction coefficient, however a steady rise in friction is observed, similar to the samples as-delivered. Experimental results show that IPA and benzine treatments yield similar friction despite significantly differing in carbon concentration as measured by XPS. To note is that the ultrahigh vacuum environment during XPS measurements do not allow for characterization of more volatile weakly adsorbed molecules. The degree of surface adsorption in experimental conditions may therefore differ from that measured by XPS. Nevertheless, in general, friction coefficient has an inverse correlation with

Table 5.1 – Elemental composition from XPS analyses

Sample	C 1s (at%)	O 1s (at%)	Si 2p (at%)	O:Si
As-delivered	5.9	65.5	28.7	2.28
Water	6.0	65.1	28.9	2.25
IPA	10.6	61.6	27.8	2.22
Benzine	37.2	42.5	20.4	2.08
TCDS	38.2	40.8	21.0	1.94

**Figure 5.20** – C1s emission intensity from XPS analyses

atomic concentration of carbon and oxygen to silicon ratio. These results suggest an influence of carbon concentration or surface hydration of silicon dioxide on friction and its evolution. The presence of carbon has a lubricating effect, and inhibits the increase in friction.

The surface treatments also have a significant effect on the recoverable phenomena of friction observed previously. Water rinsed samples exhibit very little recovery in the friction upon interruption of sliding. IPA and benzine treated samples show a recoverable behavior in the opposite direction. TCDS treated samples show no recoverable behavior at all. Recoverable behavior of friction is likely dependent on the chemical state of the surface, possibly due to environmental adsorption or surface diffusion of adsorbents. The effects of these chemical processes on friction evolution persist even over several hours and tens of thousands of cycles.

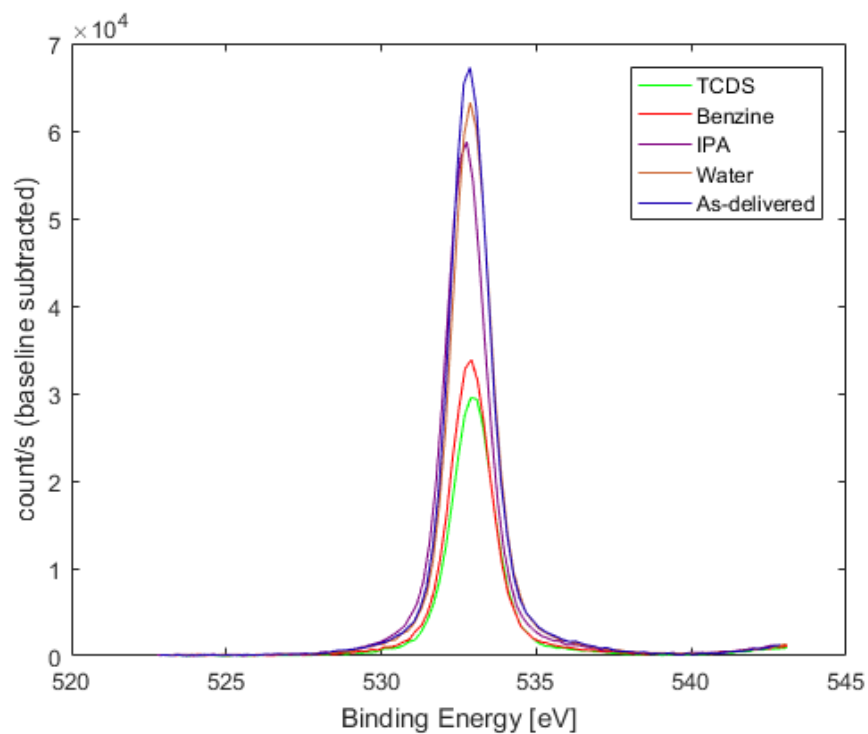


Figure 5.21 – O1s emission intensity from XPS analyses

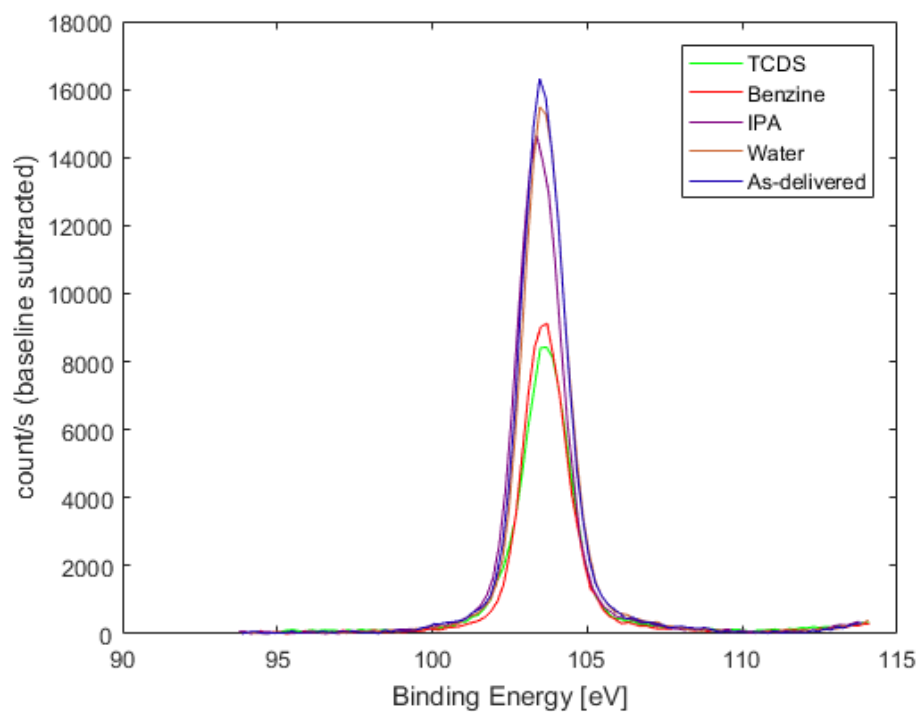


Figure 5.22 – Si2p emission intensity from XPS analyses

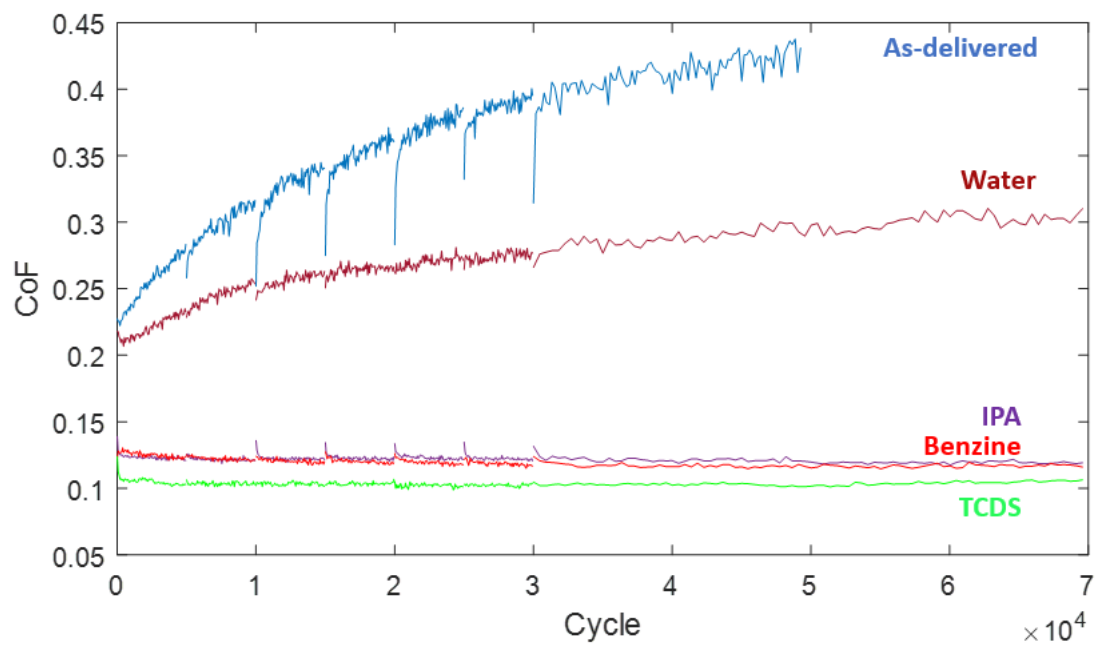


Figure 5.23 – Coefficient of friction evolution of 70000 cycles at 1 Hz, 8 mm/s, 1 mN, 2 mm sliding length, with 15 s interruptions every 5000 cycles up to 30000 cycles, after various cleaning pretreatments including IPA, benzine, water and TCDS

5.5 Effect of Topography

Samples of varying topography R5A, R5B and R5C, were compared by performing identical tribological experiments as done previously over 5000 cycles. The results, plotted in Figure 5.24, show the friction behavior across multiple experiments under identical conditions. For high roughness samples, there may be a region of highly variable friction in the first few hundred cycles, after which it stabilizes. A possible explanation is run-in behavior of wear. Sample surfaces have been observed to verify the presence of such wear.

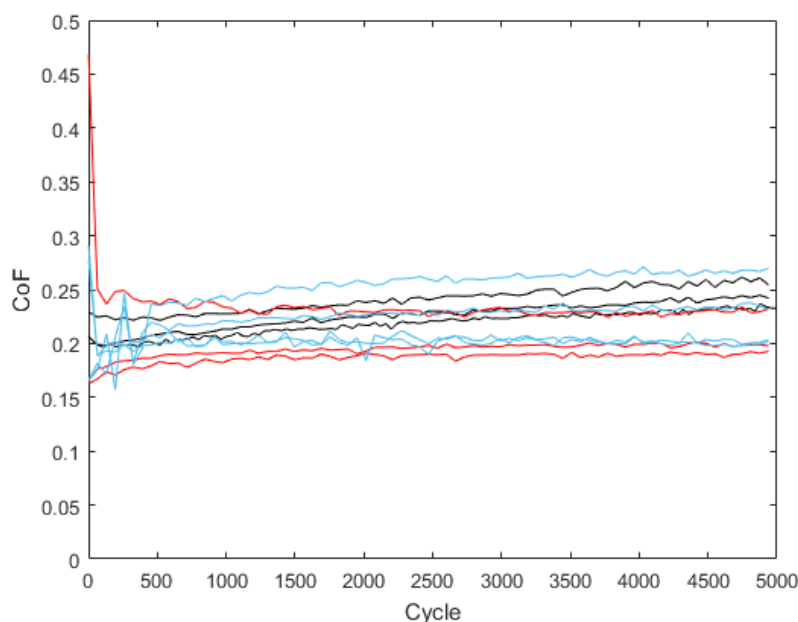


Figure 5.24 – Coefficient of friction evolution of R5A samples over 5000 cycles at 1 Hz, 8 mm/s, 1 mN, 2 mm sliding length, with samples R5A (black), R5B (red) and R5C (blue)

Shown in Figure 5.25 and Figure 5.26 are SEM images of the surface which were taken before and after the experiment respectively. The SEM image after the experiment shows an altered contrast pattern suggestive of significant surface deformation, however, further topographic analysis would be necessary to verify the presence and degree of surface deformation.

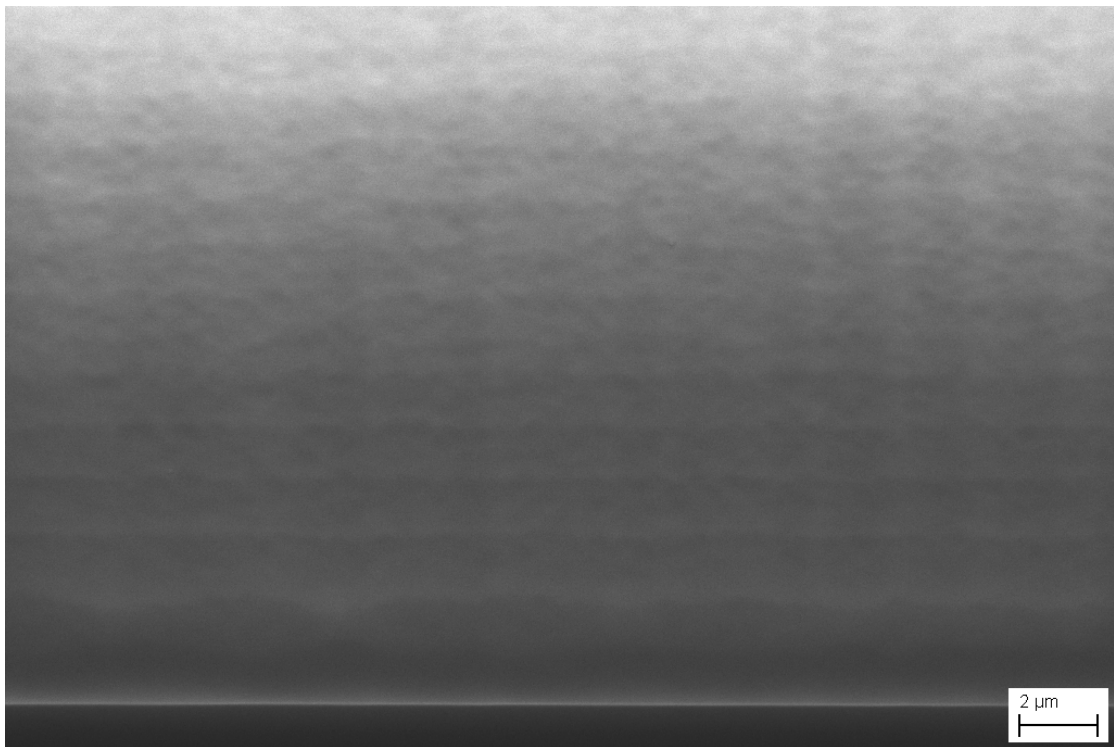


Figure 5.25 – SEM image of flat surface of R5B before experiment

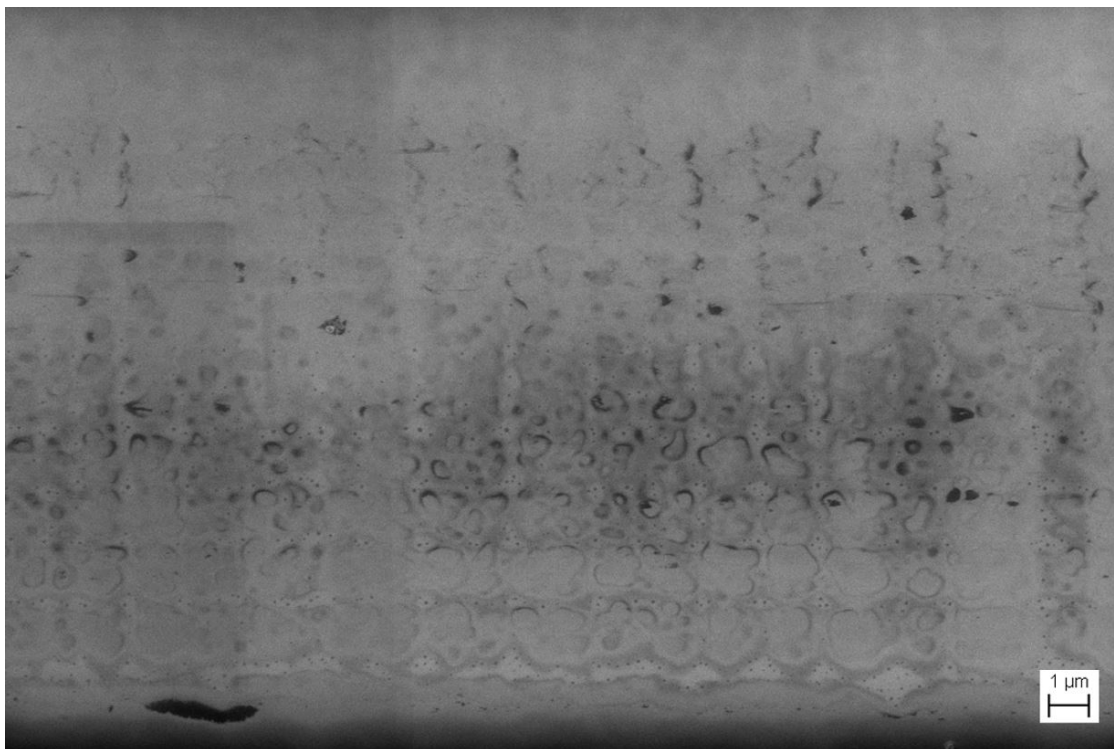


Figure 5.26 – SEM image of flat surface of R5B after 5000 cycles under 1 mN.

In order to further observe the presence of wear, SEM images of the cylinder counterpiece after the experiment were taken, as shown in Figure 5.27. Circled in red are the regions of contact. Flattening of the cylinder edge is observed in R5B and R5C samples at 1 mN load, which further suggests the occurrence of the polishing wear observed previously in experiments at high loads. Similar to the experiments at high loads, high contact pressures in the high roughness samples may lead to wear.

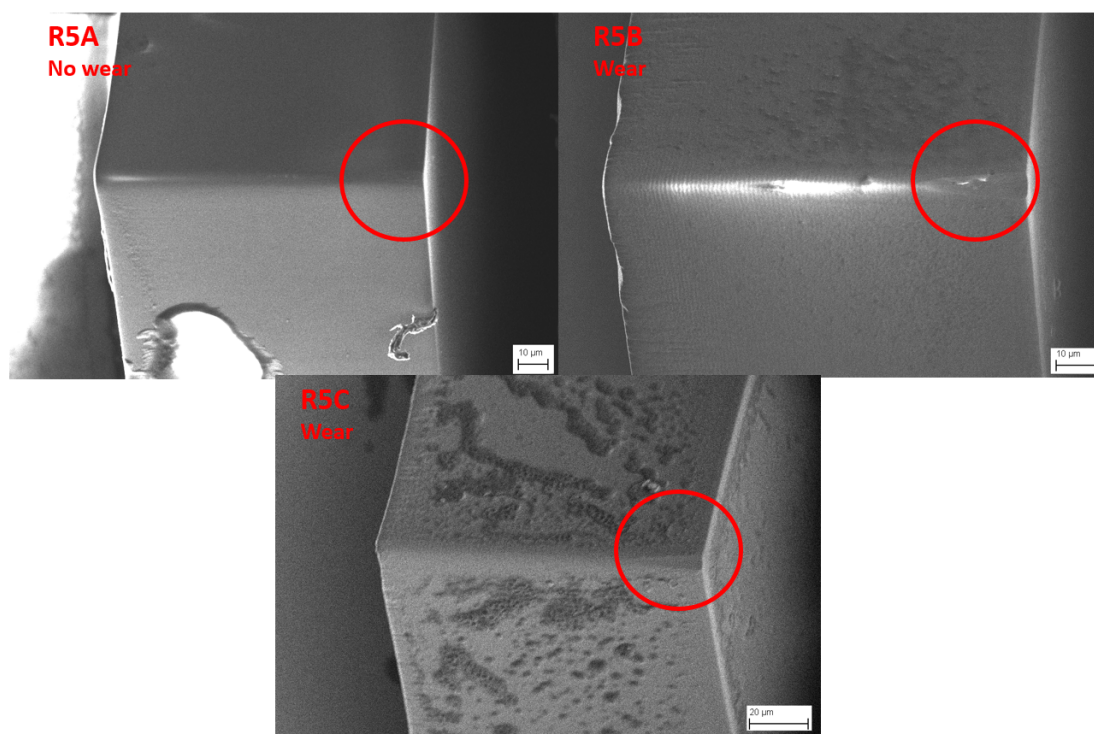


Figure 5.27 – SEM images of cylinder body of samples R5A, R5B and R5C after tribological experiments at varying 1 mN load. Red circles indicate region of contact.

Experiments with low load of 0.1 mN over 5000 cycles were performed in order to reduce contact pressures and limit wear. The results for friction evolution are shown in Figure 5.28. In the rough samples, there is high variance of friction evolution, ranging from 0.15 to 0.35. The low loads result in a friction coefficient that is highly sensitive to changes in tangential force. Additionally, small contact dimensions at low loads result in high variability of roughness in the path of sliding.

At the low loads with R5B samples no wear trace can be observed on the flat surface by SEM. SEM images of the cylinder are shown. There is no sign of wear in samples R5A, R5B and R5C. Sample R5D with the greatest surface roughness shows large-scale fracture at the contact edge. Again, the results show that the occurrence of wear may be linked to contact pressure.

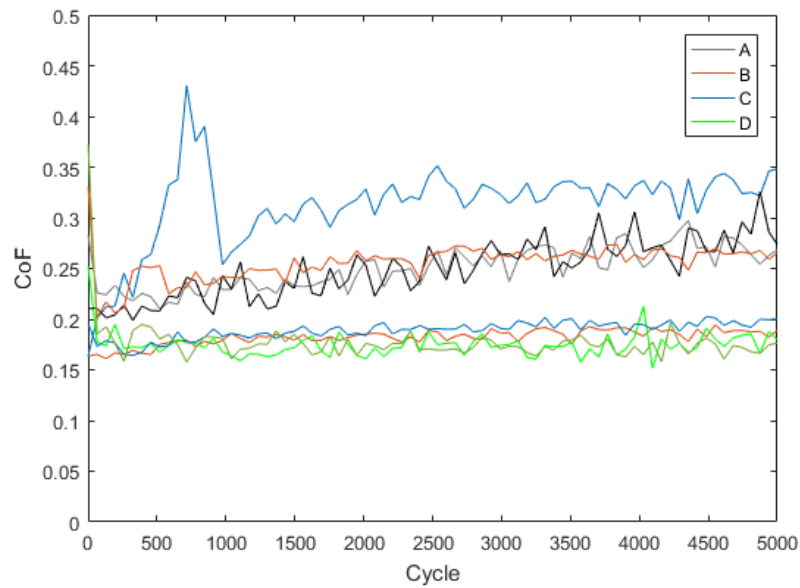


Figure 5.28 – Coefficient of friction evolution of R5A samples over 5000 cycles at 1 Hz, 8 mm/s, 0.1 mN, 2 mm sliding length, with four different surface topographies.

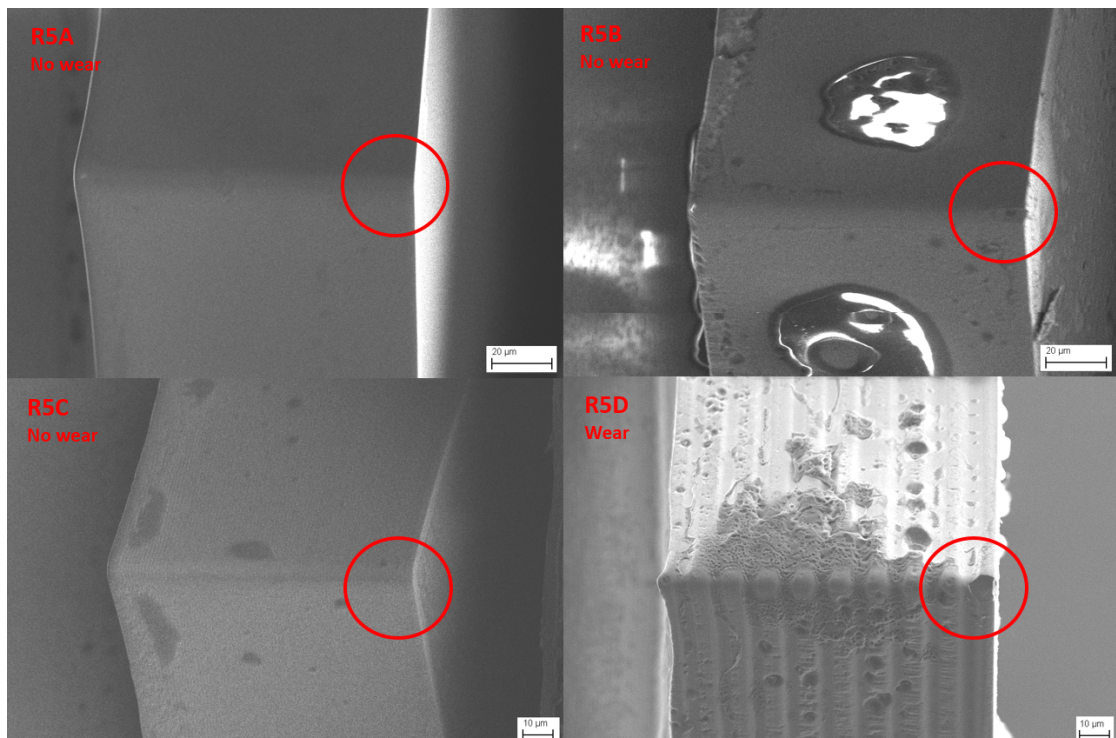


Figure 5.29 – SEM images of cylinder body of samples R5A, R5B, R5C and R5D after tribological experiments at varying 0.1 mN load. Red circles indicate region of contact.

5.6 Discussion

Experimental results showed a dependence of friction force on contact radius. The greater contact area with high contact radius, as modeled by BES, may provide an explanation. It was further observed that in high load conditions, the friction force after multiple sliding cycles is highly influenced by the differences in contact area. The results suggest that the contact area is a primary factor of friction evolution, however it has no clear effect on initial friction. The initial friction coefficient remained between 0.20 and 0.25 regardless load conditions.

As previously shown, wear is not observed in R5A samples under the 1 mN load conditions applied. However, in cases of increased load or increased roughness, the tribosystem may experience high contact pressures, which then lead to the polishing run-in type of wear observed. This is most easily seen in SEM images of the cylinder body, where the contact point is clearly visible. The original state of the cylinder bodies for samples R5A, R5B, R5C and R5D were shown previously in Figure 3.6. The edge should be smooth with uniform curvature. No deformation of the cylinder is observed for experiments of R5A samples at 2 mN or below, suggesting there exists a contact pressure threshold above which wear is observed. SEM images of samples of varying topographies showed signs of wear in R5B and R5C samples at 1 mN, where a flattening of the cylinder edge is observed. R5D samples at 0.1 mN show large scale fracture at the cylinder edge, which could also be due to wear. Using BES the maximum contact pressures may be calculated for each sample topography and load configuration. Shown in Figure 5.30, the observation of wear is indicated for a given load and contact pressure. A threshold maximum contact pressure may be determined to be approximately 1.7 GPa, above which wear will occur. This threshold pressure depends on the BES, which is performed for each topography. Simplifications of the tribosystem in the BES method may lead to errors that will vary for each sample topography. The threshold F_N and θ are shown in Figure 5.31 for a threshold P_{\max} of 1.7 GPa. Values of F_N and θ greater than the threshold curve result in P_{\max} greater than the wear threshold.

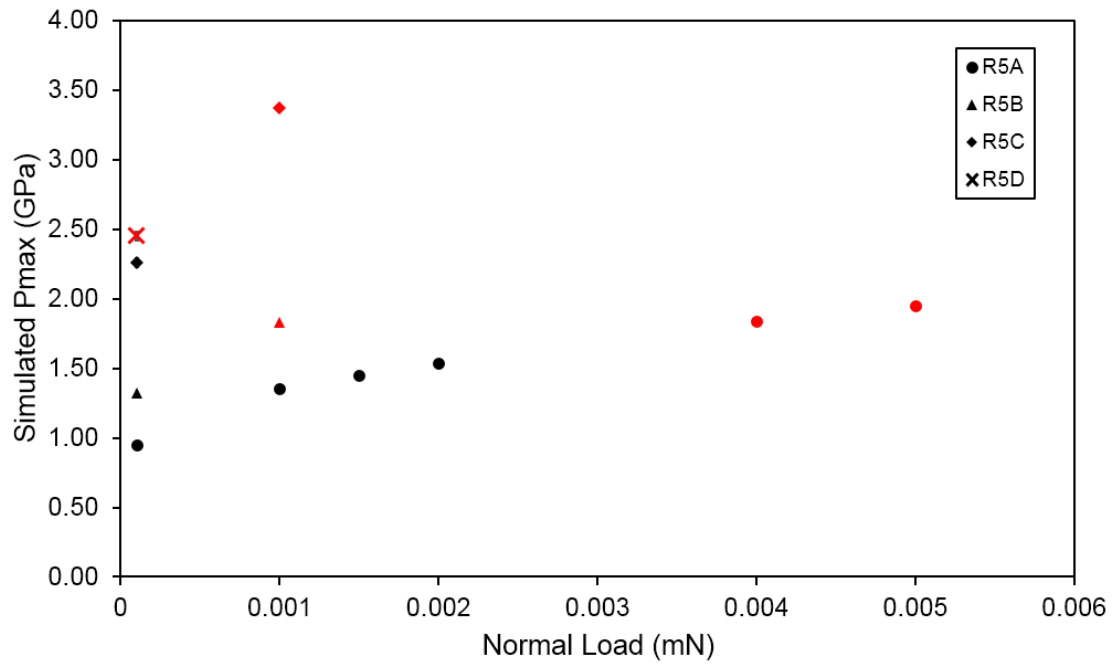


Figure 5.30 – Presence of wear for various contact pressures and contact forces for various sample topographies after 5000 cycles. Red points indicate wear observed by SEM imaging of cylinder.

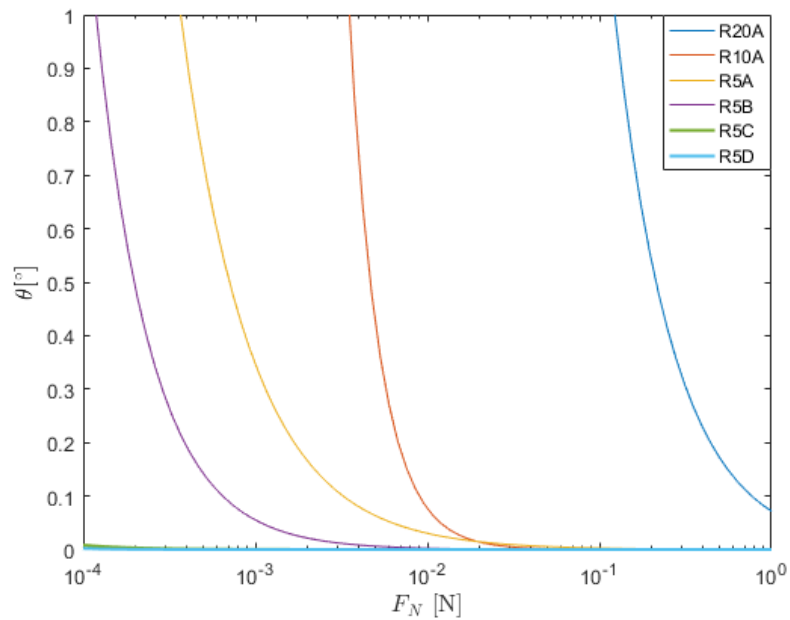


Figure 5.31 – Threshold F_N and θ for a threshold P_{\max} of 1.7 GPa based on BES.

Interrupted experimental results showed two characteristic features: (1) a rapid increase in friction in the first few hundred cycles that is recovered upon interruption, and (2) a steady cumulative increase in friction over time. This evolution of friction occurs even in cases where no topological changes in the surfaces of the samples are observed, through SEM observation and AFM profiles. This means that in these cases, wear or plastic deformation of the surface is insignificant. This corresponds to observations in industry, and shows that surface deformation cannot account for the friction evolution. Subsurface deformation of the material or chemical changes in the surface may have effects on friction. Possible explanations are surface or subsurface cracks, and adsorption of foreign species.

Experimental results with different surface treatments show that surface chemistry is a significant factor influencing friction. It affects the magnitude of friction, and both the recoverable and cumulative behaviors of friction evolution. Carbon adsorption from the various pretreatment processes correlates with lower values of friction. It also tends to suppress both the recoverable phenomenon and the cumulative increase in friction. The change in surface chemical state from various surface treatments may have influenced environmental adsorption or surface diffusion of adsorbents.

The next step is to develop a predictive model that can incorporate the observed phenomena. The primary observations considered are the two types of time-dependent behavior, the lack of topographical change, the dependence on contact area, and the dependence on surface chemistry.

6 Modeling Friction

6.1 Introduction

As described in the previous chapter, experimental results show characteristic behaviors in the evolution of friction. Shown in Figure 6.1 is an experiment over 70000 cycles at 1 Hz frequency. Firstly, there is a recoverable short time-scale phenomenon within the first few hundred cycles in which the friction coefficient increases from approximately 0.22 to 0.3. Secondly, there is a cumulative long time-scale phenomenon wherein the friction increases continually from 0.3 to greater than 0.4, and in some cases approaching 0.55.

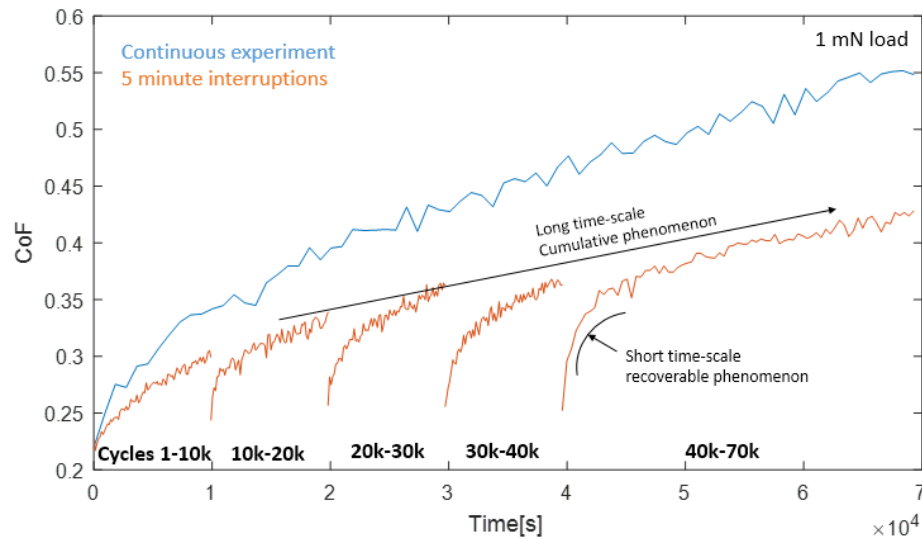


Figure 6.1 – Friction experiments with 1 mN load, 2 mm sliding distance and R5 samples over 70,000 cycles. The blue curve represents one continuous experiment and the orange curve represents one experiment with brief interruptions at 10k, 20k, 30k and 40k cycles.

SEM imaging and AFM measurements of the results before and after the tribological experiments have shown no topographical changes in the surface. There is no plastic deformation of the surface, and no wear particles observed. Third body effects can be excluded and surface topography can be considered constant throughout the experiment. Three factors are proposed as the main contributors to friction: (1) shear of adhered asperity junctions in the contact, (2) elastic deformation from vertical indentation and (3) elastic deformation from tangential sliding. Figure 6.2 illustrates the three mechanisms.

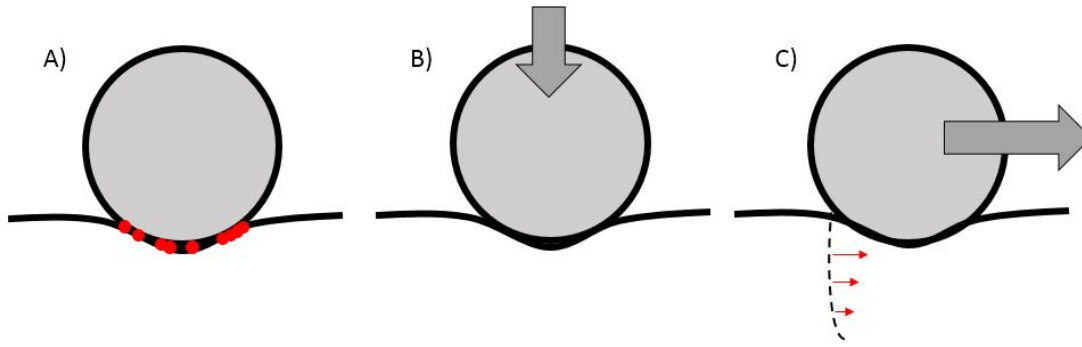


Figure 6.2 – Simplified illustration of modeled friction mechanisms: (A) adhesion of junctions in the contact (B) elastic deformation from vertical indentation (C) elastic deformation from tangential sliding which may generation and open cracks

The contributions to observed frictional energy during tribological experiments can be expressed as an energy balance, as shown in Equation 6.1, where the measured frictional energy during sliding is equal to the components of the three aforementioned friction mechanisms.

$$\mu F_N d = E_{ad} + E_{Ez} + E_{Ey} \quad (6.1)$$

where μ represents the measured frictional coefficient, F_N the normal load, d the sliding distance, E_{ad} the energy of shearing adhered asperities, E_{Ez} the elastic energy of vertical indentation, and E_{Ey} the elastic energy of tangential deformation. A time dependent model must be developed to describe the evolution of these three phenomena. It must account for both the recoverable and cumulative behavior of friction observed experimentally.

E_{ad} is dependent on surface shear strength. Chemical modifications of the surface, such as from adsorbed contaminants, may alter the surface shear strength and thus affect the friction. Sliding during the tribological experiment may further alter the surface chemistry. A transition in surface chemistry could be expected at the start and end of the experiment, which leads to the recoverable friction phenomenon observed.

E_{Ez} is described by the energy of the Hertzian contact. This energy is recovered in elastic recovery of the material. During lateral motion of the bodies in contact however, loss of a portion of this elastic recovery energy can be expected.

E_{Ey} can be increasingly significant in rough surfaces or surfaces with high crack or defect density. In rough surfaces, asperities are free to independently deform, and in cracked surfaces, material between cracks are free to independently deform.

Crack formation has been observed in contacts of rigid glass materials. During sliding, traction at the tailing end causes tensile stresses that induce crack growth at sites of defects and nanocracks where stress intensity is greatest. In brittle solids, their propagation may lead to a series of cracks along the length of the sliding track as shown previously in Figure ???. The

cracking may alter the elastic response of the material during sliding, which may be predicted with the simplified model described herein.

6.2 Energy of Adhesion E_{ad}

E_{ad} can be described in terms of a frictional force required to overcome adhesion of asperity junctions shown below. This adhesion force is proportional to the normal force and this proportionality is described by the coefficient of friction due to adhesion, μ_{ad} .

$$\begin{aligned} E_{ad} &= F_{ad}d \\ E_{ad} &= \mu_{ad}F_Nd \end{aligned} \quad (6.2)$$

The frictional energy to shear the adhered asperity junctions depends on surface state. Given an adsorbed contaminant layer, friction will vary between that of the contaminant layer and that of the bare surface. As observed in experiments, the initial friction coefficient, when the surface is contaminated, is not dependent on contact area. Meanwhile as sliding cycles increase and contamination is removed, the friction may be contact area dependent. Let μ_1 represent friction of a contaminated surface and let μ_2 represent friction of a bare surface. In the case of area dependence, the tangential force required for sliding is equal to the shear strength τ applied on the contact area A . Therefore, μ_2 can be described as follows:

$$\mu_2 = \frac{\tau A}{F_N} \quad (6.3)$$

The mechanisms governing μ_1 are thus far undetermined. It will be modeled as a free parameter, likely dependent on surface chemistry. Over increasing sliding cycles, the friction approaches μ_2 from μ_1 , as contaminants are removed. ϕ may be introduced, varying from 0 to 1, representing the fraction of the surface covered by adsorbed contaminants. The transition between μ_1 and μ_2 can be simply approximated by a linear relation with ϕ as follows:

$$\begin{aligned} \mu_{ad} &= \phi\mu_1 + (1 - \phi) \frac{\tau_2 A}{F_N} \\ &= \phi\mu_1 + (1 - \phi)\mu_2 \\ &= \phi(\mu_1 - \mu_2) + \mu_2 \end{aligned} \quad (6.4)$$

The recoverable short time-scale friction behavior from the interrupted tests in Figure 6.1 can be modeled as a simple balance of fluxes of contaminant material removal and accumulation on the surface of the contact. This is simply depicted in Figure 6.3 with $\frac{d\phi_a}{dt}$ and $\frac{d\phi_r}{dt}$ representing the changes in surface coverage from adsorption and removal of contaminants from the surface respectively.

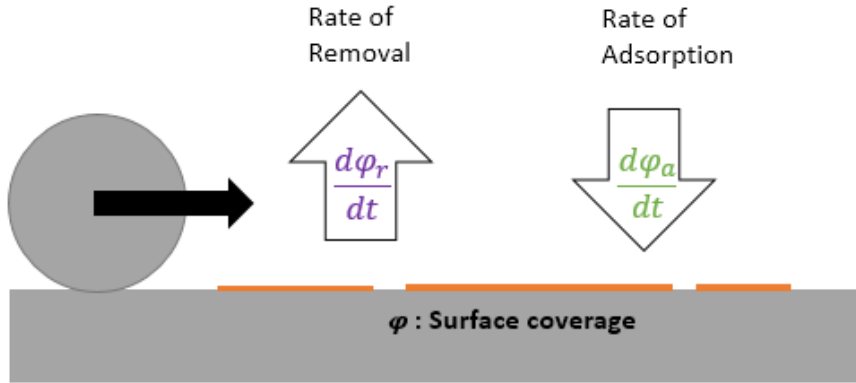


Figure 6.3 – Simplified model of contaminant layer accumulation and removal. Accumulation occurs from adsorption of contaminants in the environment and removal occurs from desorption and wear.

Overall, the change in surface coverage can be represented by Equation 6.5:

$$\frac{d\phi}{dt} = \frac{d\phi_a}{dt} - \frac{d\phi_r}{dt} \quad (6.5)$$

where ϕ represents the surface coverage as a value between 0 and 1. The friction coefficient, as a simplification, may vary between that of a fully covered surface μ_1 and a bare surface μ_2 . As an approximation it is assumed the variation of the friction coefficient is linearly correlated with surface coverage, which yields the following equation:

The changes in surface coverage can be defined by rate constants. Assuming a Langmuir isotherm adsorption model, the rate of adsorption would be a function of partial pressure expressed as follows:

$$\frac{d\phi_a}{dt} = k_a p (1 - \phi) \quad (6.6)$$

where k_a is the rate of adsorption, and p is the partial pressure of the contaminant. Although gas adsorption on the surface is assumed by this model, adsorbed layers may also be formed through surface diffusion. In the case of surface diffusion, p would represent a surface density of adsorbents. The rate of removal of contaminant has two components, one due to wear during sliding and one based on desorption, expressed as follows:

$$\frac{d\phi_r}{dt} = k_r \phi \quad (6.7)$$

where k_r is a wear constant. Solving the differential equation 6.5 proceeds with multiplying both sides by a multiplicative inverse, which allows simplification by product rule. The solution

requires introduction of an integration constant c .

$$\begin{aligned}
 \frac{d\phi}{dt} e^{(k_a p + k_r)t} &= k_a p e^{(k_a p + k_r)t} - (k_a p + k_r) \phi e^{(k_a p + k_r)t} \\
 \frac{d\phi}{dt} e^{(k_a p + k_r)t} + (k_a p + k_r) \phi e^{(k_a p + k_r)t} &= k_a p e^{(k_a p + k_r)t} \\
 \frac{d}{dt} \left(\phi e^{(k_a p + k_r)t} \right) &= k_a p e^{(k_a p + k_r)t} \\
 \phi e^{(k_a p + k_r)t} &= \frac{k_a p e^{(k_a p + k_r)t}}{k_a p + k_r} + c \\
 \phi &= \frac{k_a p}{k_a p + k_r} + c e^{-(k_a p + k_r)t}
 \end{aligned} \tag{6.8}$$

The integration constant may be expressed in terms of initial surface coverage:

$$c = \phi_0 - \frac{k_a p}{k_a p + k_r} \tag{6.9}$$

where ϕ_0 represents initial surface coverage. Equation 6.8 can be substituted into equation 6.4 to yield an expression for friction as a function of the rate constants.

$$\mu_{ad} = \left(\phi_0 e^{-(k_a p + k_r)t} + \frac{k_a p}{k_a p + k_r} \left(1 - e^{-(k_a p + k_r)t} \right) \right) (\mu_1 - \mu_2) + \mu_2 \tag{6.10}$$

One should note that ϕ is bounded to values between 0 and 1. The friction coefficient of a fully contaminated surface μ_1 , as well as the rate constants k_r and k_a , and the friction coefficient of a bare surface μ_2 must be experimentally determined.

Finally, a steady state solution can be determined by taking the limit of time to infinity:

$$\mu_{ss} = \frac{k_a p}{k_a p + k_r} (\mu_1 - \mu_2) + \mu_2 \tag{6.11}$$

In the steady state, the surface coverage is constant and the friction varies solely with μ_2 , which is given from the model based on the effects of crack growth on frictional energy.

6.3 Vertical Elastic Deformation E_{Ez}

Energy of vertical elastic deformation is derived from equations for a Hertzian ball-on-flat contact as shown in Figure 6.4. A ball is used to approximate the radius of contact observed experimentally. The depth δ and width b can be analytically derived using the Hertzian model. E_{Ez} is approximated as a portion of the indentation energy of repeated vertical indents of interval b over the path of sliding.

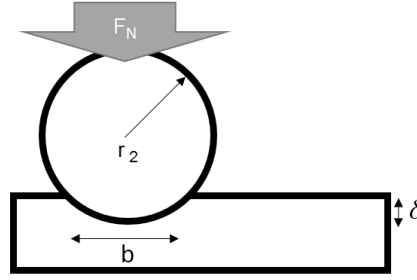


Figure 6.4 – Cross-sectional profile of indentation of a ball on flat surface

The Hertzian reduced elastic modulus for self-mated contacts is given by the equation:

$$E^* = \frac{E}{2(1-\nu^2)} \quad (6.12)$$

where E represents bulk elastic modulus and ν represents Poisson's ratio.

From the reduced elastic modulus, indentation depth is given by the equation:

$$\delta = \left(\frac{1}{r} \left(\frac{3F_N}{4E^*} \right)^2 \right)^{1/3} \quad (6.13)$$

The total work of indentation at one indentation is given simply by the product of normal load and distance. Energy of elastic recovery that is lost during sliding contributes to friction. The proportion of energy lost, α , is a constant between 0 and 1.

$$\begin{aligned} E_{indent} &= F_N \delta \\ E_{Ez} &= \alpha F_N \delta \end{aligned} \quad (6.14)$$

Substituting Equation 6.13 yields equations for energy.

$$E_{Ez} = \alpha \left(\frac{F_N^5}{r} \left(\frac{3}{4E^*} \right)^2 \right)^{1/3} \quad (6.15)$$

The equation may be expressed in terms of a friction coefficient over a distance of, b .

$$\mu_{Ez} = \frac{\alpha}{b} \left(\frac{1}{r} \left(\frac{3F_N}{4E^*} \right)^2 \right)^{1/3} \quad (6.16)$$

Given constant surface topography and geometry, as observed experimentally, E_{Ez} is also constant.

6.4 Tangential Elastic Deformation E_{Ey}

6.4.1 Shear Strain Model

The energy of lateral elastic deformation can be simplified using an idealized model of independently deforming segments. The dimensions of the segments depend on geometry of the contact. The width of the segments is assumed to be equal to the Hertzian contact diameter. The depth of the segments represent crack length if cracks exist, or asperity height if there is a rough surface.

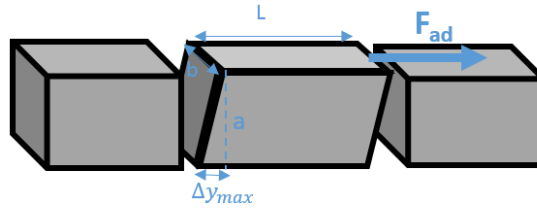


Figure 6.5 – Model of deformation on the surface along the sliding track as rectangular segments free to deform in shear mode with length L , width b and depth a .

The shearing force over one rectangular segment can be given as a function of shear modulus, G , and deformation length, Δy . Energy of deformation is derived from the integral of force over the deformation length.

$$F_{ad} = \frac{GLb\Delta y}{a} \quad (6.17)$$

$$E_{Ey} = \frac{1}{2} \frac{GLb}{a} \Delta y^2 \quad (6.18)$$

Substitution of the previous expressions to eliminate Δy yields and expression for total energy of tangential elastic deformation. The force that applies the deformation is the adhesive force described in Section 6.2.

$$\begin{aligned} F_{ad} &= \mu_{ad} F_N \\ E_{Ey} &= \frac{1}{2} \frac{a F_{ad}^2}{GbL} \\ E_{Ey} &= \frac{a F_N^2 \mu_{ad}^2}{2GbL} \end{aligned} \quad (6.19)$$

The expression may be put in terms of friction, over a distance of L . Under these shear strain conditions, depth of the segment is linearly proportional to the friction contribution of tangential elastic deformation.

$$\mu_{Ey} = \frac{a F_N \mu_{ad}^2}{2GbL^2} \quad (6.20)$$

6.4.2 Cantilever Beam Model

For segments of large depth, energy of lateral elastic deformation can be simplified using an idealized model involving a series of cantilever beams, shown in Figure 6.6. Each cantilever is independent and the force of sliding is assumed to act on one cantilever at a time.

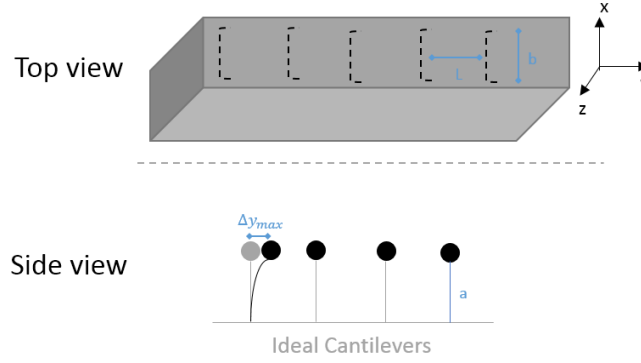


Figure 6.6 – Model of cracks on the surface along the sliding track as ideal rectangular cantilevers of length a and width b

The spring constant k is determined from the equation for an ideal cantilever and the moment of inertia I is determined for that of a rectangular prism.

$$k = \frac{3EI}{a^3} \quad (6.21)$$

$$I = \frac{bL^3}{12} \quad (6.22)$$

Given the spring constant, the force acting on the cantilever can be related to the deflection y_{\max} . This force is at most the adhesion force F_{ad} .

$$F_{ad} = k\Delta y_{\max} \quad (6.23)$$

The total sum energy of lateral deflection of one spring over distance L can be calculated from Equation 6.24. Substituting in Equations 6.23 and 6.21, yields an expression for total elastic energy of spring deflection per stroke.

$$E_{Ey} = \left(\frac{1}{2} k \Delta y_{\max}^2 \right) \quad (6.24)$$

$$E_{Ey} = \frac{2da^3F_T^2}{EbL^3} \quad (6.25)$$

The expression may be put in terms of friction, over a distance of L . Under the cantilever beam condition, depth of the segment is has a cube relation to the friction contribution of tangential elastic deformation.

$$\mu_{Ey} = \frac{2a^3F_N\mu_{ad}^2}{EbL^4} \quad (6.26)$$

6.4.3 Crack Growth Rate

If cracks are generated on the surface the evolution of the friction over time is linked to crack growth. Cracks are expected to grow upon each cycle. Assuming cracks are loaded sequentially with constant stress, the time of crack growth, t_g , during each cycle (two strokes) can be represented as:

$$t_g = \frac{2L}{v} \quad (6.27)$$

The crack length a , after N number of cycles, can thus be expressed in the following equation as a function of crack growth rate:

$$\begin{aligned} a(N) &= a_0 + N t_g \frac{da}{dt} \\ a(N) &= a_0 + \frac{2LN}{v} \frac{da}{dt} \end{aligned} \quad (6.28)$$

As a function of time, a parameter for sliding frequency, f , can be introduced as follows:

$$a(t) = a_0 + \frac{2Lft}{v} \frac{da}{dt} \quad (6.29)$$

Crack length can alternatively be expressed as a function cycles, which allows use of a fatigue model to predict crack growth.

$$a(N) = a_0 + N \frac{da}{dN} \quad (6.30)$$

In either case, in order to determine crack growth rate, stress intensity factor at crack tips under mode I can be estimated. Assuming, uniform tensile stress of an edge crack in a plate of infinite width and depth, the stress intensity factor can be approximated from the expressions [58]:

$$\sigma_T = \frac{F_T}{Lb} \quad (6.31)$$

$$K_I = 1.122\sigma_T\sqrt{\pi a} \quad (6.32)$$

The maximum tensile stress can be approximated from Hamilton & Goodman [59], which allows estimation of K_I . Literature values of crack growth rate under static stress can be referenced, given a known K_I . This allows use of Equation 6.28. Alternatively, a fatigue model of crack growth such as the Paris-Erdogan model may be used:

$$\frac{da}{dN} = m_1 K_I^{m_2} \quad (6.33)$$

This fatigue cracking approach allows use of Equation 6.30, depending on two empirical constants m_1 and m_2 .

6.5 Summary

The friction observed can be expressed as a sum of the adhesion, vertical deformation and tangential deformation components.

$$\mu = \mu_{ad} + \mu_{Ez} + \mu_{Ey}$$

The adhesion component, expressed by Equation 6.10, has been derived from the Langmuir Isotherm model of adsorption. The vertical indentation component, expressed by Equation 6.16, has been derived from Hertzian indentation energy and is constant. Two models for tangential deformation have been developed, depending on depth of the deformed segments. The shear strain model, expressed by Equation 6.20, applies for cases of low depth a . It results in a linear relationship between μ_{Ey} and a . The cantilever beam model, expressed by Equation 6.26, applies for high a . It results in a cubed relationship between μ_{Ey} and a .

The global equation for friction as a function of cycles can be formulated as follows, for shear deformation mode with crack velocity defined with respect to the time:

$$\begin{aligned} \mu(t) = & \left(\phi_0 e^{-(k_a p + k_r)t} + \frac{k_a p}{k_a p + k_r} \left(1 - e^{-(k_a p + k_r)t} \right) \right) (\mu_1 - \mu_2) + \mu_2 + \frac{\alpha}{b} \left(\frac{1}{r} \left(\frac{3F_N}{4E^*} \right)^2 \right)^{1/3} \\ & + \frac{\left(a_0 + \frac{2Lft}{v} \frac{da}{dt} \right) F_N \mu_{ad}^2}{2GbL^2} \end{aligned} \quad (6.34)$$

Likewise, a global equation can be formulated as follows, for the cantilever beam deformation mode:

$$\begin{aligned} \mu(t) = & \left(\phi_0 e^{-(k_a p + k_r)t} + \frac{k_a p}{k_a p + k_r} \left(1 - e^{-(k_a p + k_r)t} \right) \right) (\mu_1 - \mu_2) + \mu_2 + \frac{\alpha}{b} \left(\frac{1}{r} \left(\frac{3F_N}{4E^*} \right)^2 \right)^{1/3} \\ & + \frac{2 \left(a_0 + \frac{2Lft}{v} \frac{da}{dt} \right)^3 F_N \mu_{ad}^2}{EbL^4} \end{aligned} \quad (6.35)$$

In this simplified model, a and μ_{ad} are parameters that are a function of time or sliding cycles. The evolution of a depends μ_{ad} and on crack growth rate. The growth rate can be determined based on either of two approaches. First is an approach under the assumption of a static stress field, which allows use of crack velocity with respect to time $\frac{da}{dt}$, as expressed by

Equation 6.28. Second is a fatigue crack growth approach, which allows use of fatigue models to determine crack velocity with respect to cycles $\frac{da}{dN}$, as expressed by Equation 6.30.

There are a number of parameters that are fixed by experimental conditions. This includes normal load F_N , sliding velocity v , sliding frequency f and contact radius r . The contact geometry and load allows derivation of contact width b . There are parameters such as E and E^* which are intrinsic properties of the materials used. The elastic energy loss constant α is likely a function of both material properties and parameters of the contact.

Parameters such as k_a , and k_r are properties that describe an adsorbent's interaction with the substrate. These parameters can be experimentally determined by analysis of the recoverable behavior of the friction. Partial pressure p depends on the environmental conditions. ϕ_0 describes the initial state of adsorption.

Friction parameters μ_1 and μ_2 must also be experimentally determined. They are parameters that describe the friction at two different surface adsorption states. They depend on the area of contact, which is fixed by the experimental conditions, and by the surface shear strength. μ_2 therefore depends on surface shear strength of a bare silicon dioxide contact, and μ_1 may vary depending on the adsorbents that are present and on surface chemistry.

Crack spacing L is unknown, and can be dependent on both contact conditions and material characteristics. A dependence of crack spacing on contact size has been shown in a model of crack propagation in the tribology of brittle materials [60]. Large defects or surface features may also create regions of high stress intensity, leading to the dependence of crack spacing on surface topography. It is a parameter that must be experimentally determined.

7 Application of Model

This chapter presents the application of the model to prediction of the experimental data. Estimated values of model parameters will be determined based on literature and experimental results. Fitting the model to a subset of experimental data is required to extract some model parameters. The extracted model parameters may then be used to extrapolate friction behavior to new conditions. The effects on the model of sliding duration, misalignment angle, load, radius, chemical treatments and topography are evaluated.

7.1 Friction Regimes

In order to assess the model, experimental results from tribological experiments with silicon dioxide samples are used. An example of the typical friction evolution is shown in Figure 7.1 for an R5A sample under 1 mN load at 1 Hz sliding frequency. The friction evolution over time may be generalized into two general regimes. The first, regime (A), is where the adhesion component governs the rate of change of friction coefficient increase and the second, regime (B), is where a change in elastic deformation energy governs the rate of change of friction coefficient. In regime (A) a rapid increase in friction coefficient is observed, which is attributed to a rapid change in the state of surface adsorption. In regime (B), the steady increase in friction is attributed to changes in elastic behavior of the material due to cracking.

The measured friction coefficient is comprised of three components. The contribution from vertical elastic deformation, $\mu_{E,z}$, is constant. The adhesion component, μ_{ad} , evolves from the initial friction to a steady-state friction, which is reached after a few hundred cycles. The tangential elastic component, $\mu_{E,y}$, is gradually rising as the material properties evolve over time. It is assumed that in regime (A) the friction evolution is dominated by the change in μ_{ad} , and in regime (B) the friction evolution is dominated by the change in $\mu_{E,y}$.

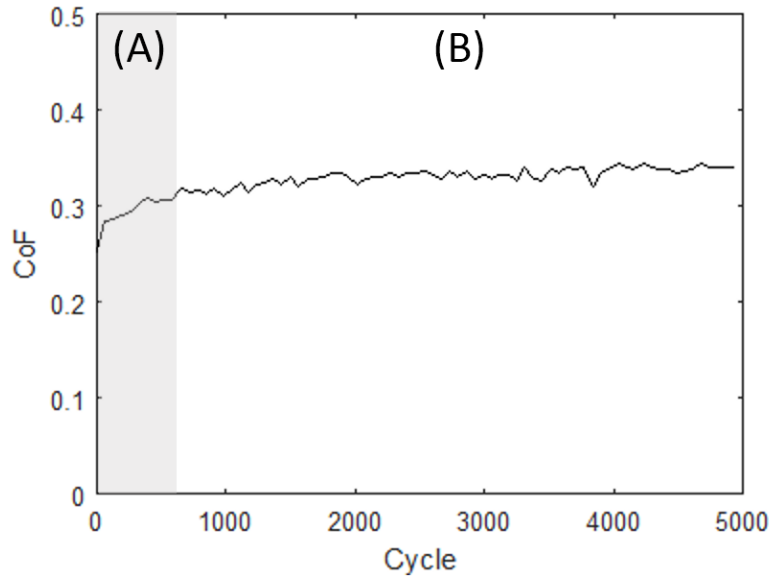


Figure 7.1 – Tribological experiment of R5A sample under 1 mN load. Two friction regimes can be observed: (A) where a rapid rise in friction may be attributed to the state of surface adsorption and (B) where a steady rise in friction may be attributed to a change in elastic properties.

7.2 Determination of Parameters

There are a number of parameters that are known from material properties or that are controlled experimentally. These include E , G , ν , F_N , v , and f . Material properties have been provided by the manufacturer where E is 70 GPa, G is 35 GPa, and ν is 0.17. Experimental parameters v and f are generally fixed for all experiments to be 8 mm/s and 1 Hz respectively. A normal load F_N of 1 mN is typically used. In experiments investigating the effects of normal load, values between 0.1 mN and 5 mN are used. The contact width b is derived directly from E , ν and F_N . Using BES, as shown in Figure 7.2, b is taken as the extremities of distance from one extremity of the contact area to another, where contact area is defined by the region with pressure greater than zero.

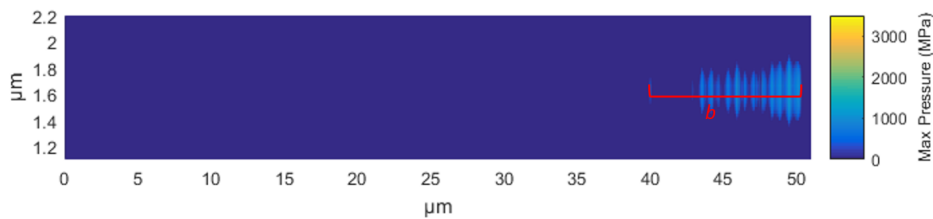


Figure 7.2 – BES of contact at 1 mN and 0.1° tilt showing the contact width b

The amount of energy lost in elastic recovery is dependent on the elastic energy loss constant α , a value between 0 and 1. This value governs the contribution of friction due to energy loss in the elastic indentation of the contacting bodies. During restitution of the

vertical elastic deformation, some energy may be lost to the environment. For the typical normal load of 1 mN, there is an energy $E_{E,z}$ of 128 nJ/cycle. This may be compared to the total work of friction experimentally observed in a stroke. With a typical initial measured friction force of 0.25 mN, and sliding length per cycle of 4 mm, the total work of friction in a cycle is approximately 1 μ J/cycle. The friction contribution $\mu_{E,z}$, is between 0 and 0.03 for α between 0 and 1. The maximum of $\alpha = 1$ is taken as an initial assumption.

The sample is left in the environment for several hours before the start of the experiment, so full surface coverage is assumed. ϕ_0 is assumed to be equal to 1. Given that friction in Regime A of Figure 7.1 is dominated by μ_{ad} , the friction values μ_1 and μ_2 can be derived experimentally. With ϕ_0 fixed to 1, μ_1 is equal to the initial μ_{ad} , which is 0.18. μ_2 is equal to the μ_{ad} at onset of the steady increase, which is the end of Regime A, which is 0.21.

The rate coefficients governing the adsorption layer k_ap and k_r are unknown but they may be derived from the tribological experiments. The friction recovery will be used to determine k_ap and the initial rise in friction of Regime A will be used to determine k_r . This procedure is described in detail in the following sections.

Crack spacing, L , is a critical parameter of the tangential deformation component of the model and is unknown. Estimation of the crack spacing may be difficult because crack presence is not easily observed. After experiments of 5000 cycles under 1 mN load, surface cracks were not observable under AFM, and SEM. Cross-sections performed using FIB across the sliding path also showed no signs of cracks. The methods used may not be sufficient to observed cracks although they may still be present. Cracks were visible in the fracture of the sample by hand shown previously in Figure 3.4. Shown in Figure 7.3, the cracks can be quantified in the oxide layer along the 21.4 μ m long dashed line. The average crack spacing in this case is 0.66 μ m. These cracks are nucleated in locations of high stress intensity, where there is high density of defects. Assuming the defect density is constant throughout the entirety of the material, cracks may nucleate on the surface during sliding with a similar periodicity. As a rough approximation, the crack frequency observed in this fracture may correspond to the frequency of probable crack nucleation sites during sliding. The crack spacing is expected to be within an order of magnitude lesser than or greater than the 0.66 μ m observed.

A range of the crack lengths a that are stable under a given load condition can be approximated using a model of crack propagation in brittle tribocontacts by Bower & Fleck [60]. Bower & Fleck's equation allows determination of the critical compressive stress, p_{\max}^{frac} , required for critical crack propagation.

$$p_{\max}^{\text{frac}} = \frac{K_{\text{IC}}}{1.121 \sqrt{\pi a \left[\mu(2 - 2.5\sqrt{a/b}) - 1.5\sqrt{a/b} + 2a/b \right]}} \quad (7.1)$$

Using the critical stress intensity, K_{IC} , for silicon dioxide of 0.77 MPa/m^{1/2} [15], and a crack width b equal to the Hertzian contact width, the critical pressure and critical crack

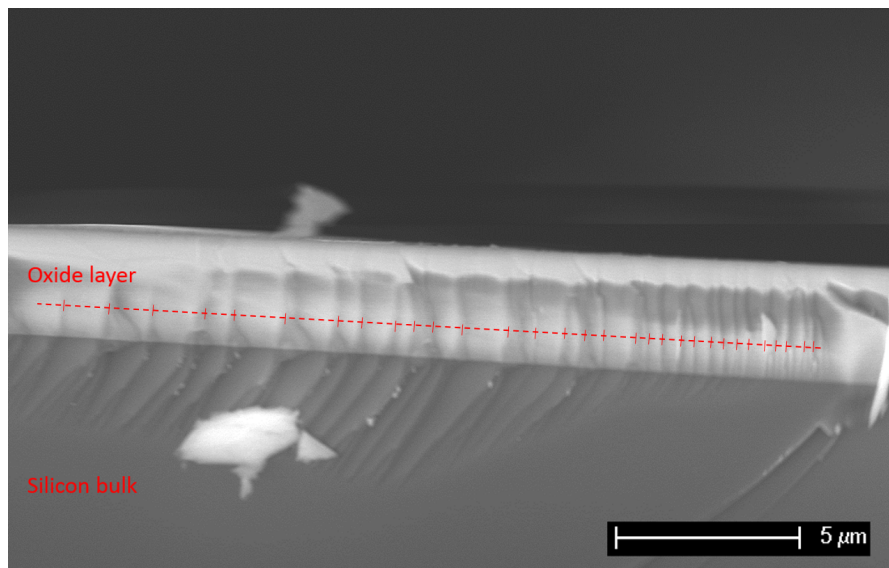


Figure 7.3 – SEM cross-section image of R5A sample fractured by hand. Cracks are visible in the oxide layer, along the dashed line.

length zones can be identified as in Figure 7.4. Under normal load of 1 mN, based on BES results, the pressures during sliding do not exceed 2000 MPa under 1 mN load conditions. The expression yields a critical crack length, a_c , of approximately 0.6 μm . Given the lack of wear in experiments, it indicates that surface cracks that exist in the sample remain below 0.6 μm in length.

Crack growth rate is a critical parameter that is unknown. Crack velocity in vitreous silica have been investigated experimentally [18], and the values may be used to estimate crack velocity in tribological experiments with to cyclical loading. The crack velocity as a function of stress intensity determined experimentally is shown in Figure 7.5. Under humid conditions, as is the case in the experiments performed, crack velocities in the order of $10^{-5.5}$ m/s or less can be expected for subcritical cracks.

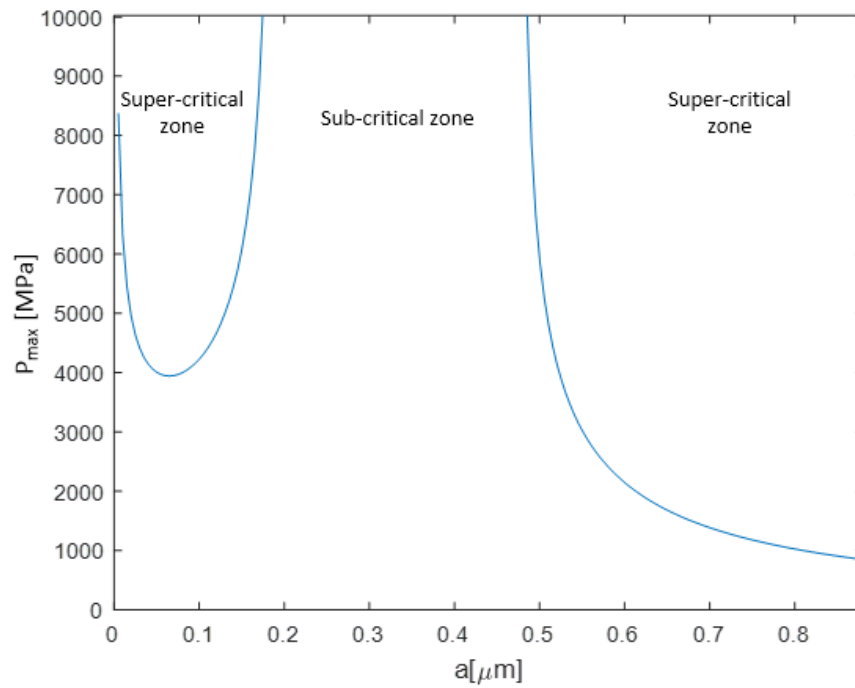


Figure 7.4 – Zones of critical crack propagation according to Bower & Fleck model given a K_{IC} of 0.77 and experimental contact geometry

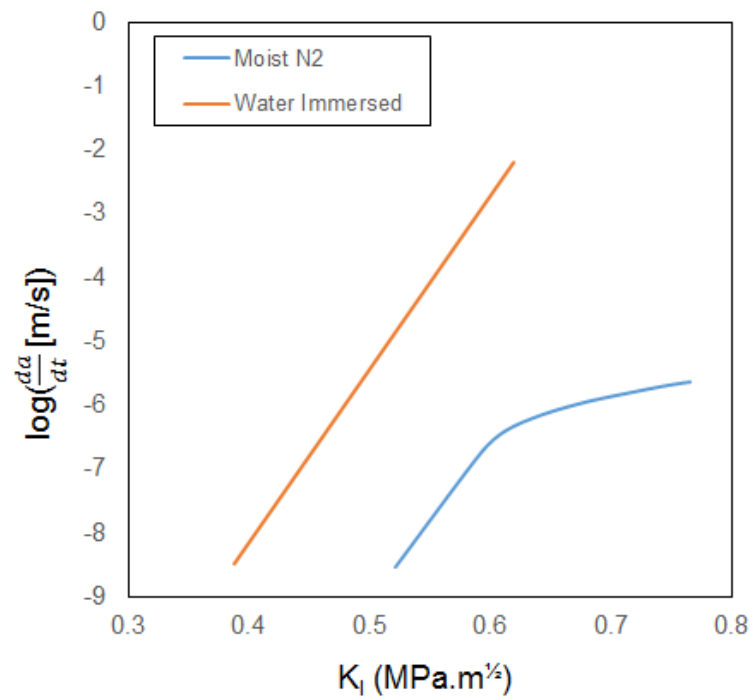


Figure 7.5 – Effect of water on subcritical crack growth in vitreous silica (curves represent best fit to experimental data extracted from [18]). Base 10 logarithm is used for crack velocity.

7.2.1 Determination of k_a & k_r

Recoverable behavior of the friction is observed in interruptions of an experiment, as shown in Figure 7.6. A rate constant can be determined that governs the recovery of friction for a given duration of interruption. Standard friction experiments as described previously were performed, but with varying interruption times. During the interruption, sliding was temporarily stopped while the counterpieces were kept in contact. Upon resumption of sliding, the friction coefficient continued to be recorded. Experiments with interruption durations of 15, 120 and 900 seconds were performed.

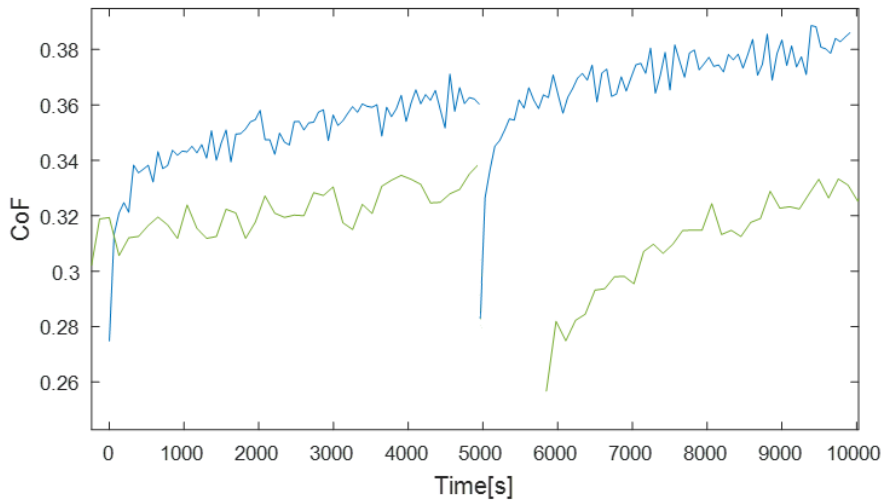


Figure 7.6 – Interrupted experiments under 1 mN load. Depicted are interruption times of 15 s (blue) and 900 s (green). The solid lines represent friction as measured by the tribometer.

The rate coefficient of adsorption, k_a , can be determined by fitting the data for recovery of friction between experiments. During this period, there is no removal of contaminants by sliding. In this domain, it can be considered that rate constant of removal k_r is zero. Additionally, as the interruptions occur in the linear regime after a long period of sliding, the surface coverage ratio φ is considered zero, representing no coverage of contaminants. In order to extract the adsorption constant based on the Langmuir kinetics, the change in the adsorption component of friction, $\Delta\mu_{ad}$, must be expressed in terms of the change in the total friction $\Delta\mu$.

$$\Delta\mu = \Delta\mu_{E,y} + \Delta\mu_{ad} \quad (7.2)$$

From Equation 6.20, it has been shown that $\mu_{E,y}$ is directly proportional to μ_{ad}^2 . This proportionality can be expressed as follows:

$$\Delta\mu_{E,y} = C\Delta(\mu_{ad}^2) \quad (7.3)$$

where, $C = \frac{aF_N}{2GbL^2}$ for shear deformation.

and, $C = \frac{2a^3F_N}{EbL^4}$ for cantilever deformation.

Equation 7.3 can be substituted into Equation 7.2 as follows:

$$\Delta\mu = C\Delta(\mu_{ad}^2) + \Delta\mu_{ad}$$

The $\Delta(\mu_{ad}^2)$ term may be expanded as follows:

$$\Delta\mu = C(\mu_{ad,f}^2 - \mu_{ad,i}^2) + \Delta\mu_{ad}$$

$$\Delta\mu = C(\mu_{ad,f} + \mu_{ad,i})(\mu_{ad,f} - \mu_{ad,i}) + \Delta\mu_{ad}$$

Given $\Delta\mu_{ad} = \mu_{ad,f} + \mu_{ad,i}$, the equation may be expressed in quadratic form:

$$\Delta\mu = C(\mu_{ad,f} + \mu_{ad,i})\Delta\mu_{ad}^2 + \Delta\mu_{ad}$$

$$\Delta\mu = C(2\mu_{ad,i} + \Delta\mu_{ad})\Delta\mu_{ad}^2 + \Delta\mu_{ad}$$

As the surface coverage is zero at the beginning of the interruption period, $\mu_{ad,i}$ is equal to μ_2 :

$$\Delta\mu = C(2\mu_2 + \Delta\mu_{ad})\Delta\mu_{ad}^2 + \Delta\mu_{ad}$$

$$\Delta\mu = C(\Delta\mu_{ad})^2 + (2C\mu_2 + 1)\Delta\mu_{ad}$$

Thus, the quadratic equation may be solved as follows:

$$\Delta\mu_{ad} = \frac{-2C\mu_2 - 1 \pm \sqrt{(2C\mu_2 + 1)^2 + 4C\Delta\mu}}{2C} \quad (7.4)$$

Using Equation 7.4, it is thus possible to extract $\Delta\mu_{ad}$ from experimental observations. Following Equation 6.10, the change in friction due to adhesion $\Delta\mu_{ad}$ can be placed in terms of time of interruption, t_{int} .

$$\Delta\mu_{ad} = (1 - e^{-k_{ap}t_{int}})(\mu_1 - \mu_2) \quad (7.5)$$

Figure 7.7 shows the relationship between $\Delta\mu_{ad}$ from Equation 7.4 and time of interruption. Black lines represent modeled changes in friction for various rate constants. Values of k_{ap} that reasonably fit the experimental data as predicted by the model are between 0.001 s^{-1} and 0.1 s^{-1} .

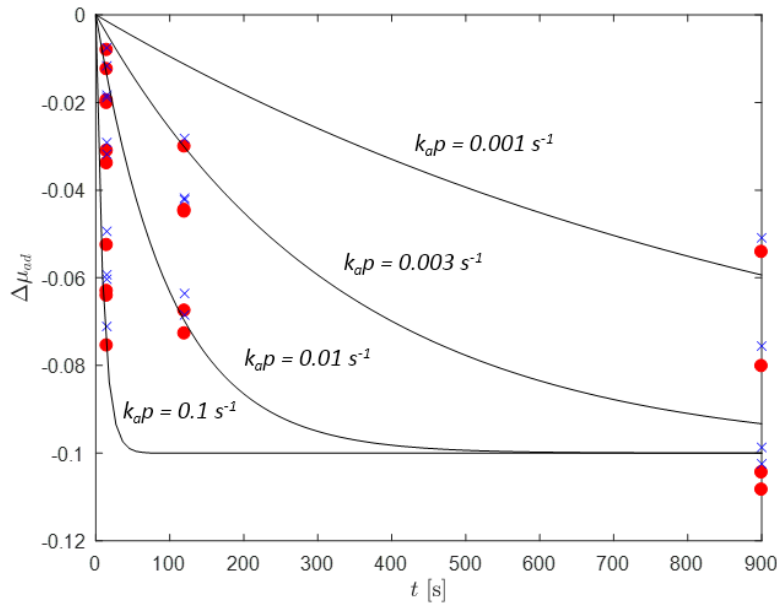


Figure 7.7 – Decrease in friction over interruption time using adsorption rate constants from experimental data of interruptions of 15 s, 120 s and 900 s. μ_{ad} is calculated using the shear model (red circles) and the cantilever beam model (blue crosses). The lines represent the modeled decrease in friction for the given rate constants k_{ap} .

The removal rate coefficient, represented by k_r in the model, describes the rate of removal of a contaminant from the surface based. This removal can be from desorption or from the shear stresses during sliding. During approximately the first 500 cycles, a regime of rapid increase in friction is observed. In this regime, it is hypothesized that there is a removal of contaminants allowing for an increase in surface adhesion. For determining the rate of removal, experimental results have had the linear increase in friction that occurs after the first 500 cycles subtracted. This linear increase was determined by linear regression of the points past 500 cycles.

Given a known rate of adsorption as determined in the previous section, rate of removal may be determined from the experimental data. The expression for the adhesion contribution of friction, Equation 6.10, was fit to experimental results. The parameter k_{ap} was fixed to 0.001 s^{-1} and 0.01 s^{-1} , which were extracted in the previous section. Average μ_1 over all experiments was determined to be 0.18. φ_0 , as discussed, may be fixed to 1 and the free parameter of k_r is fit to the data. The modeled friction evolution is compared to experimental values in Figure 7.8. The linear increase in the regime after 500 cycles was subtracted from the experimental results and a non-linear least-squares fit was performed.

The least-squares fit of the model allows extraction of the removal rate constant k_r . For a k_{ap} of 0.01 s^{-1} , it is determined that the fitted k_r is equal to 0.0026 s^{-1} . Using this k_{ap} value, the model overestimates the rate of increase in friction in the first few hundred cycles. For a k_{ap} of 0.0001 s^{-1} , the fitted k_r is equal to 3.5×10^{-5} . This results in an underestimation of the

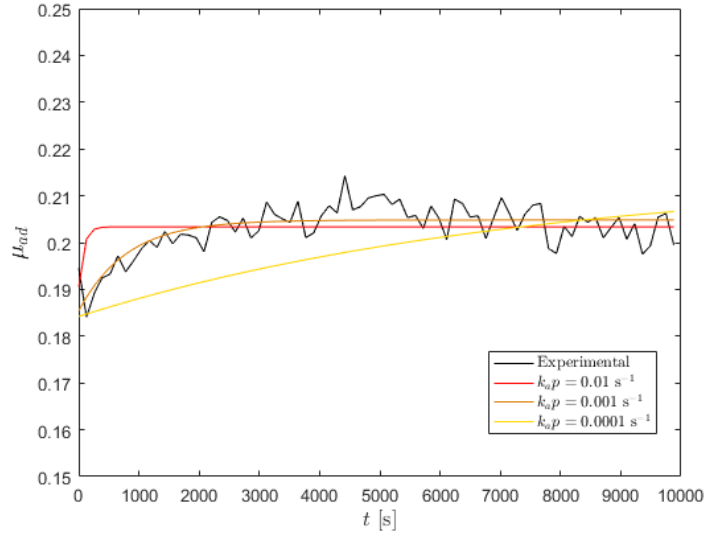


Figure 7.8 – A tribological experiment was performed under 1 mN load with 1 Hz cycle frequency with the linear increase subtracted. The linear contribution of lateral deformation has been subtracted from the results. The adhesion model was fit to the experimental results (black) with the k_{ap} value fixed to 0.001 s^{-1} (yellow) and 0.01 s^{-1} (red).

rate of increase in friction. A value for k_{ap} of 0.001 s^{-1} yields a k_r of $2.6 \times 10^{-4} \text{ s}^{-1}$. Given the interaction between k_r and k_{ap} , this combination of values provides the best approximation of the experimental data.

The fitting was performed for the friction evolution of seven independent experiments, using a k_{ap} value of 0.01 s^{-1} . The mean k_r value is $2.67 \times 10^{-4} \text{ s}^{-1}$ with a standard deviation of $1.07 \times 10^{-4} \text{ s}^{-1}$. Figure 7.9 shows the range of variability of the modeled fit based on the variance of the extracted k_r values, compared to three independent experiments.

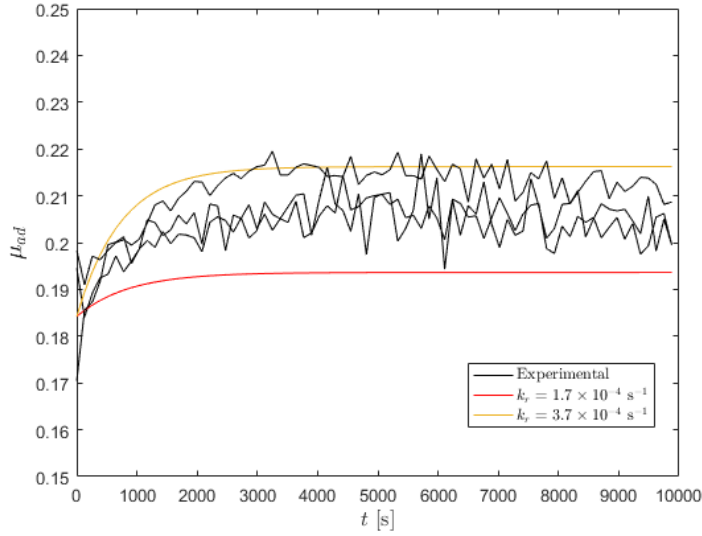


Figure 7.9 – Model fit based on k_r ranging from $1.7 \times 10^{-4} \text{ s}^{-1}$ to $3.7 \times 10^{-4} \text{ s}^{-1}$, including imposed linear growth representing cumulative increase in friction. Model fit is compared to 3 independent experiments.

7.2.2 Determination of Crack Growth

The longterm evolution of friction is highly affected by the dimensions of the elastically deformed segments between cracks as described by the model. Growth of vertical cracks in the surface during cyclical loading may effectively increase the height of these elastically deformed segments. Using typical experimental parameters the relationship between E_{Ey} and crack depth can be determined. Subtracting the elastic energy of indentation and adhesion components from the experimental results allows fitting of solely the elastic energy of tangential deformation component of friction. Experimental values of four independent experiments are shown in Figure 7.10 with E_{Ez} and E_{ad} subtracted. There is a dispersion of friction at 5000 cycles of from 0.3 to 0.7.

Equations 6.20 and 6.26 can be used to relate friction with crack growth rate, crack length and crack spacing. The time dependent components are μ_{ad} and a . The adhesion component of friction coefficient, μ_{ad} , is taken from Section 7.2.1. It was determined previously that L is around $0.66 \mu\text{m}$. The exact value of L is unknown but it will be assumed to be within an order of magnitude higher or lower. The crack length at a given time is a function of growth rate, $\frac{da}{dt}$ and initial crack length a_0 , expressed in Equations 6.28 and 6.30. The value of $\frac{da}{dt}$ is unknown. It will be assumed that $\frac{da}{dt}$ is within the range of subcritical crack velocity reported in literature of less than 10^{-5} m/s , shown previously in Figure 7.5. It will also be assumed that in the duration of the experiment, a will not exceed the limit of $0.6 \mu\text{m}$, as determined by the Bower & Fleck model shown in Figure 7.4. As an initial estimate, a_0 is fixed to zero. It is assumed for simplicity that the crack growth rate is constant.

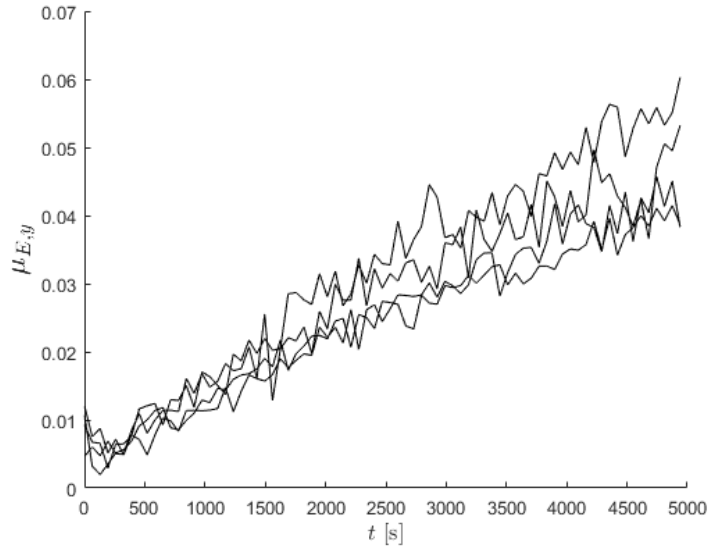


Figure 7.10 – Experimental results of R5A samples after 5000 cycles under 1 mN load with μ_{ad} and μ_{Ez} components subtracted.

Given all L and $\frac{da}{dt}$ in the valid range, the modeled cracklength after 5000 cycles, a_{5000} can be calculated. Shown in Figure 7.11 is a map of values of a_{5000} given a L and $\frac{da}{dt}$. The red region represents crack lengths greater than the $0.6 \mu\text{m}$ threshold after 5000 cycles, while the green region represents valid values of L and $\frac{da}{dt}$. The figure shows that the valid threshold crack velocities are from $10^{-7.1}$ m/s to $10^{-5.1}$ m/s. This gives a maximum crack velocity that can be restrict possible values of L and $\frac{da}{dt}$ in later analysis.

A similar approach may be taken for friction after 5000 cycles. For R5A samples, after 5000 cycles at 1 mN, μ ranges between 0.25 and 0.30. The modeled friction after 5000 cycles can also be calculated for any given L and $\frac{da}{dt}$, as shown in Figure 7.12 for the shear mode of deformation and 7.13 for the cantilever mode of deformation. The dashed red line in both figures represents the limit of $\frac{da}{dt}$ imposed by maximum crack length. The green region represents the valid range of μ at 5000 cycles that corresponds to experimental results. For the shear mode of deformation, there are no valid values of L and $\frac{da}{dt}$ within the imposed restrictions. It cannot accurately describe the growth in friction observed experimentally, whereas the cantilever mode can better describe the observed friction. L may range from 63.1 nm to 125.9 nm while $\frac{da}{dt}$ may range from $10^{-5.4}$ m/s to $10^{-5.3}$ m/s.

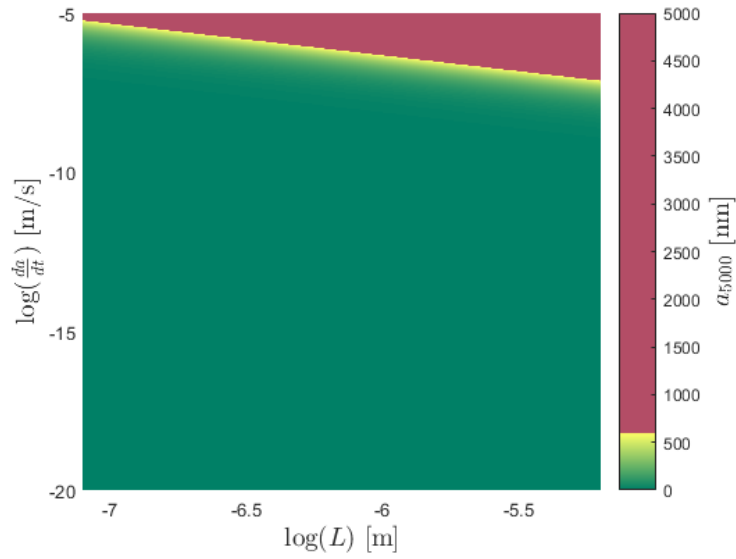


Figure 7.11 – Map of modeled values of a given a L and $\frac{da}{dt}$ for R5A samples after 5000 cycles under 1 mN load. The red region is defined by a greater than 0.6 μm .

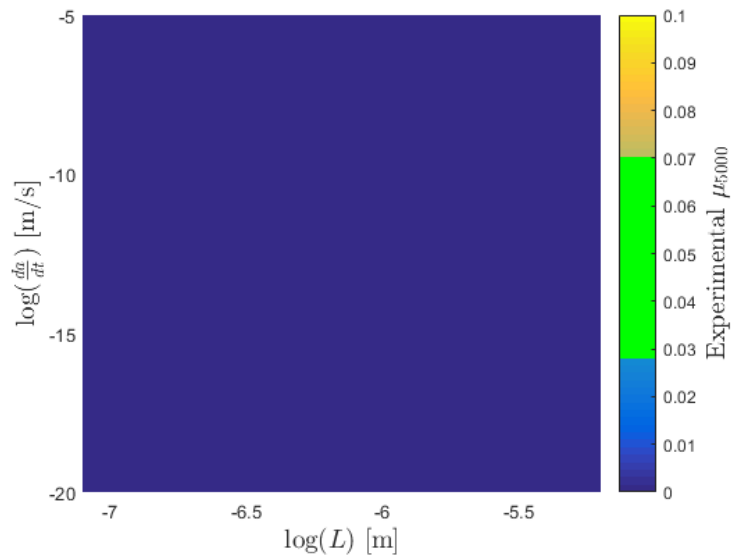


Figure 7.12 – Map of modeled values of μ given a L and $\frac{da}{dt}$ for R5A samples after 5000 cycles under 1 mN load. Green represents friction corresponding to experimental results. All combinations of parameters within the restrictions do not yield a valid value of μ .

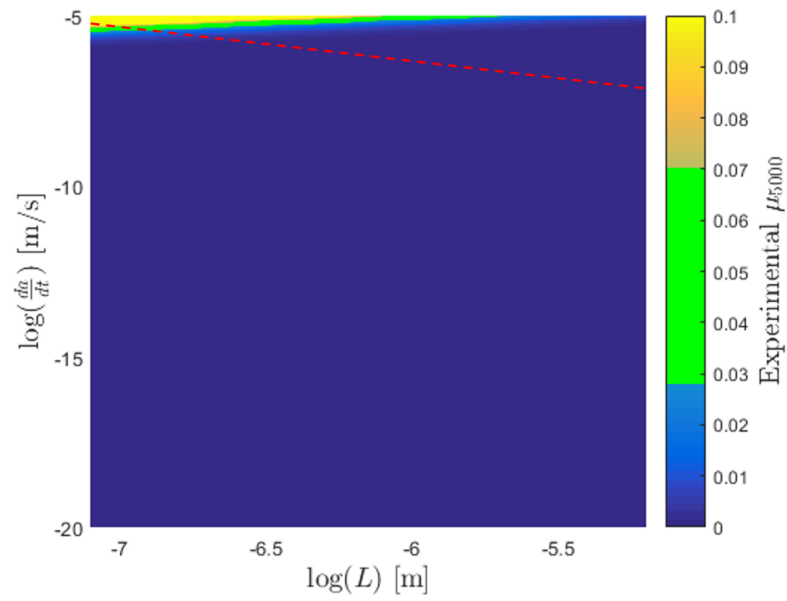


Figure 7.13 – Map of modeled values of μ given a L and $\frac{da}{dt}$ for R5A samples after 5000 cycles under 1 mN load. Dashed red line represents the threshold of valid values of a , determined by Figure 7.11. Green represents friction corresponding to experimental results.

Figure 7.14 shows the friction evolution with parameters at the extremes of the determined range of validity. The slope of the friction evolution curve over time is nearly identical, and is independent of L and $\frac{da}{dt}$. The slope is in fact governed by initial crack length a_0 , which has been fixed to zero until now.

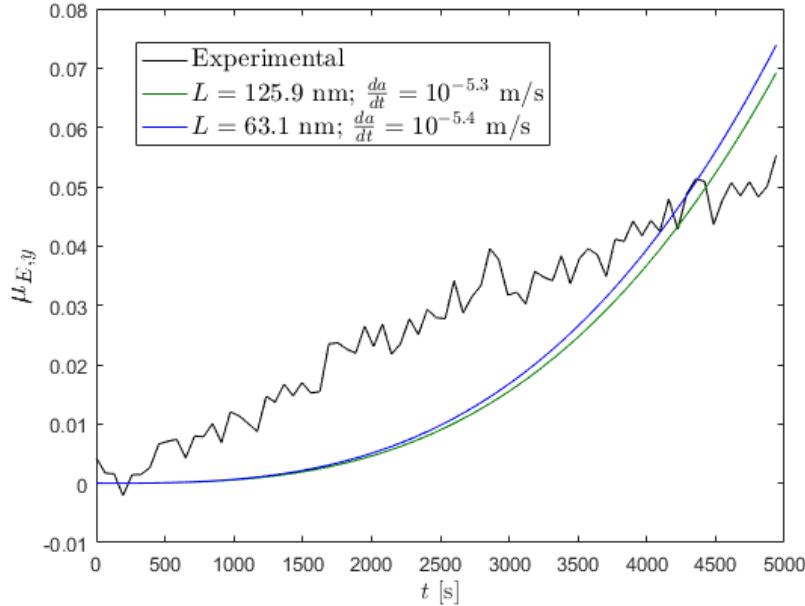


Figure 7.14 – Experimental μ_{Ey} compared to modeled μ_{Ey} for two sets of L and $\frac{da}{dt}$ within valid ranges determined from Figure 7.13

The process may be repeated for any arbitrary a_0 . The restriction is that a_0 must be less than the limit of $0.6 \mu\text{m}$. Figure 7.15 shows the effect of varying a_0 . An a_0 of approximately $0.15 \mu\text{m}$ closely approximates the experimental results, where L and $\frac{da}{dt}$ are determined to be 63.1 nm and $10^{-5.7} \text{ m/s}$ respectively. After 5000 cycles, crack length is modeled to be $0.307 \mu\text{m}$, which is within realistic ranges of a .

Acceptable values for all parameters of the friction model have been determined by fitting to a subset of experimental results, within realistic ranges that have been determined from literature. Unifying all of the components of friction with the determined parameters yields the total friction evolution shown in Figure 7.16. These parameters may be taken and used for applying the model to new experimental conditions.

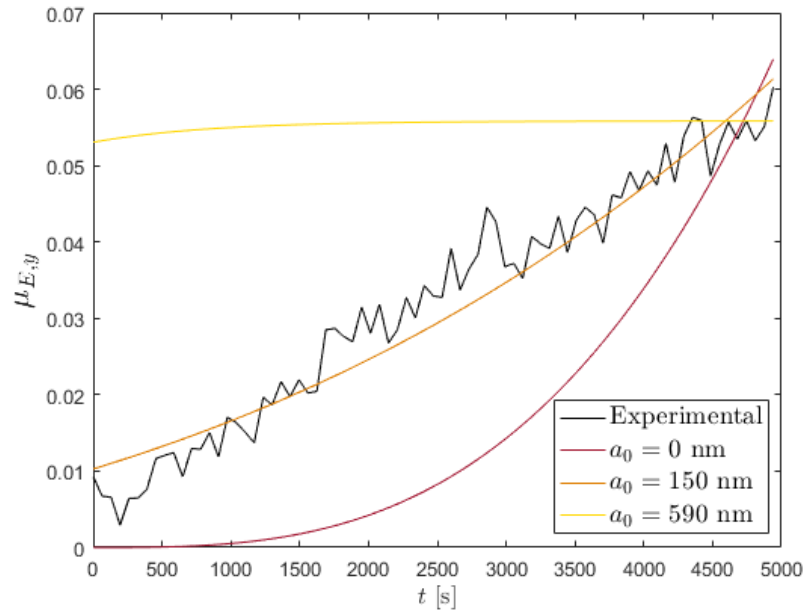


Figure 7.15 – Experimental $\mu_{E,y}$ compared to modeled $\mu_{E,y}$ with varying a_0

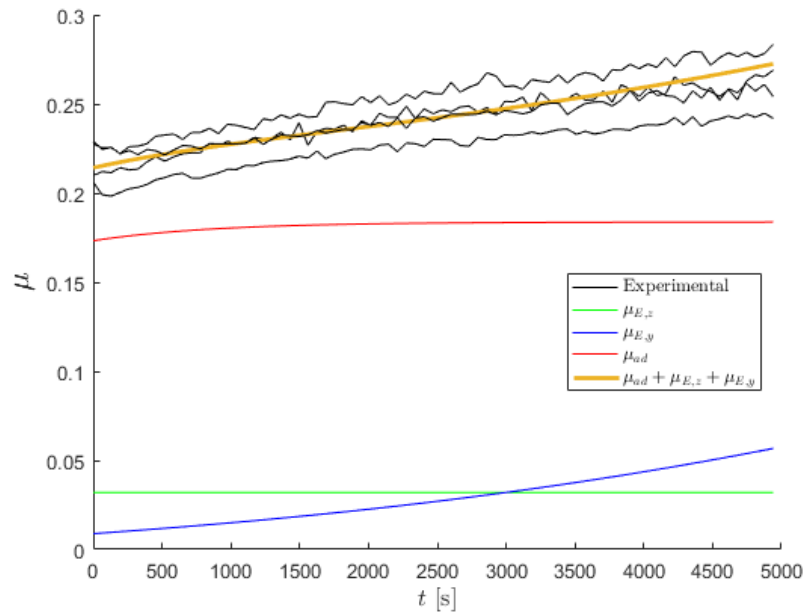


Figure 7.16 – Experimental vs modeled friction for R5A samples under 1 mN load over 5000 cycles using the cantilever deformation model, including all three components of friction. Multiple repetitions of the experimental results are shown.

7.3 Time Extrapolation

Friction may be extrapolated over time to assess model behavior compared to long term experiments. The data set shown thus far for model fitting has been from experiments of 5000 cycles. The modeled friction evolution may be extrapolated over time and compared with experimental results of longer durations. Figure 7.17 shows friction evolution from an experiment performed over 70000 cycles, and the modeled friction based on just a 5000 cycle experiment. Thus, the modeled friction diverges from the experimental results over time, greatly overestimating the rise in friction. Model parameters may also be extracted by fitting the model to the 70000 cycle results, which may allow identification of the critical parameters. It was determined that the newly fitted curve yields a crack velocity of $10^{-6.5}$ m/s, compared to the previous values of $10^{-5.7}$ m/s. From Figure 7.5, at $0.6 \text{ MPa}/\text{m}^{1/2}$ stress intensity, an order of magnitude difference in velocity corresponds to only a 5% difference in stress intensity. The model is thus highly sensitive to crack velocity. Further sensitivity analysis is required in order to better understand the predictive power of the model.

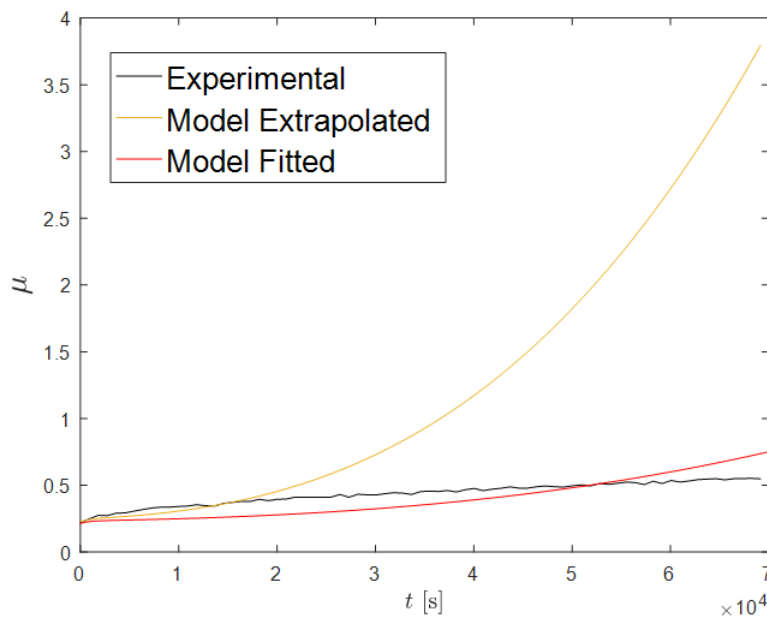


Figure 7.17 – Experimental friction evolution compared to modeled evolution using model of cantilever mode deformation of cracks with parameters extracted from 5000 cycle experiments (yellow) and parameters fitted to the 70000 cycle experiment (red).

There may be other factors that may account for an apparent overestimation of friction. The modeled friction evolution in the figure is given under the assumption that crack growth rate is constant. The divergence of the experimental results with the model may be explained if crack growth rate decreases over time. A number of mechanisms could contribute to slower crack growth rate over time that are not incorporated in the model. For example, firstly, there is currently no mechanism included that describes crack closure, which may limit crack growth

and allow stabilization of friction. Secondly, stress intensity is likely not constant with respect to crack length. Stress intensity may decrease with crack length if the stress field also decreases with depth. Thirdly, crack growth is not linear. The effective depth of the deformed segments is limited by the trajectory of the crack growth, as shown in Figure 2.6. Long term prediction of friction would require more detailed consideration of the crack growth mechanics.

7.4 Cylinder Misalignment

The alignment angle of the cylinder counterpiece with the flat surface may significantly change the characteristics of the contact, including A , c and E_{Ez} . The contact dimensions can be simulated using BES as shown in Figure 7.18 for misalignment angles of 0.01° , 0.1° and 1° . The extracted contact characteristics are shown in Table 7.1. Contact area increases significantly at low misalignment angles.

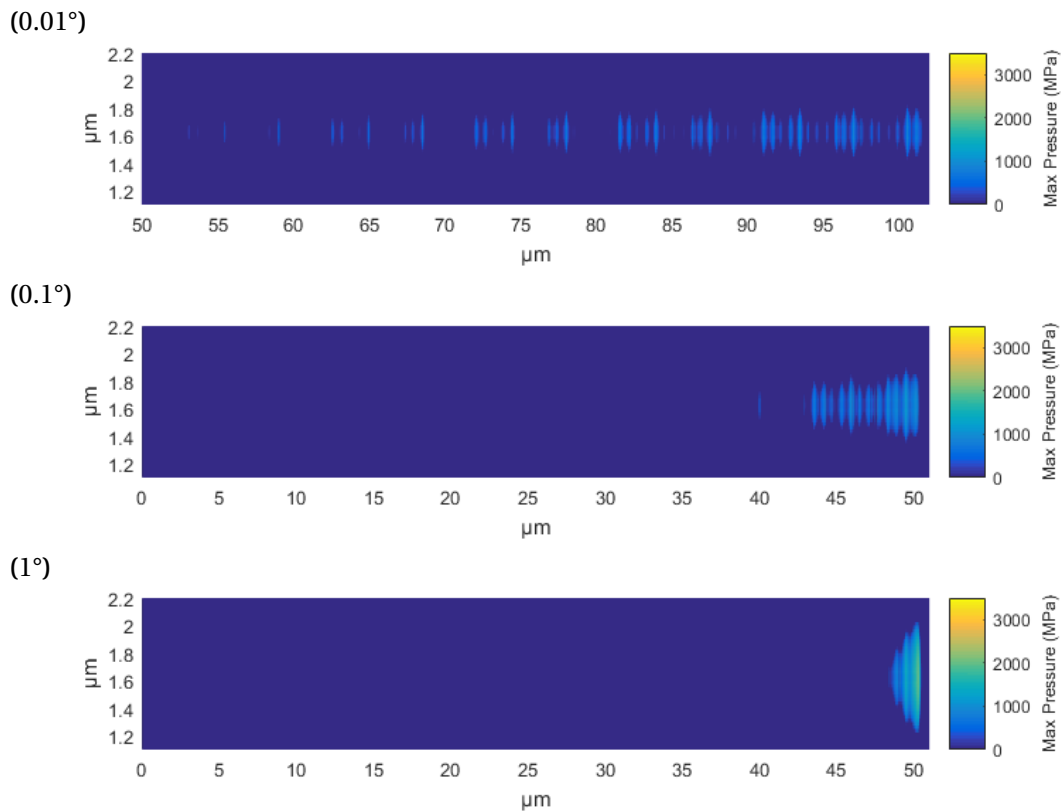


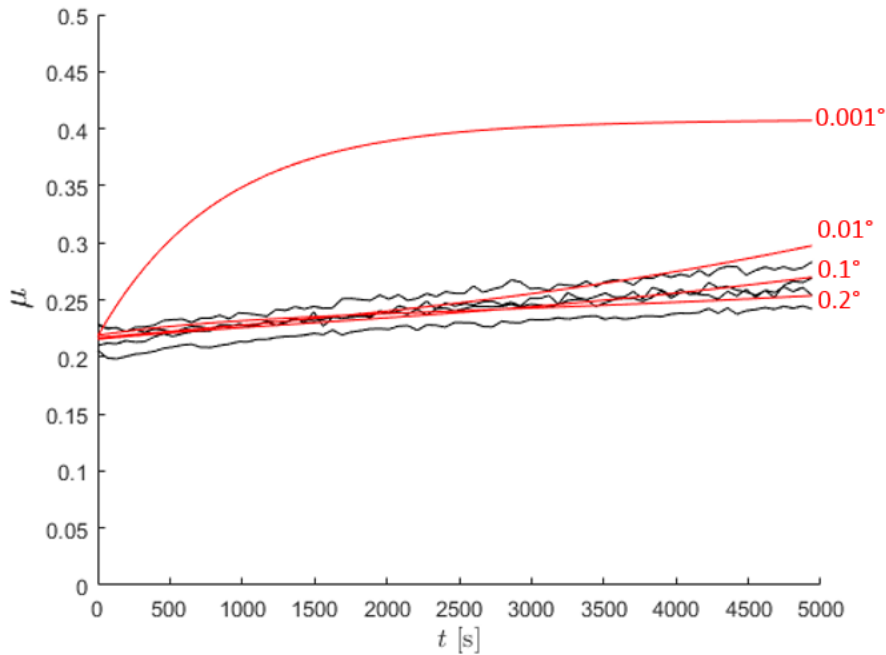
Figure 7.18 – BES of various angles of 0.01° , 0.1° and 1° tilt under 1 mN load with R5 sample

As shown in Figure 7.19, as expected the increased A leads to a significant increase friction coefficient at low misalignment angles. Variation of alignment angle of $\pm 0.09^\circ$ around 0.1° can result in dispersion of measured friction coefficient corresponding to the variation of friction experimentally observed between independent experiments. Lower misalignment angles is predicted to result in even greater friction coefficient, reaching over 0.4 after 5000

Table 7.1 – Values extracted from numerical contact simulations of various angles of 0.01°, 0.1° and 1° under 1 mN load with R5 samples

Angle (°)	P_{\max} [GPa]	A [μm^2]	b [μm]	δ [nm]
0.01	0.96	2.97	52.0	9.45
0.1	1.35	1.91	10.4	19.7
1	2.24	1.04	2.1	35.7

cycles. Although angle is measured to be 0.1° prior to contact, the alignment of the surfaces of the two bodies may change while under load introducing dispersion in results.

**Figure 7.19** – Modeled friction evolution at various misalignment (red) compared to four independent R5A experiments (black), at 1 mN load, 0.1° tilt and over 5000 cycles.

7.5 Varying Load

The model predicts significant dependence on normal load. The impact of changes in load can be determined using numerical simulations that allow extraction of contact dimensions and pressures under varying load conditions. The results of simulations at 0.1° tilt with R5A samples are shown in Figure 7.20. Extracted values are shown in Table 7.2. Increasing F_N causes significantly increased A , which leads to a proportional increase in μ_{ad} . Additionally, there is an increase in indentation energy $\mu_{E,z}$, and contact width b .

The modeled friction evolution at various loads are shown in Figure 7.21. A significant increase in contact area is expected at high loads. This increase in contact area is the primary

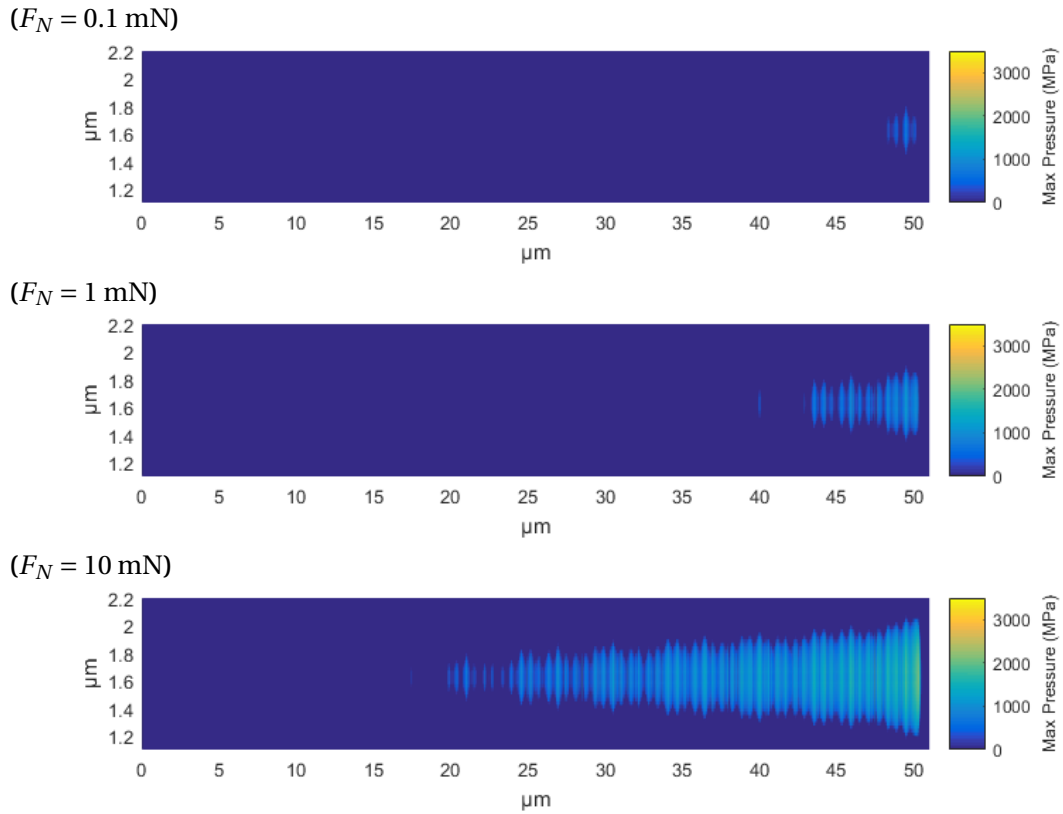


Figure 7.20 – BES of various loads of 0.1 mN, 1 mN and 10 mN load 1 mN load with R5 samples at 0.1° tilt. Sliding direction is up and down. The edge of the cylinder makes contact on the right side of the plot.

factor contributing to higher friction. The model overestimates the increase in friction for samples at 2 mN and 1.5 mN. More repetitions are required to verify. Experimental results of 4 mN were highly irreproducible showing two distinct behaviors between independent experiments. SEM imaging had shown differences in wear behavior. The wear behavior may alter the effective contact geometry and thus change contact area. Indeed, in the case of high friction at 4 mN a large contact area was observed and in the case of low friction a reduced contact area was observed.

Figure 7.22 shows the modeled friction at 4 mN with A altered to visualize the effects on friction. The contact area was increased by a factor of 10 to represent the flattening of the cylinder and reduced by a factor of 10 to represent the effect of wear debris accumulation on the cylinder counterpiece. All other parameters are kept constant. The rapid increase in friction with high A and the reduced μ with low A corresponds with experimental observations. The results can be fit *post hoc* to the model, however the irreproducibility of the behavior makes it difficult to predict *a priori*. Wear phenomena may be sensitive to stochastic processes depending on factors such as path of sliding and surface topography, which cause the irreproducibility. The results show that in the case of wear, the evolution of wear particles and their behavior during sliding must be known in detail.

Table 7.2 – Values extracted from numerical contact simulations of various loads of 0.1 mN, 1 mN and 10 mN with R5 samples at 0.1° tilt

Load (mN)	P_{\max} [GPa]	A [μm^2]	b [μm]	δ [nm]
0.1	0.95	0.28	1.9	6.65
1	1.35	1.91	10.4	19.7
10	2.34	12.9	33.0	61.3

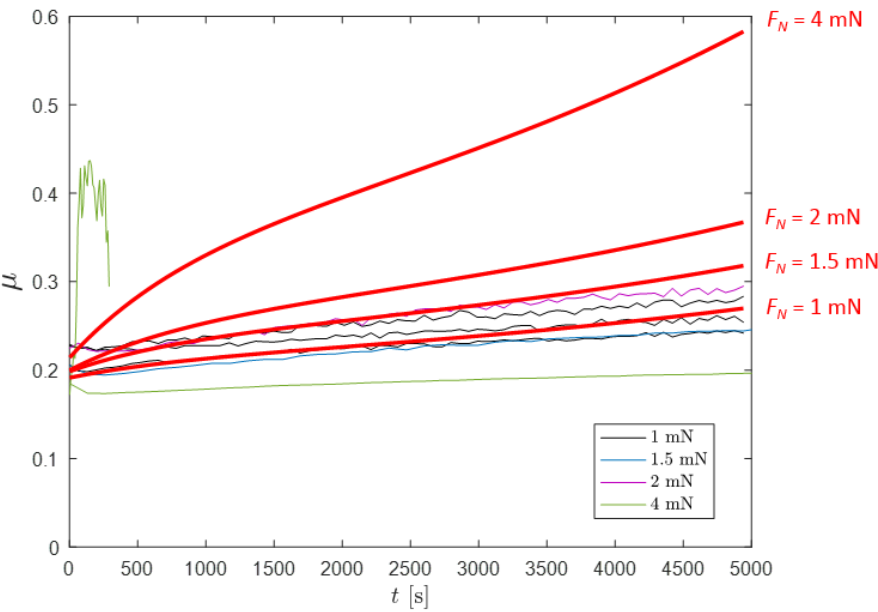


Figure 7.21 – Modeled friction evolution at various loads (red) compared to experiments at varying loads (as labeled), with 0.1° tilt over 5000 cycles. Two repetitions at 4 mN are shown.

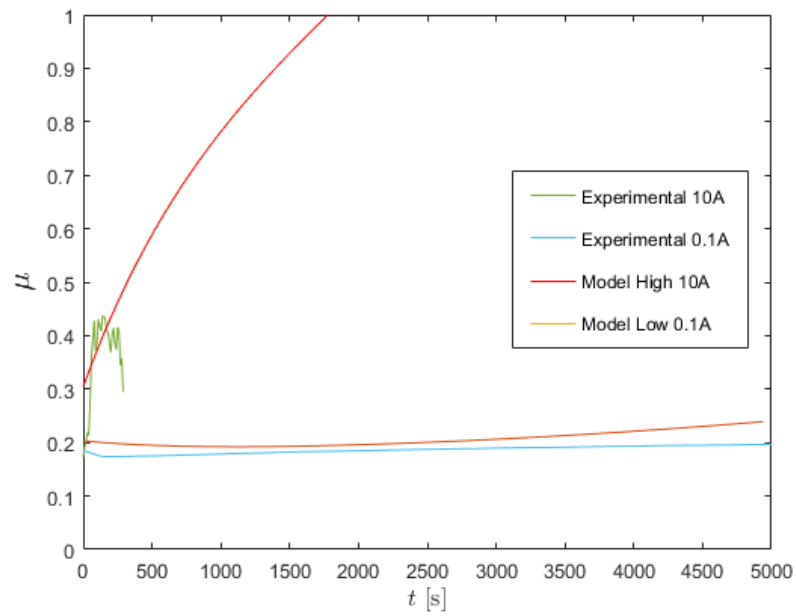
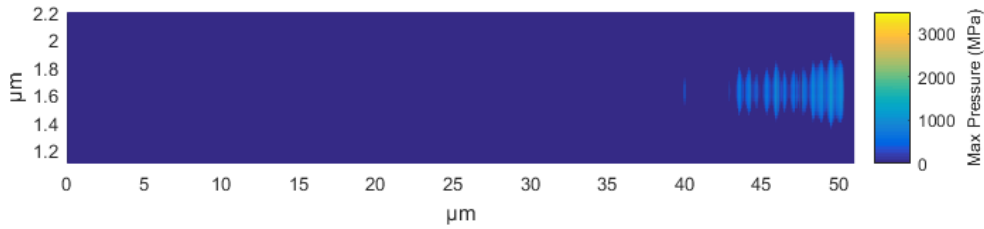


Figure 7.22 – Friction evolution of 4 mN where high contact area and low contact area are observed. Modeled friction evolution shows the effects of altering contact area by a factor of 4, keeping all else constant.

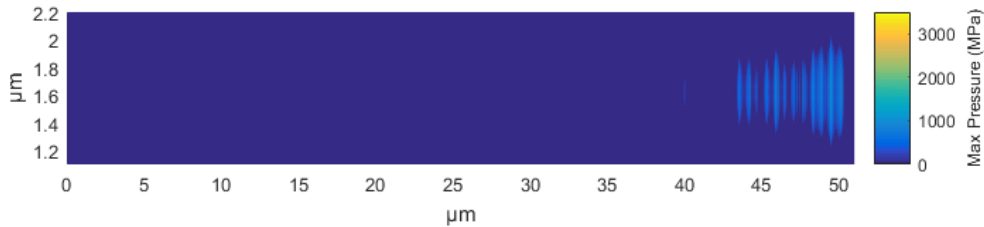
7.6 Varying Counterpiece Radius

Contact geometry is investigated by altering the primary radius of curvature of the cylinder counterpiece, r_1 . BES simulations are performed of radii of 5 μm , 10 μm and 20 μm as shown in Figure 7.23. The values extracted are shown in Table 7.3. Increasing the radius of curvature leads to greater A due to the increased size of the contact in the direction parallel to sliding.

($r_1 = 5 \mu\text{m}$)



($r_1 = 10 \mu\text{m}$)



($r_1 = 20 \mu\text{m}$)

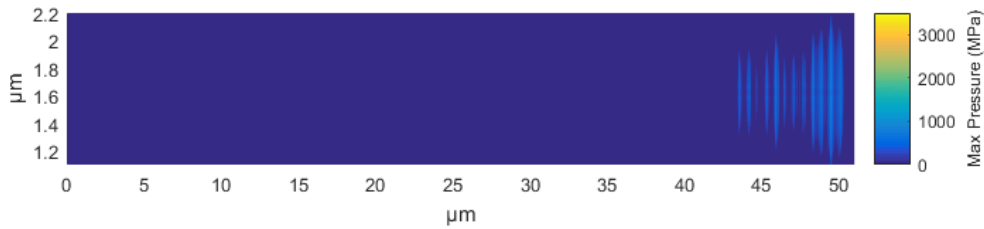


Figure 7.23 – BES of various radii of 5 μm , 10 μm and 20 μm under 1 mN load at 0.1° tilt. Sliding direction is up and down. The edge of the cylinder makes contact on the right side of the plot.

Table 7.3 – Values extracted from numerical contact simulations of various radii of 5 μm , 10 μm and 20 μm under 1 mN load at 0.1° tilt

Sample	P_{\max} [GPa]	A [μm^2]	b [μm]	δ [nm]
R5A	1.35	1.91	10.4	19.7
R10A	1.14	2.38	10.3	21.5
R20A	0.98	2.57	6.9	25.7

The results of the modeling are shown in Figure 7.24. The increase in μ as modeled matches closely with experimental results. The friction increase in the first few hundred cycles, governed by k_r , is underestimated. This could be explained if the rate of contaminant removal is dependent on tribosystem properties. k_r however, has thus far been taken as a constant. If

it was shear stress dependent, a higher k_r at higher μ may eliminate the underestimation that is observed.

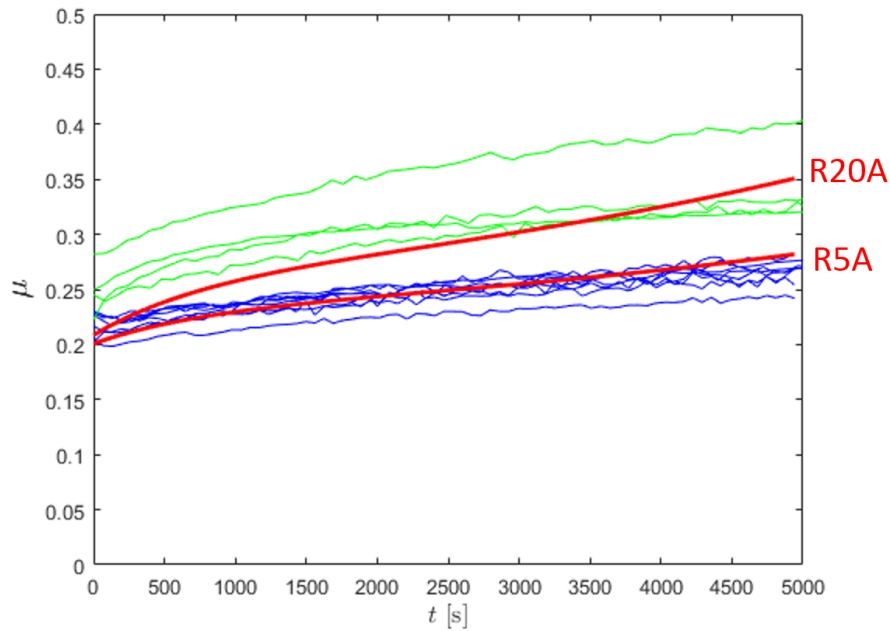


Figure 7.24 – Modeled friction evolution for various cylinder radii under 1 mN load with 0.1° tilt over 5000 cycles. L is proportional to b .

7.7 Chemical Treatments

The surface pretreatments performed, including water rinsing, IPA rinsing, benzene rinsing, and TCDS coating, introduced contaminating layers on the sample. It was observed by XPS that the friction obtained may be correlated to the atomic concentration of carbon. Different species adsorbed on the surface will result in different surface shear strengths. This implies that the friction of a contaminated surface μ_1 may vary between sample preparation methods. A reduced μ_1 decreases the initial friction. The rates of removal and adsorption, governed by k_r and $k_a p$, are also dependent on the adsorbed species. These rates govern how quickly the system reaches a steady-state friction that approaches the friction coefficient of a bare surface, μ_2 . The experiments show that for surface treatments with organic compounds, the friction is nearly constant with respect to time. This implies that the removal rate constant k_r is zero. Additionally, a significant decrease in the slope of the friction evolution was observed, indicating lower crack growth rates.

Figure 7.25 shows the model prediction compared to experimental values. Three different modeled friction evolutions are shown: (A) standard parameters determined for R5A samples, (B) half k_r and half $\frac{da}{dt}$ and (C) half μ_1 , zero k_r and zero $\frac{da}{dt}$. The evolution of friction can be well described by the model, however more detailed chemical analysis will be required in the future to evaluate the model parameters. The recoverable friction effect is in the inverse

direction for samples treated with organic solutions. The model does not incorporate any mechanism describing an inverse recoverable effect. To explain the recoverable decrease in friction there may be unconsidered mechanisms that change surface shear strength with the introduction of hydrocarbons. Tadmor et al. [61] suggested that the disentanglement of polymers may occur during sliding of polymer brushes bonded to the surface. Molecular scale rearrangement of adsorbed species may have similar effects in these pre-treated samples. Sufficient chemical analysis of the adsorbed species is lacking.

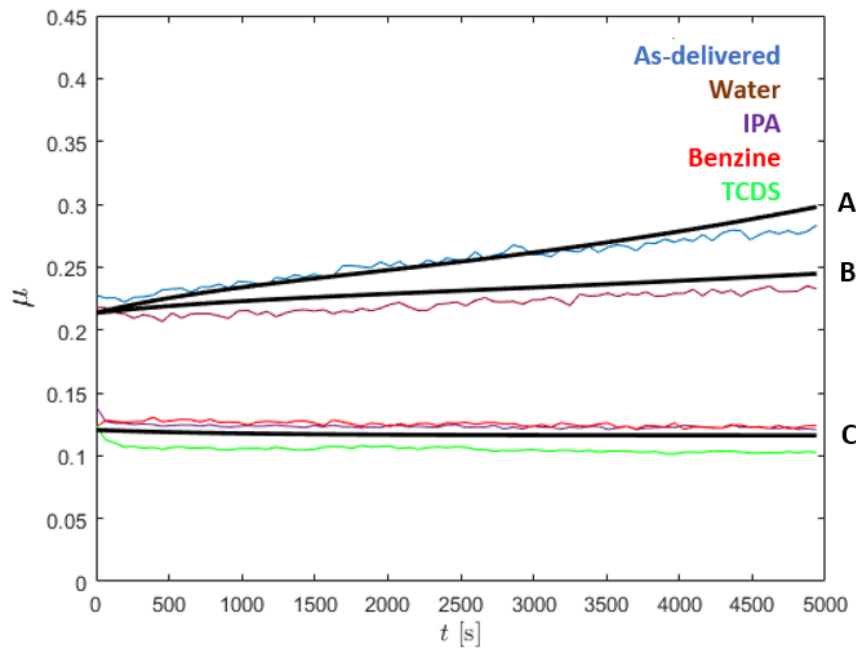


Figure 7.25 – Modeled friction evolution compared to experimental results for various surface treatments under 1 mN load with 0.1° tilt over 5000 cycles. The black lines represent modeled friction of (A) standard parameters determined for R5A samples, (B) half k_r and half $\frac{da}{dt}$ and (C) half μ_1 , zero k_r and zero $\frac{da}{dt}$.

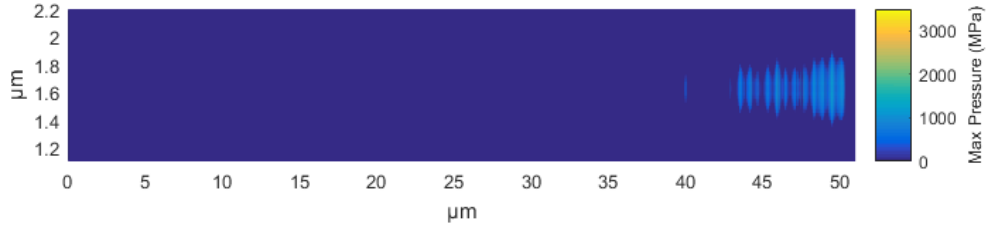
The results also show that crack growth may be greatly reduced. This is possibly explained firstly by the significant decrease in tangential stress. Secondly, there may be an effect of adsorbed carbon compounds on the inhibition of fracture of silicon dioxide by hydrolysis. Silicon dioxide fracture has been shown to be highly dependent on diffusion of water into the silicate network [17]. An adsorbed hydrophobic layer might act as a barrier against water diffusion. Further studies investigating the effects of humidity on these microscale systems may allow quantification of the role of water on friction.

7.8 Topography Effects

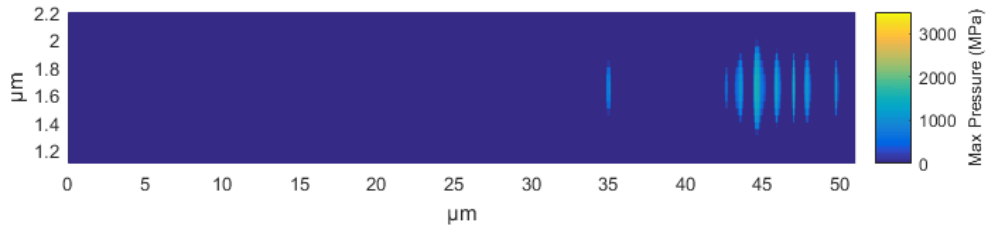
Varying topographies were studied with samples R5A, R5B, R5C and R5D. Maps of contact pressure are shown in Figure 7.26 for all of the topographies studied under a load of 1 mN. The

topographies with high roughness tend to have increased P_{\max} , decreased A , increased b and increased δ . Experiments at 0.1 mN were also performed. Parameters for 0.1 mN load can also be extracted using the same method, shown in Table 7.4. The extracted parameters can be used in the friction model to predict friction evolution behavior with each of the topographies.

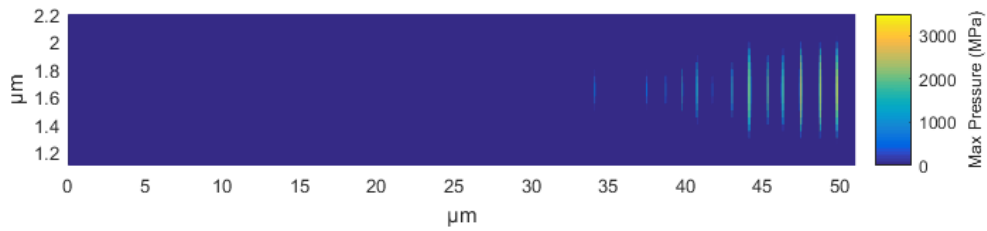
(R5A)



(R5B)



(R5C)



(R5D)

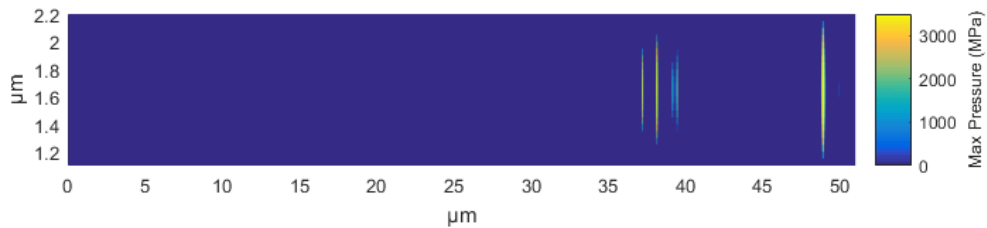


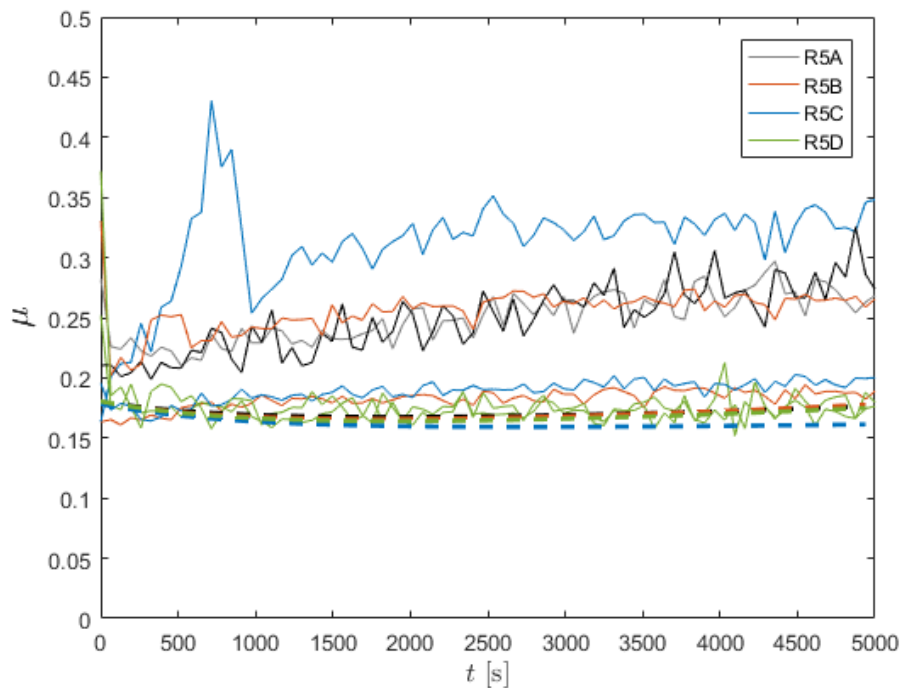
Figure 7.26 – BES of contact area for topographies A, B, C and D under 1 mN load at 0.1° tilt. Sliding direction is up and down. The edge of the cylinder makes contact on the right side of the plot.

Due to occurrence of wear in samples R5B and R5C at 1 mN, the worn contact geometry is transformed by a flattening of the cylinder counterpiece. Values extracted from BES do not accurately represent this geometry. Therefore, in order to apply BES extracted values, the model is applied to the experiments where wear is avoided at 0.1 mN load and 0.1° misalignment with R5A, R5B, R5C and R5D samples. Results of the modeled friction are shown in Figure 7.27. The modeled friction is shown as dashed lines corresponding in color to the experimental results. In general friction evolution is predicted to be constant with respect

Table 7.4 – Values extracted from numerical contact simulations of various topographies with 0.1° tilt and 0.1 mN normal load

Sample	P_{\max} [GPa]	A [μm^2]	b [μm]	δ [nm]
A	0.95	0.279	1.90	6.65
B	1.32	0.153	1.50	9.33
C	2.26	0.115	5.80	7.11
D	2.45	0.070	1.50	12.7

to time. This is behavior indeed observed experimentally for several samples, but there is high dispersion in the results. The low loads in this experiment yield a friction coefficient that is highly sensitive to changes in tangential force. The small contact dimensions also result in high variability of roughness in the path of sliding. Analysis of the topography effects on the model are limited by firstly the wear that occurs at high loads, and secondly the high variability of friction at low loads. Future sample topographies may be designed to allow 1 mN load experiments without wear.

**Figure 7.27** – Experimental results under 0.1 mN load compared to model predictions for R5A and R5B samples. Model parameters are from BES of elastic contact, and from parameters extracted from experiments at 1 mN. The modeled friction is shown as dashed lines corresponding in color to the experimental results.

7.9 Summary

By fitting the model with a subset of experimental data of R5A samples under 1 mN load over 5000 cycles, all the required model parameters have been determined. Parameters for crack length, crack velocity and crack spacing correspond to plausible values as determined from experiments and literature. The evolution of friction in the subset of data can be well described by the model.

Extrapolation of the model to other experimental conditions reveal limits of model applicability. The model overestimates friction growth over longer experiment durations, possibly due to simplifications of crack growth behavior. The model predicts dispersion in friction due to inaccuracy of angle misalignment, which may be a contributor to dispersion of results observed experimentally. The model overestimates the friction increase at higher loads of 1.5 mN and 2 mN, however further experimental repetitions are necessary to verify the dispersion in results. The increase in friction with increase in contact radius was well described by the model, although inaccuracies may be due to the assumption of constant k_r . The model can be used to explain *post hoc* the contact area dependence of friction in the 4 mN experiments where wear occurred. The model may be used *post hoc* to explain differences in surface chemistry and their effects on friction. Finally, analysis of model predictions for varying surface topography are limited by experimental results, where significant wear is observed at high loads and high variance is observed at low loads.

8 Conclusions

An experimental apparatus has been developed to allow for performing tribological experiments in conditions that simulate those experienced in watches. It allows experiments with microfabricated samples that are precisely aligned for reproducible contact geometry. The apparatus also allows tribological experiments of microscale loads and geometries. The experimental set-up is robust for testing durations of up to several days. It would meet the needs of any industrial application that utilize parts at these length and load scales.

The elastic deformation of the contact with misaligned cylinder-torus geometry has been modeled using BES. Real AFM profiles were incorporated to predict the effects of complex topographical changes. The BES allowed determination of the contact areas and pressures as a function of normal force, contact geometry and misalignment angle. The extracted values allow quantitative analysis of these factors on the experimental results.

Friction behavior of thermally grown silicon dioxide films were observed at low millinewton scale loads with no lubrication. Two characteristic time-dependent friction behaviors were observed. First was the permanent cumulative increase in friction throughout the experiment despite the lack of topographical change. Second is a recoverable phenomenon governed by two rate coefficients that describe friction recovery upon interruption and friction increase upon sliding. This characteristic friction behavior occurred in systems with no wear or surface plastic deformation. A run-in polishing wear was present in tribosystems under high contact pressure. The threshold contact pressure was able to be determined using BES. In the case of wear, the friction is highly irreproducible due to random behavior of wear particles. Nevertheless, a strong dependence on contact area was observed. Furthermore, experiments with chemical treatments showed strong dependence of both friction force and its time dependent behavior on surface carbon concentration. In general, the phenomena that influence friction was determined to be surface adsorption of contaminants, surface cracks and elastic deformation behavior.

A mechanistic model has been developed that allows for prediction of friction over time that is based on the evolution of the identified phenomena. In particular this includes surface contaminant adsorption, and elastic deformation behavior under conditions of subcritical crack growth. The model incorporates a recoverable friction effect that is the result of surface adsorption and desorption of contaminants, and a cumulative friction increase that is a result of the elastic deformation around growing cracks. Plausible model parameters were extracted based on a subset of experimental data.

Time extrapolation of the model overestimates the friction coefficient, likely due to high sensitivity of the model the crack velocity and simplifications of crack growth behavior. Further development is required to incorporate mechanisms that may act to reduce crack growth rate over time, in order to allow more accurate long term prediction of friction. Effects of misalignment, load, radius of contact, surface chemistry and topography were examined. The contribution of misalignment inaccuracy was quantified by the model. Increase in friction from contact radius is predicted by the model, although it overestimates the increase in friction from increased load. The model may be used *post hoc* to fit for and quantify the effects of contact area and surface chemistry. In any case, further sensitivity analysis is critical to precisely quantify the predictive power of the model.

In practice, in order to achieve low and constant friction, there are three approaches that can be recommended. First, contact pressures must be kept below the wear threshold in order to maintain predictable friction behavior. Second, contact area must be minimized in order to minimize adhesion interactions between contacting bodies. This study allows quantification of the trade-off between contact area and contact pressure in silicon dioxide systems given any surface topography. Additionally, surface chemical treatments may limit friction increase by decreasing surface shear strength and limiting crack growth. The model developed also allows quantification of the friction evolution given a change in surface chemistry, while also considering effects of contaminant adsorption.

References

- [1] E Rabinowicz, *Friction and wear of materials*, Wiley, New York, **1965**.
- [2] S. Mischler, S. Debaud, D. Landolt, *Journal of The Electrochemical Society* **1998**, *145*, 750–758.
- [3] M. Godet, *Wear* **1984**, *100*, 437–452.
- [4] A. L. Barnette, D. B. Asay, D. Kim, B. D. Guyer, H. Lim, M. J. Janik, S. H. Kim, *Langmuir* **2009**, *25*, 13052–13061.
- [5] U. Beerschwinger, R. Reuben, S. Yang, *Sensors and Actuators A: Physical* **1997**, *63*, 229–241.
- [6] K. Strawhecker, D. B. Asay, J. McKinney, S. H. Kim, *Tribology Letters* **2005**, *19*, 17–21.
- [7] D. B. Asay, M. T. Dugger, J. A. Ohlhausen, S. H. Kim, *Langmuir* **2008**, *24*, 155–159.
- [8] K. Noguchi, H. Fujita, M. Suzuki, N. Yoshimura in, *IEEE*, **1991**, pp. 148–153.
- [9] M. Lim, J. Chang, D. Schultz, R. Howe, R. White in, *IEEE*, **1990**, pp. 82–88.
- [10] K. Deng, W. H. Ko, *Journal of Micromechanics and Microengineering* **1992**, *2*, 14–20.
- [11] S. K. Parida, S. Dash, S. Patel, B. Mishra, *Advances in Colloid and Interface Science* **2006**, *121*, 77–110.
- [12] K. Kato, *Wear* **1990**, *136*, 117–133.
- [13] K.-H. Chung, Y.-H. Lee, D.-E. Kim, *Ultramicroscopy* **2005**, *102*, 161–171.
- [14] L. Chen, C. Xiao, X. He, B. Yu, S. H. Kim, L. Qian, *Tribology Letters* **2017**, *65*, DOI 10.1007/s11249-017-0922-9.
- [15] V. Hatty, H. Kahn, A. Heuer, *Journal of Microelectromechanical Systems* **2008**, *17*, 943–947.
- [16] L. Chen, X. He, H. Liu, L. Qian, S. H. Kim, *The Journal of Physical Chemistry C* **2018**, *122*, 11385–11391.
- [17] D. Hou, H. Ma, Z. Li, Z. Jin, *Acta Materialia* **2014**, *80*, 264–277.
- [18] G. S. White, S. W. Freiman, S. M. Wiederhorn, T. D. Coyle, *Journal of the American Ceramic Society* **1987**, *70*, 891–895.
- [19] C. Xiao, P. Shi, W. Yan, L. Chen, L. Qian, S. H. Kim, *Colloids and Interfaces* **2019**, *3*, 55.
- [20] D. B. Asay, S. H. Kim, *The Journal of Chemical Physics* **2006**, *124*, 174712.
- [21] L. Chen, C. Xiao, B. Yu, S. H. Kim, L. Qian, *Langmuir* **2017**, *33*, 9673–9679.
- [22] A Opitz, S.-U. Ahmed, J. Schaefer, M Scherge, *Wear* **2003**, *254*, 924–929.

- [23] D. B. Asay, S. H. Kim, *The Journal of Physical Chemistry B* **2005**, 109, 16760–16763.
- [24] J. Luo, J. Wang, E. Bitzek, J. Y. Huang, H. Zheng, L. Tong, Q. Yang, J. Li, S. X. Mao, *Nano Letters* **2016**, 16, 105–113.
- [25] B. R. Lawn, *Proceedings of the Royal Society A: Mathematical Physical and Engineering Sciences* **1967**, 299, 307–316.
- [26] Y. Wang, S. M. Hsu, *Wear* **1996**, 195, 112–122.
- [27] K. Kato, *Wear* **1992**, 153, 277–295.
- [28] H. Kitsunai, K. Hokkirigawa, *Wear* **1995**, 185, 9–15.
- [29] F. P. Bowden, D. Tabor, *British Journal of Applied Physics* **1966**, 17, 1521–1544.
- [30] E. Rabinowicz, *Journal of Applied Physics* **1961**, 32, 1440–1444.
- [31] B. Lincoln, *British Journal of Applied Physics* **1952**, 3, 260–263.
- [32] B. Lincoln, *Nature* **1953**, 172, 169–170.
- [33] A. S. Lodge, H. G. Howell, *Proceedings of the Physical Society. Section B* **1954**, 67, 89–97.
- [34] G. Stachowiak, A. Batchelor, *Engineering Tribology*, Elsevier, Amsterdam, **1993**.
- [35] F. Al-Bender, V. Lampaert, J. Swevers, *Tribology Letters* **2004**, 16, 81–93.
- [36] J. H. Dieterich in *Rock Friction and Earthquake Prediction*, (Eds.: J. D. Byerlee, M. Wyss), Birkhäuser Basel, Basel, **1978**, pp. 790–806.
- [37] J. R. Rice, A. L. Ruina, *Journal of Applied Mechanics* **1983**, 50, http://esag.harvard.edu/rice/105_RiceRuina_StabF 343–349.
- [38] G. Perrin, J. R. Rice, G. Zheng, *Journal of the Mechanics and Physics of Solids* **1995**, 43, 1461–1495.
- [39] L. Knopoff, R. Burridge, *Geophysical Journal International* **1966**, 11, 265–265.
- [40] J. M. Carlson, J. S. Langer, *Physical Review A* **1989**, 40, 6470–6484.
- [41] V. Popov, J. Gray, *ZAMM - Journal of Applied Mathematics and Mechanics / Zeitschrift für Angewandte Mathematik und Mechanik* **2012**, 92, 683–708.
- [42] G. Tomlinson, *The London Edinburgh and Dublin Philosophical Magazine and Journal of Science* **1929**, 7, 905–939.
- [43] T. Kontorova, J. Frenkel, *Zh. Eksp. Teor. Fiz.* **1938**, 8, 1340–1348.
- [44] E. Granato, M. R. Baldan, S. C. Ying in *Physics of Sliding Friction*, (Eds.: B. N. J. Persson, E. Tosatti), Springer Netherlands, Dordrecht, **1996**, pp. 103–118.
- [45] M. Weiss, F.-J. Elmer, *Physical Review B* **1996**, 53, 7539–7549.
- [46] M. Weiss, F.-J. Elmer, *Zeitschrift für Physik B Condensed Matter* **1997**, 104, 55–69.
- [47] D. Karnopp, *Journal of Dynamic Systems Measurement and Control* **1985**, 107, 100–103.
- [48] D. A. Haessig, B. Friedland, *Journal of Dynamic Systems Measurement and Control* **1991**, 113, 354–362.

- [49] B. Armstrong-Hélouvry, P. Dupont, C. C. De Wit, *Automatica* **1994**, 30, 1083–1138.
- [50] P. R. Dahl, A Solid Friction Model: tech. rep., Defense Technical Information Center, Fort Belvoir, VA, **1968**.
- [51] C. Canudas de Wit, H. Olsson, K. Astrom, P. Lischinsky, *IEEE Transactions on Automatic Control* **1995**, 40, 419–425.
- [52] P. Dupont, V. Hayward, B. Armstrong, F. Altpeter, *IEEE Transactions on Automatic Control* **2002**, 47, 787–792.
- [53] J. Swevers, F. Al-Bender, C. Ganseman, T. Projogo, *IEEE Transactions on Automatic Control* **2000**, 45, 675–686.
- [54] F. Al-Bender, V. Lampaert, J. Swevers, *IEEE Transactions on Automatic Control* **2005**, 50, 1883–1887.
- [55] I. Polonsky, L. Keer, *Wear* **1999**, 231, 206–219.
- [56] E. A. H. Vollebregt, *Journal of Optimization Theory and Applications* **2014**, 162, 931–953.
- [57] L. Batooli, **2019**, DOI 10.5075/EPFL-THESIS-7123.
- [58] M. Liu, Y. Gan, D. A. Hanaor, B. Liu, C. Chen, *Engineering Fracture Mechanics* **2015**, 149, 134–143.
- [59] G. M. Hamilton, L. E. Goodman, *Journal of Applied Mechanics* **1966**, 33, 371.
- [60] A. Bower, N. Fleck, *Journal of the Mechanics and Physics of Solids* **1994**, 42, 1375–1396.
- [61] R. Tadmor, J. Janik, J. Klein, L. J. Fetters, *Physical Review Letters* **2003**, 91, DOI 10.1103/PhysRevLett.91.115503.

Vance Nguyen

+1(647)847 0541 +41(77)955 67 65 vance.nguyen@gmail.com

Nationality: Canadian Residency: Switzerland

Education:

PhD, Materials Science & Eng.

École Polytechnique Fédérale de Lausanne, 2020

Thesis: Friction in Silicon Dioxide Micro-Contacts

Taught laboratory sessions in Corrosion for classes of 20-30 Bachelor students

Supervised semester-long projects for Master students

MSc, Materials Science & Eng.

École Polytechnique Fédérale de Lausanne, 2016

Thesis: Plastic deformation of oxide layers of metals in nanoindentation

Minor in Area and Cultural Studies: Systemic Segregation of African Diaspora Communities in China

Study Abroad in Shanghai and Bangalore (4 weeks)

BASc, Nanotechnology Engineering

University of Waterloo, 2014

Graduation Project: Aluminum Oxide Nanofluid for CPU Cooling

Employment:

R&D Intern @ ABB Switzerland Ltd. Semiconductors

Lenzburg, Switzerland 9/2015–2/2016

- Identified failure factors in diamond-like-carbon passivation layers in power electronics.

Junior Engineer @ Toronto Microelectronics

Mississauga, Canada 5/2014–6/2014

- Designed stop-sign cameras for deploying to school buses allowing entry into \$10m North America market

R&D Intern @ Toagosei Inc.

Nagoya, Japan 1/2013–8/2013

- Miniaturized industry chemical processes to develop a novel acrylate adhesive for entry into PSA market

R&D Intern @ B & W Hospital, Harvard Medical School

Boston, USA 9/2011–4/2012

- Designed enzyme-based nanoparticle drugs in \$15m research project for combatting atherosclerosis

R&D Intern @ Center for Advanced Materials Joining

Waterloo, Canada 1/2011–4/2011

- Design of extreme heat/pressure system for comparative study of copper and gold wire bonds

Publications:

Chobaut, N., Drezet, J. M., Mischler, S., Nguyen, V., De Marco, B., Dobler, S., & Rosset, E. (2019).

Miniaturized tube fixed plug drawing[...]. Journal of Materials Processing Technology, 263, 396-407.

Kamaly, N. et al. (2016). *Targeted interleukin-10 nanotherapeutics [...]*. ACS nano, 10(5), 5280-5292.

Presentations:

Poster Presentation. EDMX Research Day 2019

Poster Presentation. EDMX Research Day 2018

Poster Presentation. Tribology Gordon Research Conference 2018

Seminar Presentation. Workshop on Mechanical Testing at the Micro/Nano-scale 2016

Languages:

English (native), Vietnamese, Japanese (JLPT N2 certified 2019), French, Mandarin Chinese (beginner)

Other:

Operations Volunteer for Lausanne Underground Film Festival

2017-2018

Recipient of Huayu Enrichment Scholarship for Mandarin study in Taiwan

2014

Events Co-ordinator of UW Vietnamese Students' Association

2012-2014